

# Influence of sour environment on crack initiation at corrosion pits under cyclic loading

Farhad, Farnoosh

*Award date:*
2019

*Awarding institution:*
Coventry University

# Influence of sour environment on crack initiation at corrosion pits under cyclic loading

**By**

**Farnoosh FARHAD**

**December 2018**


***A thesis submitted in partial fulfilment of the University's requirements for the Degree of Doctor of Philosophy***

# Certificate of Ethical Approval

Applicant:

Farnoosh Farhad

Project Title:

Predicting remaining life from corrosion pitting to fatigue cracking in X65 steel pipelines

This is to certify that the above named applicant has completed the Coventry University Ethical Approval process and their project has been confirmed and approved as Low Risk

Date of approval:

07 September 2018

Project Reference Number:

P75831

## Table of Contents

## List of Tables

## List of Figures

## Acknowledgments

I would like to express my sincerest gratitude to my industrial supervisor Dr David Smyth-Boyle for his endless support, kindness and friendship throughout this research. I am deeply grateful to my first academic supervisor Prof Xiang Zhang for her constructive comments, criticism and advices on this work and her kind support during these three years. This dissertation is the product of these two people's encouragement and guidance.

I wish to thank Dr Kashif Khan, my second academic supervisor for his advices.

This work was enabled through, and undertaken at the National Structural Integrity Research Centre (NSIRC Ltd.), a postgraduate engineering facility in Cambridge for industry-led research into structural integrity established and managed by TWI Ltd. through a network of both national and international universities. I would not have been able to come to Cambridge and this thesis would not have been possible, without financial support of TWI Ltd, Coventry University and BP. I would like to express my deepest gratitude to them who have made it possible for me to achieve my dream and accomplish my academic goals at this level of study.

I am grateful to my colleague and dear friend Muntasir Hashim who trained me to use X-ray tomography device and micro-electrochemical cell. I also thank him for discussions about our research as well as all life matters. I am thankful to TWI project leaders, Dr. Jenny Crump for discussions on my research and to Dorothee Panggabean for her advice and support on X-ray tomography. My acknowledgments also go to the TWI laboratory technicians, Mr Mark Tinkler and Mr. Jack Smith for their great assistance and Mr Ian Wallis for his advice on designing the environmental vessel.

I could not have done any of this without the love and support from my parents, my brother and my sister who always supported and believed in me. Especially, my parents who taught me to be hard work, confident and believe in myself at every stage of my life. I would like to thank my parents-in-law and sister-in-law for their continued love and kindness. I also want to express my gratefulness to my daughter, Termeh, who will be born in March 2019. She has accompanied me during my thesis write up stage and it was the love I have had for her that enabled me to be happy at every moment of this stage and finish my thesis on time. Last but certainly the biggest thank you of all goes to my incredible husband, Sadegh. He has been the best friend, partner and advisor for me. I could not have done any of this without his love and support.

**Farnoosh Farhad**

**Cambridge, Dec 2018**

***It is to my loves, my husband, Sadegh, and my daughter to be born, Termeh, that I dedicate this dissertation.***

## Abstract

Corrosion pits are a form of geometrical discontinuity that lead to stress and strain concentration in engineering components, resulting in crack initiation under service loading conditions and ultimately fracture and failure, in which case the damage process is more commonly known as corrosion fatigue. Initiation and propagation of cracks in offshore pipelines can lead to loss of containment and environmental and commercial impacts. In order to prevent such failures, tools to predict the structural integrity of pipelines need to be improved. The transition from corrosion pit to corrosion fatigue crack, the so-called pit-to-crack transition, is a significant portion of the total fatigue life and yet the underlying mechanism is still not well understood. This constitutes an important knowledge gap, which has to be addressed in order to advance the life prediction methods for the assets. A sensible approach to progressing the understanding of the pit-to-crack transition, thus providing further clarity regarding the overall process of corrosion fatigue, is to conduct testing and condition monitoring under representative conditions of the field environment and service loading conditions. Most approaches that attempt to model corrosion fatigue focus on the crack propagation stage rather than crack initiation. Available models used to predict the fatigue crack initiation from corrosion pits are based on the transition criterion, which is defined using long crack growth rate data and linear elastic fracture mechanics (LEFM). These prediction models assume pits as small cracks and use LEFM criteria to predict long crack. This approach neglects the short crack initiation life, which should not be neglected especially in the high cycle fatigue regime. Limitations in applying this criterion to short crack initiation from pits mean that determining a criterion for short crack initiation from a pit remains a major challenge. In this project, it is hypothesised that corrosion pits do not behave as

cracks but they may be the primary location for crack initiation. It is also hypothesised that the geometry of the pits and the level of stress value play important role in the crack initiation time.

Oil and gas production pipelines often operate under sour corrosive environments in combination with cyclic loading. It is well known that an aggressive environment can reduce the fatigue life of materials. Consequently, it is important to replicate in-service conditions during testing to obtain reliable data regarding corrosion fatigue behaviour and in particular pit-to-crack transitions in API-5L X65 grade steel pipelines that are commonly used for oil and gas products risers due to their good weldability, mechanical properties and low cost. The material of interest in this study is seamless API-5L X65 grade pipeline steel that was provided by the industrial sponsor. This work investigates the effect of sour corrosive environment on fatigue behaviour of corrosion pits in X65 grade steel risers utilising experimental, numerical and analytical methods.

This PhD project was set up to investigate the influence of sour corrosive environments on the pit-to-crack transition in X65 pipeline steel. The main aspects of the investigation include: (a) whether the sour environment could change the nature of the crack initiation process (e.g. fatigue damage development time and crack location) relative to fatigue damage process in the air environment; (b) whether it was possible to develop a predictive model for the pit-to-crack evolution based only on the pit geometry and size, and the material mechanical properties in the sour environment.

An electrochemical method was used to create corrosion pits on the specimens and good control over the desired size of corrosion pits was achieved. An environmental cell was designed and constructed to undertake in-situ corrosion fatigue tests in a sour corrosive

environment containing toxic gas of H2S under uniaxial fatigue loading. The bespoke test cell allows periodic non-destructive X-ray micro-computed tomography of the specimen in-situ during fatigue testing and thus enables monitoring of material degradation as it progresses and in particular the pit-to-crack transition. This approach provides more direct information on crack initiation than complementary ex-situ techniques such as Scanning Electron Microscopy (SEM) of post-test metallographic specimens. Load-controlled fatigue tests were carried out on smooth and pre-pitted specimens in both air and sour corrosive environment. Results presented herein demonstrate the performance and reliability of this approach. In addition, fractography of the specimens was carried out to more investigate the location of crack initiation from the pits. S-N curve was established in both air and sour corrosive environments to be used in a predictive model. Local stress-strain behaviour at corrosion pits and its effect on fatigue crack initiation were investigated using elastic-plastic finite element analysis of specimens containing a single corrosion pit under static and cyclic loading. Analytical methods were also used to predict the local maximum stress and strain at the pit, which showed similar results to the finite element analysis result. Finally, a model was proposed to predict the pit-to-crack transition life that showed good agreements with experimental results. The local stress and strain ranges at corrosion pits were calculated by simultaneously solving the material's cyclic stress-strain relationship with either the Neuber's or Glinka's rule. Thereafter, the obtained local stress amplitude and mean stress were used to predict fatigue crack initiation life ($N_i$) using Smith-Watson-Topper (SWT) equation for ambient condition and the measured material's S-N data test for the sour environment.

## Nomenclature

| | |
|---|---|
| $a$ | Pit depth |
| $a/2c$ | Pit aspect ratio |
| $a'$ | Material constant |
| $b$ | Fatigue Strength Exponent |
| $C$ | Fatigue Ductility Exponent |
| c | Half of pit width |
| $E$ | Elastic modulus |
| $E1$ | Percentage Elongation |
| $K$ , $K'$ | Monotonic and Cyclic Strength Coefficient |
| $K_f$ , $K_t$ | Fatigue notch and stress concentration factor |
| $N_f$ | Number of cycles to failure |
| $N_i$ | Number of cycles to crack initiation |
| $n$ , $n'$ | Monotonic and Cyclic strain Hardening Exponent |
| r | Pit radius |
| t | Plate thickness |
| $YS_L$ , $YS_U$ , $YS'$ | Lower, Upper and Cyclic Yield Strength |
| $\Delta S$ , $\Delta\sigma$ | Applied and Local stress range |
| $\Delta\varepsilon$ | Local strain range |
| $\varepsilon_a$ | Strain amplitude |
| $\varepsilon'_f$ , $\sigma'_f$ | Fatigue Ductility and Fatigue Strength Coefficient |
| $\sigma_a$ | Stress amplitude |
| $\sigma_e$ | Fatigue limit |
| $\sigma_f$ , $\sigma_{UTS}$ | True Fracture and Ultimate Tensile Strength |
| $\sigma_m$ , $\sigma_{\max}$ | Mean and Maximum stress |

## Published Contents

Farhad, F., Zhang, X., Smyth-Boyle, D. **(2018)** Fatigue behaviour of corrosion pits in X65 steel pipelines. *Proceedings of the Institution of Mechanical Engineers, Part C: Journal of Mechanical Engineering Science.* https://doi.org/10.1177/0954406218776338

Farhad, F., Smyth-Boyle, D., Zhang, X. **(2018)** Laboratory apparatus for in-situ corrosion fatigue testing and characterisation of fatigue cracks using X-ray micro-computed tomography. *Fatigue & Fracture of Engineering Materials & Structures.* https://doi.org/10.1111/ffe.12873

Farhad, F., Smyth-Boyle, D., Zhang, X., Govender, K. **(2018)** Corrosion fatigue behaviour of X65 steel oil and gas pipelines. *12th International Fatigue Congress*, Poitier, France.

Farhad, F., Zhang, X., Smyth-Boyle, D., Khan, M.K. **(2017)** Evaluation of Simulated Corrosion Pits in X65 Steel. *NACE CORROSION 2017*, New Orleans, USA.

Farhad, F., Hashim, M., Smyth-Boyle, D., Zhang, X., Khan, M.K. **(2017)** Characterisation of corrosion pitting and induced fatigue cracking using X-ray micro-tomography. *International Conference on Tomography of Materials and Structures*, Lund, Sweden.

# Chapter 1: Introduction

## 1.1 Motivation

Networks of subsea pipelines that often extend for thousands of kilometres are used to transport production fluids to surface facilities for the oil and gas industry. Due to the operational conditions and the nature of the production fluids, pipes are typically subjected to cyclic loading and their internal surfaces are often exposed to the sour corrosive environment (i.e. containing $H_2S$). Cyclic loads acting on the pipelines are as a result of the sea wave motions, seabed movements and fluctuations in the internal pressure and temperature (Gamboa et al. 2008, Zhang, YM et al. 2016). In steel catenary risers, which form the basis for this study, the specific sources of cyclic loading are the direct and indirect effect of waves (including motions of floating production facility) and installation fatigue load (Bai, Y. and Bai, Q. 2005). It is reported that 18% of the failures in the oil and gas industry were caused by fatigue (Kermani et al. 1996). As fatigue has been cited as the underlying cause for many catastrophic failures experienced within the oil and gas industry, it is important to accurately predict the fatigue life of these assets in order to better manage the integrity of the pipelines. The driving factors in fatigue for the offshore structures include the presence of defects, stress concentration at joints, applied mechanical stress from the environmental loads and corrosion (Wirsching 1984). Corrosion can induce a form of localized damage termed pitting. Localized corrosion is found as a primary factor in most of the failures reported by the oil and gas industry (Zhang, GA and Cheng, Y. 2011, Mohammed et al. 2017). More specifically, corrosion pits are often the sites for initiation of fatigue cracks, in which case the damage process is more commonly known as corrosion fatigue. The transition from corrosion pit to corrosion fatigue

crack, the so-called pit-to-crack transition, is a significant portion of the total fatigue life and yet the underlying mechanism is still not well understood. This constitutes an important knowledge gap, which has to be addressed in order to advance the life prediction methods for the assets. A sensible approach to progressing the understanding of the pit-to-crack transition, thus providing further clarity regarding the overall process of corrosion fatigue, is to conduct testing and condition monitoring under representative conditions of the field environment and service loading conditions.

Pipelines used to transport oil and gases are commonly assembled from the API-5L grade X65 steel. Despite their useful mechanical properties and general availability, X65 and related grades of pipeline steels are prone to localized forms of corrosion such as pitting in the oil and gas production environments (Zhang, GA and Cheng, Y. 2011). The consequences of fatigue crack nucleation and growth from the aforementioned corrosion pits can be extremely serious, as the failure of subsea components of offshore assets can have serious safety, environmental and financial implications. To increase safety and reduce consequential costs resulting from failure, prediction of asset life or remaining life of components is of particular interest. A more reliable fatigue life prediction model would result in an improvement in maintenance and inspection scheduling, in addition to the potential for further cost reductions due to fewer failures and increased operational safety.

## 1.2 Aims and Objectives

This PhD project was set up to investigate the influence of sour corrosive environments on the pit-to-crack transition in X65 pipeline steel. The main aspects of

the investigation include: (a) whether the sour environment could change the nature of the crack initiation process (e.g. fatigue damage development time and crack location) relative to fatigue damage process in the air environment; (b) whether it was possible to develop a predictive model for the pit-to-crack evolution based only on the pit geometry and size, and the material mechanical properties in the sour environment. In order to achieve this goal, the following objectives were defined:

1. To obtain the material's Stress-Life (S-N) curve in both the ambient air and sour corrosive environments, by testing smooth specimens.
2. To produce a corrosion pit of desired dimension on smooth specimen using an electrochemical method.
3. To design and manufacture an environmental test vessel to facilitate corrosion fatigue tests in environment containing toxic $H_2S$. Furthermore, the vessel design shall allow X-ray tomography inspection of the specimen *in-situ* and hence monitoring crack initiation from the corrosion pit.
4. To perform representative small-scale corrosion fatigue tests, to collect test data on pre-pitted specimens in the ambient air and sour corrosive environments.
5. To perform metallographic examination after testing, to establish the crack initiation location and make other relevant observations.
6. To undertake Finite Element Analysis (FEA) under cyclic load by using the material cyclic load properties and an elastic-plastic material model, to acquire the pit local stress and strains in order to perform life prediction based on the local stress-strain approach.

7. To use semi-analytical models from literature to estimate the local stress and strain values at the pit base; to compare with the FEA stress result from the Objective 6 (as the semi-analytical models offer time efficiency).
8. To propose a method for predicting corrosion pit-to-fatigue crack transition life, using the knowledge and findings generated from the previous objectives.

## 1.3 Thesis structure

This thesis is composed of six chapters. Chapter 1 provides an overview of the subject and demonstrates the need for and relevance of the present work. Aims and objectives of the study are also presented. Chapter 2 contains a literature review with a specific focus on the works carried out by other researchers on the corrosion pit-to-crack transition. The methodology used is detailed in Chapters 3 and 4. Chapter 3 includes all the experimental methodology, while Chapter 4 provides an account of the methods for life prediction, covering the semi-analytical and Finite Element Method approaches used in this work. The results are presented in Chapter 5. Chapter 6 includes a summary of novel contributions to the field, main conclusions and recommendations for future studies.

# Chapter 2: Literature Review

The first and second Sections of this Chapter provide a brief overview of the topic of corrosion and corrosion pitting, in the context of and relating to the oil and gas industry and environmental assisted cracking. Sections 2.3 to 2.6 present a summary of findings from previous research, with particular focus on investigations concerning the pit-to-crack transition process. Section 2.7 describes how the application of X-ray computed tomography for characterisation of materials has furthered the understanding of pit-to-crack phenomena. Finally, this Chapter concludes with a summary of the state-of-the-art highlighting the gaps in the literature.

## 2.1 Corrosion and corrosion pitting in oil and gas pipelines

Corrosion is the term given to the chemical or electrochemical process leading to loss of material as a result of a material/environment interaction. Engineering components often operate in environments (e.g. marine) that are corrosive to their materials of construction (Akid, R 1996). Corrosion plays a critical role in threatening the structural integrity of oil and gas pipelines. It is noted that 33% of failures in the oil and gas industry can be attributed to corrosion (Kermani et al. 1996). In addition to safety and environmental concerns, corrosion presents a significant financial impact and is reported to consume of the order 2.2 trillion US dollars from the oil and gas industry across the world economy (Ossai et al. 2015). One of the most recent incidents that resulted in fatalities occurred as a result of corrosion in gas pipelines, whereby an explosion occurred at a pipeline in Taiwan in 2014, which killed 25 people and injured several hundred people (Ossai et al. 2015).

Electrochemical corrosion can be conveniently classified as either (1) general or uniform corrosion (*i.e.* uniform loss of material averaged across the surface, where the anodic and cathodic regions are constantly changing) or (2) localised corrosion (loss of material is localised at specific anodic regions on the surface). The latter form of corrosion includes pitting, crevice corrosion, galvanic corrosion and intergranular corrosion (Papavinasam 2013). Table 2.1 lists the documented causes of corrosion-related failures in the oil and gas sector and their corresponding percentage of the total number of failures. Data were collected from a survey during 1980s (Kermani et al. 1996). Figure 2.1 illustrates some of the types of corrosion, both internal and external that can occur with pipelines.

Table 2.1. Cause of corrosion related failure in the oil and gas industry during 1980s (Kermani et al. 1996).

| Type of failure | Total failure | Type of failure | Total failure |
|---|---|---|---|
| CO2 related | 28 | Galvanic | 6 |
| H2S related | 18 | Crevice | 3 |
| Preferential weld | 18 | Impingement | 3 |
| Pitting | 12 | Stress corrosion | 3 |
| Erosion corrosion | 9 | | |

Figure 2.1. Possible types of corrosion in pipelines (Karami 2012). MIC stands for microbiologically induced corrosion.

Electrochemical corrosion (‘wet’ corrosion) requires the presence of four prerequisites: an anode, a cathode, a conduction path for the electrons (usually the metal) and an ionic conductor (the electrolyte). In simple terms, at the metal anode, oxidation takes place and the metal loses electrons. Electrons migrate towards the cathode and depending on the electrolyte pH, reduction of hydrogen ions or dissolved molecular oxygen occurs at the cathode, i.e. the electrons produced at the anode are consumed at the cathode (Papavinasam 2013). Corrosion will cease to occur in the absence of any of four prerequisites. Figure 2.2 is a schematic showing a possible anodic and cathodic reaction in the pipe walls.

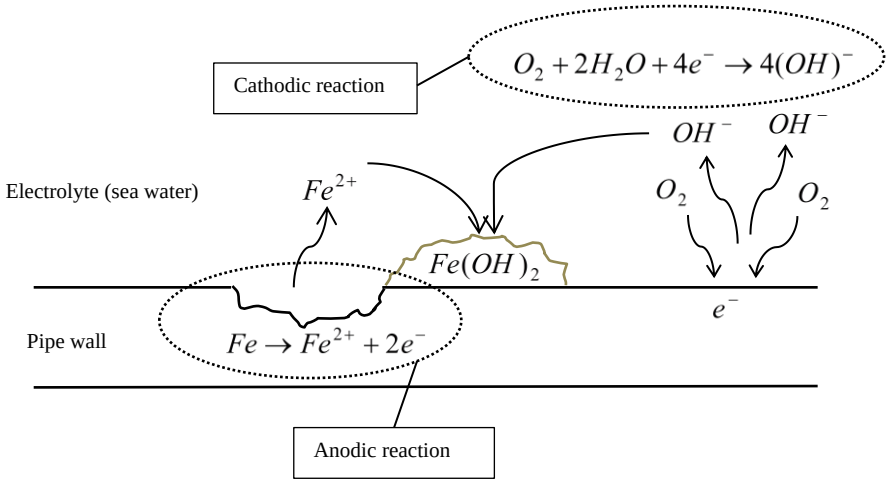


Figure 2.2. Schematic of cathodic and anodic reactions that take place during corrosion of steel in aerated seawater.

The anodic and cathodic reactions in pipe walls are as follows (Ohaeri et al. 2018):

Anodic reaction: $Fe \rightarrow Fe^{2+} + 2e^-$ (Iron dissolution)

Cathodic reactions: $2H^+ + 2e^- \rightarrow H_2$ (Hydrogen reduction)

$O_2 + 2H_2O + 4e^- \rightarrow 4OH^-$ (Oxygen reduction in neutral and alkaline media)

$O_2 + 4H^+ + 4e^- \rightarrow 2H_2O$ (Oxygen reduction in acidic media)

Typicallyy, the oil and gas hydrocarbon products transported in the risers contain carbon dioxide ($CO_2$ ) and hydrogen sulphide ($H_2S$) as impurities, which when dissolved in water will result in low pH values (Bai, Y. and Bai, Q. 2005) and lead to risk of so-called sweet and sour corrosion. The electrochemical reactions involved are as follows (Ossai et al. 2015):

Sour corrosion: $Fe + H_2S + H_2O \rightarrow FeS + 2H^+ + H_2O$

Sweet corrosion: $CO_2 + H_2O \rightarrow H_2CO_3$

$H_2CO_3 \rightarrow 2H^+ + CO_3^{2-}$

$Fe^{2+} + CO_3^{2-} \rightarrow FeCO_3$

In addition to general corrosion and localised pitting, the nature of sour environments present an increased risk of cracking due to the development of more significant levels of diffusible hydrogen in the metal, which can lead to embrittlement of both stressed (residual and applied, static and cyclic) and unstressed steel alloys. It is generally understood that the risk of fatigue cracking and failure may be greater in sour environments, due to corrosion pitting and the embrittling effect of atomic hydrogen (Ossai et al. 2015).

Pitting corrosion is an insidious form of localised damage that may lead to through-wall failure and loss of containment in pipelines. Failure may occur directly through corrosion or indirectly following a pit-to-crack transitional stage. Corrosion pits may develop where there is localised damage to the protective layer of material, which may comprise a passive film or native oxide layer or applied coating. Pits may evolve via voids in a coating layer or where the surface region contains microstructural defects. Due to the highly localised nature of pitting corrosion, through wall penetration may occur relatively quickly without any significant damage to other areas, leading to loss of containment in a pipe or vessel. Cracks can also initiate from pits since they act as stress risers. As a result, pitting is a threat to the structural integrity of many assets and is often cited as the most significant form of localised corrosion (Kolios et al. 2014, Caines et al. 2013). A unified understanding of the pit-to-crack evolution is still not available which leads to an unrealistic assessment of assets remaining life.

In the literature, the general mechanism for pitting is discussed in terms of three sequential stages; nucleation, propagation and passivation. Due to the stochastic nature of pitting, variety in pitting location and geometry (Figure 2.3) is expected for a material subject to pitting corrosion (Caines et al. 2013). Depending on the material and environment, the pits can have deep, shallow, undercutting, subsurface, horizontal grain attack and vertical grain attack shapes (Caines et al. 2013).

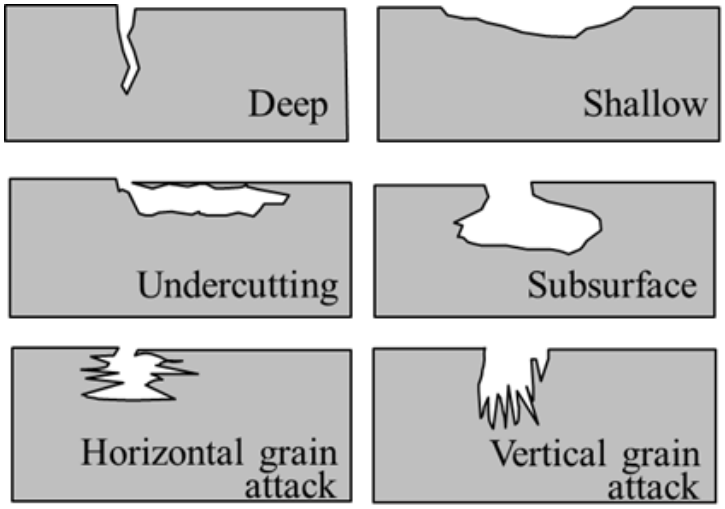


Figure 2.3. Typical cross-sectional shapes of corrosion pits (Caines et al. 2013).

Electrochemical Polarisation curves can be used to identify the resistance of a material to pitting corrosion. For metals and their alloys that exhibit active-passive behaviour, these curves can indicate the potential where pitting initiates ($E_{pit}$) in the forward anodic direction, and the minimum potential required in the reverse cathodic direction to re-passivates the surface ($E_R$). Pitting is predicted to continue when the potential remains between $E_{pit}$ and $E_R$ (Figure 2.4) (Caines et al. 2013, Bhandari et al. 2015).

Figure 2.4. Schematic of anodic Polarisation curve for a metal immersed in an aggressive solution (Caines et al. 2013).

Caines et al. (2013) defines the conditions for pitting as follows. The protective layer is damaged, the lectrolyte is aggressive and continue to be aggressive and the initial electrochemical potential to form the pit is above the $E_{pit}$ value and the pit continues to grow as long as the potential stays above $E_R$.

## 2.2 Environmental assisted cracking (EAC)

The interaction between material, environment and loading that lead to initiation and propagation of certain cracks in the components is referred to environmentally assisted cracking (EAC) (Turnbull, A 1993). EAC can be categorized as stress corrosion cracking (SCC), hydrogen-assisted cracking (HSC) and corrosion fatigue (CF) (Lynch 2016).

### 2.2.1 Stress Corrosion Cracking (SCC)

SCC is the failure of material under static stress, which is generally tensile (Papavinasam 2013), in corrosive environment (Parkins 1964). The likelihood of SCC

depends on the nature of the material and the environment. For example, SCC can occur in stainless steel exposed to  acidic chloride containing environments but not in ammonia, whereas for brass the opposite is true (Papavinasam 2013). SCC cracks tend to show branching which differentiates them from fatigue cracks and propagate in branches (Papavinasam 2013). As stated in Table 2.1, 3% of total failures in oil and gas pipelines can be attributed to SCC. The material composition, microstructure and surface conditionin addition to environmental conditions (temperature, chemistry) and stress type and level all influence the susceptibility to SCC (Papavinasam 2013).

SCC can initiate from the surface discontinuities such as corrosion pits. A study by Turnbull, Alan and Crocker (2006) showed that stress corrosion cracks from pits initiated at the location of plastic strain localisation, which was at or just below the surface, near to corrosion pits and in the form of one of the profiles in Figure 2.5. In the same study, around 50% of stress corrosion cracks had the profile shape (b) and broke the surface, *i.e.* in these cases, pits were deeper than cracks (Turnbull, A et al. 2006, Turnbull, Alan 2014).

Figure 2.5. Illustration of pits and cracks seen in the experimental study of stress corrosion cracking (Turnbull, Alan and Crocker, Louise 2006).

### 2.2.2 Hydrogen-Assisted Cracking (HAC)

Another form of EAC is termed hydrogen-assisted cracking. Corrosion of metals in electrochemical reducing acidic environments including hydrogen sulphide ($H_2S$), hydrogen fluoride (HF) or hydrogen cyanide (HCN) can generate hydrogen atoms through cathodic reduction of protons ($H^+ + e^- \rightarrow H$) (Papavinasam 2013). These hydrogen atoms can combine to form hydrogen gas, which can form bubbles and leave the surface. The small atomic radii of hydrogen also allows a fraction of the atoms also to diffuse into the metal, retarding dislocation movement (thus ductility) and generating tensile forces that weakening the inter-atomic bonds, all of which can lead to cracking (Lynch 2016). The factors cited in literature that influence hydrogen assisted cracking include strain (Scully and Moran 1988), microstructural and

mechanical properties (Li, Xinfeng et al. 2018, Ohaeri et al. 2018), the environment (in particular the presence of hydrogen recombination poisons such as $H_2S$) and temperature (Ohaeri et al. 2018).

### 2.2.3 Corrosion Fatigue (CF)

Corrosion fatigue (CF) cracking is a type of environmentally assisted cracking that derives from the combined action of cyclic stress and presence of a corrosive environment. The phenomenon of corrosion assisted fatigue was first described by Haigh in 1917 and corrosion fatigue testing was firstly reported by McAdam in late 1920s (Jones and Hoeppner, D. W. 2009). The processes that govern CF are complex and the electrochemical mechanisms that prevail depend on the specific material-environmental combination. CF induced failure can occur through a combination of stages, beginning from the point where the protective layer of material (coating layer or passive film or oxide layer) is damaged or where pre-existing defects exist on the surface (McEvily Jr 1990). Under corrosion fatigue conditions, the surface protective layer can be damaged leading to exposure of the underlying alloy to the corrosive environment and thus localised corrosion. The formation of localised corrosion pits causes an increase in the local stress and as a result fatigue cracks can initiate at these locations. The presence of a corrosive environment can also increase the growth rate of cracks (but not always) and consequently decrease the fatigue life (Akid, R 2010). The stress-life ( $S-N$ ) curve in Figure 2.6 and crack growth rate ( $da/dN-\Delta K$ ) curve in Figure 2.7 reveal how different materials can behave under cyclic load in the presence of a corrosive environment. Figure 2.6 illustrates the idea that by introducing a corrosive environment, the fatigue limit (*i.e.* the stress level below which the crack

arrests) may be eliminated (Akid, R 1996). Figure 2.7 shows how the fatigue crack growth rate may be expected to increase in a corrosive medium.

Figure 2.6. Relative S-N fatigue behaviour under various environmental conditions (Stephens, R. I. et al. 2000).



Figure 2.7. Fatigue crack growth rate in the air and corrosion environments (Akid, R 2010).

The fatigue crack growth (FCG) in pipelines has been studied extensively through experimental tests in different media, such as seawater (Poberezhnyi et al. 2016), $H_2$

gas environments (Amaro et al. 2014), and near-neutral environments consist of $CO_2$ and $H_2S$ (Eadie, RL et al. 2005, Vosikovsky 1976). The corrosion fatigue data collected showed that crack growth rate increased in this environment and the higher the concentration of $H_2S$, the higher the crack growth rate. Yu et al. (2015) studied the effect of loading frequencies on the crack growth rate of X60 pipeline samples in a near-neutral pH environment. The corrosion fatigue tests were carried out using a solution saturated with 5% $CO_2$ (nitrogen balance) using a frequency range from $10^{-5}$ to $5x10^{-1}$ Hz. In addition to the observation of two distinct regimes of crack growth rate, it was found that the crack growth rate increased with decreasing loading frequency until $10^{-3}$ Hz, beyond which no significant changes were noted.

Due to experimental limitations, less strain-life ( $\varepsilon - N$ ) data has been collected in comparison to stress-life (S-N) data and curves for corrosion fatigue conditions. One reason for this is that in strain-controlled tests, an extensometer or strain gauge is used to measure the strain. As the component needs to be isolated from the aqueous corrosive environment, these types of tests are experimentally difficult (Stephens, R. I. et al. 2000).

Variables affecting corrosion fatigue are reported as for example the microstructure of the material, loading frequency, environment, applied stress and surface condition (Akid, R 2010). Studies have been carried out to investigate the factors affecting corrosion fatigue life. Van der Walde and Hillberry (2008) concluded from experimental CF tests that the number of flaws and their interaction plays an important role in corrosion fatigue life, while the exact nature of flaws was of lesser importance. As chemical reaction rates tend to increase with temperature, it is not surprising that several workers have reported that the corrosion rate of materials is

different at different temperatures (Yang, Y. and Akid, Robert 2015, Zhang, YL et al. 2015). Hydrogen assisted cracking of carbon steels tends to be more severe at lower temperatures because the tendency of hydrogen to escape from the material at higher temperature.

Zhang, X.-Y. et al. (2013) has conducted fatigue tests in air and artificial seawater on pre-pitted and smooth specimens to produce data for S-N curves. Comparing the S-N curves for real corrosion pits and artificially-induced pits indicated a decrease in fatigue lifetime for real pits. This result highlights the importance of real corrosion pits to provide more realistic models for prediction of corrosion fatigue life. Results also indicated that the higher stress amplitude leads to greater numbers of corrosion pits.

Although many studies have attempted to model the failure mechanisms involved in CF and consequently provide predictions on asset integrity, there is still no general model that can provide accurate predictions. One reason for this deficiency is that corrosion fatigue life prediction models are typically based on long crack growth rate and no deterministic model, in general, considers short crack phenomena, which have different characteristics and behaviour (Akid, R 1996). Provision of a realistic damage prediction method would be desirable, as it would help optimise maintenance and inspection schedules and presumably reduce failures.

Within the oil and gas sector, API 5L-X65 steel is commonly used for the conveyance of production fluids. Despite the useful material properties and low cost, this alloy grade is known to be susceptible to pitting and cracking in several different media (e.g. alkaline bicarbonate oxidizing conditions or acidic reducing ‘sour’ solutions).

Fatoba and Akid, Robert (2014) investigated the operative damage mechanisms during crack initiation, propagation and failure of X65 steel under low cyclic loading. Tensile tests were carried out using dog-bone shaped specimens. The inelastic strain of fully reversed push-pull with strain amplitude ranging between 0.3% and 1.2% were investigated. The microstructural images of the specimens were taken using Scanning Electron Microscopy (SEM) in order to gain information to determine the damage mechanism. From the high magnitude of the measured plastic strain, it can be concluded that early crack nucleation and propagation is a result of an increase in the total strain. At higher levels of strain amplitude, multiple cracks were observed. This study has the merit of measuring the plastic strain in early stages of fatigue life, but not in the context of a corrosive environment (*i.e.* CF data).

Considering the importance of aggressive environment on fatigue life of materials, it is important to replicate oil and gas pipelines in-service conditions, *i.e.* sour environment including $H_2S$, during testing to obtain reliable data regarding corrosion fatigue behaviour and in particular pit-to-crack transitions in X65 steel pipelines. Wang and Akid (Wang, Y and Akid, R 1996), Akid and Dmytrakh (Akid, R and Dmytrakh, I 1998), Arriscorreta (Arriscorreta 2012), Baragetti (Baragetti 2014), Li and Akid (Li, S.-X. and Akid, R 2013) have used chambers to expose the specimen to saline solutions (NaCl) during fatigue tests. The corrosion mini-cell used by Akid and Dmytrakh (Akid, R and Dmytrakh, I 1998) exposed the specimen to $0.3cm^3$ of artificial seawater and is open to the atmosphere. Their tests were carried out under uniaxial fatigue loading. Li and Akid (Li, S.-X. and Akid, R 2013) utilised a rubber chamber for undertaking 4-point rotating bending corrosion fatigue tests. The low volume environmental chamber designed by Arriscorreta (Arriscorreta 2012) enabled

continues flow of test solution to ensure that the test environment was replenished during corrosion fatigue tests. Baragetti (Baragetti 2014) exposed the specimen notch area to NaCl solution by bolting two pieces of Plexiglass shells around the specimen. The described environmental chambers were useful for corrosion fatigue tests in NaCl solutions; however, these chambers are not practical for testing in an environment consisting of toxic $H_2S$ because the required chamber needs to be sealed securely. Due to the challenges in experimental testing (including the Health and Safety considerations (Sun, J. et al. 2016), as $H_2S$ is toxic), the effect of sour environments on the mechanism of fatigue crack initiation has not been addressed thus far by researchers. Therefore, a primary aim of this project was to carry out uniaxial fatigue tests in a sour corrosive environment.

## 2.3 Corrosion pit-to-fatigue crack transition

Oil and gas production pipelines often operate under sour corrosive environments that include $H_2S$ gas in combination with cyclic loading. As previously stated, it is well known that an aggressive environment can reduce the fatigue life of materials (Srivatsan and Sudarshan 1988). In the presence of an aggressive environment, corrosion pits can initiate and then grow to a finite size before terminating (*i.e.* 'dead' pits). Cyclic loading is thought to decrease the pitting potential during the tensile phase and therefore the ease whereby pitting may proceed (Guan et al. 2015). Under continuing cyclic load, pits may then lead to a pit-to-crack transition and short crack growth, followed by another transition to the long crack regime. Ultimately, the process leads to final failure. Overall the pitting corrosion fatigue life includes six phases; pit nucleation, pit growth, transition from pit to the short crack, short crack growth, transition from short to long crack and long crack growth (Kolios et al. 2014,

Li, S.-X. and Akid, R 2013, Caines et al. 2013, Zhang, R. and Mahadevan 2001, Jakubowski 2015). This process is shown in Figure 2.8. Akid, Robert et al. (2006) states that the pit-to-crack transition is "an extremely important life controlling stage" where the damage mechanism changes from a time-dependent corrosion dominated process to a cycle dependent mechanical loading dominated process (Akid, R 2010) (Figure 2.9). The deteriorating effect of localised corrosion interacting with cyclic loading was first established following the Aloha airline accident in April 1988 that was ascribed to pitting corrosion induced fatigue cracking (Goswami, Tarun and Hoeppner, D. W. 1999).




Figure 2.8. Pitting corrosion fatigue regimes (Akid, R 2010).

Figure 2.9. Pitting corrosion fatigue regimes showing corrosion dominated and mechanical loading dominated stages (Akid, Robert et al. 2006).

Although carbon steels can be prone to localised forms of corrosion such as pitting in oil and gas production environments, they are commonly used for pipelines (Zhang, GA and Cheng, Y. 2011). Much of the current literature on pit-to-crack transition pays particular attention to alloys used in aircraft industry such as Al-alloys (Chlistovsky et al. 2007, Ishihara et al. 2006, Van der Walde and Hillberry 2007, Dolley et al. 2000, Pidaparti, R. M. and Patel, R. R. 2008, Medved et al. 2004). The existing literature on steel is focuses particularly on medium carbon (Goto and Nisitani 1992, Kawai and Kasai 1985, Miller and Akid, R 1996, Wang, Y and Akid, R 1996) and high carbon steel (Cornet and GOLAN 1959, Linder and Blom 2001). The carbon steel material grades that are commonly used for oil and gas products risers are API 5L X60, X65 and X70 due to their good weldability, mechanical properties and low cost (Bai, Y. and Bai, Q. 2005). There is a relatively small body of literature that is concerned with low carbon steel used in offshore structures (Lu, B. and Luo 2006, Ahn et al. 1992, Boukerrou and Cottis 1993).

The consequences of fatigue crack development from corrosion pits can be serious in the oil and gas sector, as the failure of offshore components can have serious safety, environmental and financial implications. Localised corrosion is cited as a primary factor in many cases of the failures reported by the oil and gas industry (Zhang, GA and Cheng, Y. 2011, Mohammed et al. 2017). As shown in Table 2.1, 12 % of total failures in this industry have been ascribed to corrosion pitting. To prevent this, a more reliable fatigue life prediction model would result in an improvement in maintenance and inspection scheduling, in addition to the potential for further cost reductions due to fewer failures and increased operational safety.

Fatigue cracks have been studied widely in the literature showing they often emanate and propagate from corrosion pits (Kolios et al. 2014). Therefore, corrosion pits are of particular interest in fatigue life considerations. However, pitting initiation and propagation are complex stochastic processes with variations that are system-specific to each metal-environment. The pit-to-crack transition is of particular interest and arguably the least well-understood process. Consideration of the above leads to the conclusion that a useful step in the design and maintenance of marine environment components is to correctly identify the processes that reduce the fatigue life of assets due to the presence of pitting corrosion.

It has been stated that all cracks which result in final failure emanate from pits (Schoenbauer et al. 2015) but not necessarily from the deepest pit (Xu and Wang, You-de 2015). However, investigation of CF initiation and pit growth by Ebara (2007) in 12% chromium stainless steel in two different plane bending stress ranges indicated that the crack initiated from the base of deepest corrosion pit. Interrupted fatigue testing was performed using three different stress levels by Van der Walde &

Hillberry (2007) (Van der Walde and Hillberry 2008) on 32 dog-bones 2024-T3 aluminium specimens pre-corroded by 6 to 24hrs exposure. The tests were interrupted at defined stages, corresponding to the different percentage of final fatigue life, and the cracks were characterised. The initial crack size was determined in all specimens to be of the order twice the average grain size in the corresponding metallurgical direction. Around 40% of early-stage cracks were found to emanate from the base of pits and 60% from the pits sides. Several studies have noted that the crack initiates not necessarily from the bottom of a pit but may also emerge from the pit side wall (Van der Walde and Hillberry 2007, Horner et al. 2011, Turnbull, Alan 2014, Schoenbauer et al. 2015). In the work described in Van der Walde and Hillberry (2007) and Lu and Luo (2006), non-pit crack and pit-crack initiation were observed meaning that not every crack were initiated at the corrosion pits.

Data from several studies suggest that the critical pit depth can be different even in the same materials. For example, the critical pit depth for high strength low alloy steel is reported as 40µm (Kumakura et al. 1999) and 110µm (Ahn et al. 1992); for Al-alloys 2µm (Dolley et al. 2000), 30µm (Medved et al. 2004) and 60µm (Chlistovsky et al. 2007). These collected data suggest that other factors, as well as pit depth, are affecting the pit-to-crack transition.

It was reported (Pidaparti, R. M. and Rao 2008) that exposure duration did not affect the maximum stress at the pits for exposure time longer than 75 days. Pidaparti and Patel, R. K. (2010) also studied the stress around pits for different periods of exposure time for the corrosion of aluminium and concluded stress concentration factor (SCF) increased for the first half of the corrosion period and then it decreased. Horner et al. (2011) reported that an increase in exposure time does not affect the intensity of pits.

Lu and Luo (2006) studied the effect of stress level pit induced crack initiation and propagation in X70 steel in near neutral environment where it was concluded that the increase in the stress level will decrease the crack initiation life whereas it does not have an effect on propagation stage. Several lines of evidence suggest that pit's critical depth for crack initiation decreases with increasing the applied cyclic stress level (Dolley et al. 2000, Ishihara et al. 2006, Sankaran et al. 2001, Goto and Nisitani 1992). It has been shown by Chlistovsky et al. (2007) and Goto and Nisitani (1992) that at high stress amplitude the fatigue life of steel and Al-alloy specimens were independent of the presence of a corrosive environment (NaCl solution) and the large number of cracks initiated at slip bands rather than pits, whereas at low stress amplitudes the fatigue life reduced remarkably and corrosion pits were the origin of fatigue crack.

Cornet and GOLAN (1959) investigated the effect of corrosive solution temperature on fatigue life. They found that fatigue life has been higher at higher environmental temperature. They concluded that this was because higher temperature made more hemispherical and rounded shape pit than sharp pit shapes. Therefore the pit stress concentration factor has been lower at a higher temperature at 2.5% NaCl solution. The result reported by Fink et al. (1943) on the effect of temperature on corrosion fatigue is different with Cornet and GOLAN (1959). The difference in experimental condition used can be the cause of different conclusions in these two studies.

Murtaza and Akid (1996) (Murtaza and Akid, R 1996) studied the short crack growth behaviour of high strength steel in the air and in 0.6M NaCl solution under constant strain amplitude. The average surface crack length was measured using surface replicas and results indicated that the aggressive environment had a strong influence in

the early stages of crack growth. Crack initiation occurred at non-metallic areas revealing the key role of inclusions in CF crack initiation. Similar tests were carried out on silicon-manganese spring steel (BS250 A53) and the same result was observed (Murtaza & Akid 2000) (Murtaza and Akid, R 2000). It was observed that transition from short to long crack in air happened at 120 μm crack length while in the corrosive environment it occurred at 30-60 μm. In the examples cited, prior austenite grain boundaries play the role of a barrier for pit growth dependent on the applied stress. The authors conclude that most of the fatigue life (60%) was consumed by the pit and short crack growth. In these reports, only surface cracks were studied.

The definition of crack initiation has been a subject of debate for many years and thus far there is no universal consensus. Although some workers have defined crack initiation as the stage that newly formed cracks reach dimensions of the order of the grain size (Hertzberg et al. 2012), most approaches that attempt to model corrosion fatigue focus on the crack propagation stage rather than crack initiation (McEvily Jr 1990). Available models used to predict the fatigue crack initiation from corrosion pits (Goswami, T and Hoeppner, D. 1997, Arriscorreta 2012, Kondo 1989, Chen, G. et al. 1996, Sriraman and Pidaparti, R. 2010, Li, S.-X. and Akid, R 2013) are based on the transition criterion, which is defined using long crack growth rate data and linear elastic fracture mechanics (LEFM). These prediction models assume pits as small cracks and use LEFM criteria to predict long crack. This approach neglects the short crack initiation life, which should not be neglected especially in the high cycle fatigue regime (Ranganathan et al. 2011). Limitations in applying this criterion to short crack initiation from pits mean that determining a criterion for short crack initiation from a pit remains a major challenge (Burns et al. 2011). The proposed model in this project

(as will be discussed in Chapter 5) does not assume pits as a short crack, but rather as a notch, *i.e.* a stress concentration site. The available standard, such as DVN-RP-C203 for predicting the fatigue behaviour of oil and gas pipelines are based on LEFM approaches and fatigue tests in sea water. But they do not suggest prediction models for sour environment service condition.

Under cyclic loads, it is understood that notches often deform plastically and the short crack initiates from the plastically deformed zones (Stephens, R. I. et al. 2000, Hertzberg et al. 2012). Murtaza and Akid, R (2000) states that pit induced crack growth is not linear and is controlled by strain. It was observed in a subsequent fatigue study of steel that early crack nucleation and propagation is a result of an increase in the total strain (Fatoba and Akid, Robert 2014). It is noted in another study by Larrosa et al. (2015) and Xu and Wang, You-de (2015) that fatigue cracks initiate from the site of maximum plastic strain localisation. However, research on the pit-to-crack transition has been mostly restricted to considering plastic deformation around the pit, because the available models to predict crack initiation from corrosion pits assume corrosion pits as a crack. Consequentially, these approaches are based on stress intensity factor considerations and the LEFM concept, which is applicable only when small-scale yielding is assumed. As the embryonic corrosion pit size is of the scale of microstructure and the level of stress is high, small-scale yielding and linear elastic assumption may be unrealistic for the purpose of estimation of the crack initiation from corrosion pits. The size of the plastic zone around the notch may be similar to the dimensions of the microstructure and hence short cracks interact with the microstructure. It follows that fatigue crack initiation is controlled by local stress at the notch root, and stress intensity factor is not the controlling driving force for

crack initiation since the size of notch plastic zone and the microstructure are more significant for short crack initiation (Hertzberg et al. 2012). Clearly, fatigue life is more reliably estimated if using predictive models for both the crack initiation and crack propagation stages. In order to provide a more accurate prediction of the initiation phase, local stress field or cyclic strain approaches are of interest (Zhang, YM et al. 2016).

One approach for the improved prediction of crack initiation is to account for the elastic-plastic behaviour of materials and derive the local stress and strain behaviour at corrosion pits. Moreover, accurate calculation of stress and strain values could provide additional information to assess the influence of mechano-electrochemical effects on the pit-to-crack process and corrosion /corrosion fatigue in general (Sato 1971). The combined influences of mechanical and chemical/electrochemical effects (hereafter termed mechano-electrochemical effects) have been studied since the beginning of the 19th century (Gutman, E. M. 1994). Previous studies have focused on stress corrosion cracking, corrosion fatigue (Pan 2012) and hydrogen-induced cracking (Lu, B. et al. 2013). Despite the wealth of theoretical and empirical models and experimental data, there is no consensus on a general model to describe the synergistic effects of either elastic stress or plastic strain on electrochemical and corrosion processes.

In general, the influence of elastic stress on corrosion may vary significantly but is limited in magnitude for a given alloy-environment combination. The observed mechano-electrochemical effect is likely to be a combination of change in surface physical properties, microstructural heterogeneity and the deformation of oxide film induced by the external loading. By contrast, the influence of plastic strain is comparatively more significant and primarily related to the production of dislocations,

leading to enhancement of the anodic dissolution reaction at the alloy surface (Gutman, E. et al. 1996) and often enhancement of the hydrogen evolution reaction (Lu, B. et al. 2009).

The following Sections elaborate on the available corrosion pit fatigue crack models.

## 2.4 Linear Elastic Fracture Mechanics based models

Different models exist in the literature to estimate the critical pit size from which fatigue cracks may initiate and also to establish corrosion fatigue (CF) life. This section reviews these models. The advantages and limitations of each model are discussed.

### 2.4.1 Hoeppner model

In 1979, Hoeppner proposed a model to predict the fatigue life based on a pitting corrosion fatigue process involving the initiation of a mode 1 crack. The crack growth rate vs. stress intensity factor curve for pre-pitted aluminium alloy 2124-T851 specimens was used to obtain the empirical $\Delta K_{th}$. By using the term $K = 1.1\sigma(\pi a/Q)^{1/2}$ for the case of a hemispherical pit, the critical pit depth (*i.e.* that cracks initiate from pits) was determined and finally, the critical pit depth time was estimated (Goswami, Tarun and Hoeppner, D. W. 1999, Arriscorreta 2012):

$$t = (d/c)^3$$

where $d$ is the penetration depth, $t$ is the exposure time, $c$ is the material/environment constant, $\sigma$ is applied stress, $a$ is the hemispherical pit length and $Q$ is shape factor.

The model employs a linear elastic fracture mechanics (LEFM) approach and thus is only strictly valid where LEFM is applicable *i.e.* when a small scale yielding

condition is involved and the crack presence is assumed. The fatigue tests were only conducted in air and environmental (*i.e.* corrosion fatigue) tests were not conducted. Another issue with this approach is that it is not general and appears to be specific to aluminium alloy 2124-T851.

### 2.4.2 Lindley model

In 1982, Lindley (Lindley et al. 1982) considered a corrosion pit as a semi-elliptical surface crack, with the minor axis $a$ perpendicular to the applied stress and major axis $c$. The pit depth was not considered in the subsequent calculations. Irwin's stress intensity solution was used to determine the crack nucleation threshold stress intensity factor:

$$\Delta K_{th} = \frac{\Delta\sigma\sqrt{(\pi a)[1.13-0.07(a/c)^{0.5}]}}{[1+1.47(a/c)^{1.64}]^{0.5}}$$

By using the existing threshold stress intensity factor, the critical value of $a/c$ can be estimated. The model is material dependent and the pit assumed as a surface crack. In other words, the pit depth is not considered in the model. Problem arises with the use of this model where LEFM is not applicable.

### 2.4.3 Kawai and Kasai model

Considering a pit as an elliptical crack, this model uses the $da/dN$ vs. $\Delta K$ plot to determine the corrosion fatigue threshold stress intensity factor $\Delta K_{th}$ and then defines allowable stress under CF condition (Arriscorreta 2012):

$$\Delta\sigma_{th} = \frac{\Delta K_{th}}{F\sqrt{\pi h_{\max}}}$$

where $F$ is the geometry factor and $h_{\max}$ is the maximum pit depth.

As corrosion is not usually reflected in S-N curves, this model can be used under CF conditions to acquire the allowable fatigue stress. The same limitations exist as for the aforementioned models, *i.e.* material dependency and LEFM applicability.

It is further noted (Kawai and Kasai 1985, Buxton et al. 1992) that pit growth can be described by:

$$x = Bt^{\beta}$$

Where $x$ is the maximum pit depth, $t$ is the exposure time, $B$ and $\beta$ are material/environment constant. Turnbull, A et al. (2010) and Bhandari et al. (2015) defined pit growth similarly.

### 2.4.4 Kondo model

Kondo (1989) also used a fracture mechanics approach, by considering a pit as a sharp hemispherical crack and evaluating the critical pit condition at which the transition to crack occurs. This worker conducted CF tests on two specimens prepared from 2.5NiCrMoV and 3.5NiCrMoV steel and exposed to a corrosive environment in a test cell within a fatigue test machine. The proposed equations for pit size $c$ and pit growth rate $dc/dN$ are given as follows:

$$c = C_p t^{1/3} = C_p (N/f)^{1/3}$$
$$dc/dN = (1/3) C_p f^{-1/3} N^{-2/3}$$

where $c$ is the pit radius, $t$ is the time, $C_p$ is the coefficient reflecting the effect of the environment, $N$ is the number of stress cycles and $f$ is the frequency.

Using Newman-Raju's equation, the stress intensity factor range $(\Delta K)_P$ for critical pit was proposed as:

$$(\Delta K)_P = 2.24\sigma_a\sqrt{\pi c\alpha/Q}$$

where $\sigma_a$ is the cyclic stress amplitude, $\alpha$ is the pit aspect ratio $(a/c)$ and $Q$ is the shape factor.

Kondo used the intersect of the fatigue crack growth line in Figure 2.10 and pit growth line as a critical pit condition. It shows the pit-to-crack transition occurs when the fatigue crack growth rate exceeds the pit growth rate for which the critical pit size $c_{cr}$ is:



Figure 2.10. Model for transition into a crack from a pit (Kondo 1989).

The limitations of his work are the hemispherical shape assumption for the pit, the assumption of a pit as a sharp crack and the applicability of LEFM. The experiments were conducted for only two different pit sizes and the model is both material and environment dependent. In the Kondo model, the depth of the critical pit is assumed to be the same as the first crack initiated from the pit, which is a limitation because a crack may initiate from the pit mouth and subsequently the pit may be deeper than a crack.

### 2.4.5 Chen model

Chen, G. et al. (1996) investigated the CF behaviour of 2024-T3 aluminium alloy under different stress ranges and frequencies and suggested the following formula for pit-to-crack transition under LEFM criteria, using the assumption of the pit as a crack:

$$\Delta K_{tr} = \frac{1.12 k_t \Delta\sigma \sqrt{\pi c_{tr}}}{\Phi_{tr}} = \Delta K_{th}$$

$$\Phi = \int_0^{\frac{\pi}{2}} [\sin^2\theta + (c/a)^2 \cos^2\theta]^{1/2} d\theta$$

where $c, a, \phi$ are defined in Figure 2.11 and $\Phi$ is a shape factor, $k_t$ is the stress concentration factor (SCF) of the circular hole and $\Delta\sigma$ is the cyclic stress range.

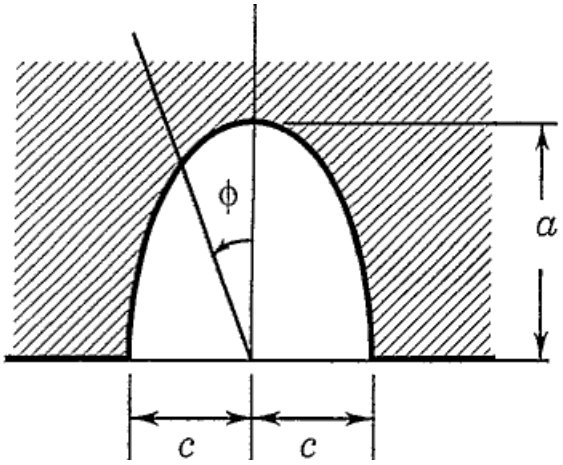


Figure 2.11. Schematic of an equivalent semi-elliptic surface crack modelled from corrosion pit causing fatigue crack nucleation.

The author also presented two criteria for pit-to-crack transition as:

$$1)\ \Delta K \geq \Delta K_{th}$$

$$2)\ \left(\frac{dc}{dt}\right)_{crack} \geq \left(\frac{dc}{dt}\right)_{pit}$$

These two criteria are used extensively in the literature (Horner et al. 2011, Li, S.-X. and Akid, R 2013, Turnbull, Alan 2014) .

### 2.4.6 Modified Hobson Model

The Hobson model was postulated in 1985 and was modified by Murtaza and Akid, R (2000). The Modified Hobson Model assumes the fatigue life to comprise pit development, CF short crack growth and CF long crack growth, as described by the following equations for each stage:

Pit development: $(da_p/dN)_{pcf} = C_p(a_{tr} - a_p),\ \ C_p = A_p(\Delta\gamma_t)^{\alpha_p}$

Short crack growth: $(da/dN)_{scf} = C_{scf}(d_i - a)$

Long crack growth: $(da/dN)_{lcf} = C_{lcf}a - D,\ \ C_p = B_{lcf}(\Delta\gamma_t)^{\beta_{lcf}}$

where $\Delta\gamma_t$ is the total shear strain range, $\alpha_p, C_{scf}, A_p, C_p, B_{lcf}, \beta_{lcf}$ are constants dependent on material and environment, $a$ is average surface crack length, $a_{tr}$ is transition crack length, $a_p$ pit length, $d_i$ grain size and $D$ the threshold crack growth rate.

This model is based on LEFM and is material and environment dependent.

### 2.4.7 The superposition model

This model was initially proposed in 1969 and was subsequently modified by Wei and Gao, Ming (1983). In the Superposition Model (SM), the total fatigue crack growth rate is the sum of Air Fatigue Crack Growth (AFCG) plus Environment-Assisted Crack Growth (ECG) (Murtaza and Akid, R 2000). AFCG represents the mechanical driving force which depends on strain whereas ECG is determined by the chemical driving force caused by the interaction of the aggressive environment and material. This model is expressed by:

$$(da/dN)_{cf} = (da/dN)_a + (da/dN)_e$$

where $(da/dN)_{cf}$ is the CF crack growth rate, $(da/dN)_a$ is the calculated fatigue crack growth rate in air and $(da/dN)_e$ is the environmental crack growth rate, evaluated by following equations for short and long fatigue crack growth rates, respectively:

$$(da/dN)_{se} = A_e(\Delta\gamma_t)^{\alpha_e} a^{-b_e}$$

$$(da/dN)_{le} = A_e(\Delta\gamma_t)^{\beta_e} a$$

where $\Delta\gamma_t$ is the total shear strain range, $\alpha_e$, $b_e$ and $\beta_e$ are constants depending on material and environment. Similar to the previously outlined models, this model is material/environmental dependent and LEFM based.

### 2.4.8 Sriraman & Pidaparti model

Sriraman and Pidaparti, R. (2010) considered the influence of corrosive environment and cyclic loading and describes a model to predict the critical pit depth ($a_{pc}$) and the number of cycles ($N_i$) for the pit to reach the critical length ($a_{pc}$):

$$a_{pc} = \pi\left(\frac{\Delta k_{th}}{4.4K_t\sigma_a}\right)^2$$

$$N_i = \frac{2\pi nF\rho}{3M}(f)\left[\pi\left(\frac{\Delta k_{th}}{4.4K_t\sigma_a}\right)^2\right]^3\left(\frac{1}{I_p}\right)\left(\frac{1}{C^{\sigma_a}}\right)^3$$

where $n$ is the number of electrons released during corrosion of the metal, $M$ is the atomic mass of the material, $F$ is Faraday's constant, $f$ is the frequency, $\rho$ is the material mass density, $I_p$ is the pitting current, $K_t$ is the SCF of a circular hole and $C^{\sigma_a}$ is the factor reflecting the influence of stress.

One of the principal advantages of this model is that it considers the effect of pitting corrosion current as well as fatigue stress. The model was validated by experimental results from literature for aluminium alloy 2024-T3 and 12%Cr stainless steel, but these experimental data were limited and further experiments are required in order to validate the model. The primary limitations of the work are the use of hemispherical and the assumption of instantaneous pitting.

### 2.4.9 Li and Akid

Li, S.-X. and Akid, R (2013) attempted to develop a model for the fatigue life prediction using medium strength structural steel specimens; with tensile strength and yield strength of 610MPa and 375MPa respectively, with an emphasis on the effect of initiation and evaluation of corrosion pits. Dog-bone shaped specimens were made from carbon steel. Pits with an aspect ratio (a/2c) around 0.11 were produced on some specimens, using a commercial Scanning Droplet Cell. A series of fatigue tests were performed at room temperature in both air and 3.5% NaCl in a corrosion cell under identical loading conditions. In order to measure crack growth at a selected number of cycles, replicas were taken from the surface of specimens and S-N curves were obtained. The results from the S-N curves indicated fatigue life in the air or 3.5% NaCl reduced by over 60% due to the presence of pits. Of particular note in this study is that the lifetime of non-pitted specimens tested under CF condition was less than pitted specimens fatigued in the air, which demonstrates the impact of a corrosive environment on fatigue lifetime. This paper simplified the description of the CF process into pit growth $N_{pit}$, small crack growth $N_s$ and long crack growth $N_l$ resulting in a total fatigue lifetime. The authors suggested the following formulae for each stage in the life prediction based on experimental data:

$$N_{pit} = \left(\frac{a_{pc}}{A}\right)^{1/B}\left(\frac{10^{9.19}}{e^{0.036\sigma_a}}\right)$$

$$N_s = \int_{a_{pc}}^{a_{tr}} \frac{1}{C_s(\Delta K)^{m_s}} da$$

$$N_l = \int_{a_{tr}}^{a_f} \frac{1}{C_l(\Delta K)^{m_l}} da$$

The critical pit size was also defined as:

$$a_{pc} = \pi\left(\frac{\Delta K_{th}}{4.4K_t\sigma_a}\right)^2$$

Comparing the model with experimental data, the model provides conservative predictions at high stresses; however, a good agreement is acquired in the low stress regime. Their results are also in strong agreement with previous work (Akid, R 2010). The main limitation of this study is the assumption of semi-circular shape for pits. No consideration is given to different pit aspect ratios and plastic behaviour of cracks. This model is also material and environment dependent.

## 2.5 Empirical models for crack initiation to total fatigue life

### 2.5.1 Khan and Younas

Khan, Z. and Younas (1996) used the initiation-propagation model to predict the CF life of aluminium alloy in Persian Gulf sea water. The following equations were used for the initiation and propagation stages respectively:

$$\frac{\Delta\varepsilon}{2} = \frac{\sigma'_f}{E}\left(2N_f\right)^b + \varepsilon'_f\left(2N_f\right)^c$$

$$\frac{da}{dN} = \frac{C\Delta K^m}{(1-R)K_c - \Delta K}$$

where $\Delta\varepsilon$ represents the strain life, $\sigma'_f$, the fatigue strength, $\varepsilon'_f$, the fatigue ductility coefficient, $b$ and $c$, fatigue exponents, $K_c$, fatigue toughness.

Good agreement was found with experimental results. In this model, plastic strain is considered in the initiation stage, but the authors made no attempt to study the effect of pitting potential. As it is seen in other studies, the authors observed that in high

cycle fatigue most of the fatigue time is dominated by crack initiation stage but in low cycle region it is dominated by propagation. In other words, in the low cycle region cracks initiates earlier than is the case for the high cycle region.

### 2.5.2 Rokhlin model

Rokhlin et al. (1999) divided fatigue life into two stages; stage one being the time in which the crack extends from the root of the pit and propagates into a single semi-elliptical crack and stage two is the remaining time to failure. Based on a two-stage fatigue life and fatigue tests on ten 2024-T3 aluminium alloy specimens; each of which containing a central artificial pit with the depth of 170μm and diameter of 240μm, an empirical relation (Figure 2.12) has been suggested to show the relation between the depth of corrosion pit and the fatigue life:

$$N = N_{th}(d/h)^{-3/4}$$

where $N$ is the fatigue life, $N_{th}$ is the fatigue life of the specimen with a through-thickness hole, $d$ is the pit depth and $h$ is the specimen thickness. The model developed is in agreement with experimental results. This model can be used to predict the fatigue life of the specimen containing a random pit only when the experiments indicated the fatigue life of the specimens with through-thickness hole ( $N_{th}$ ).

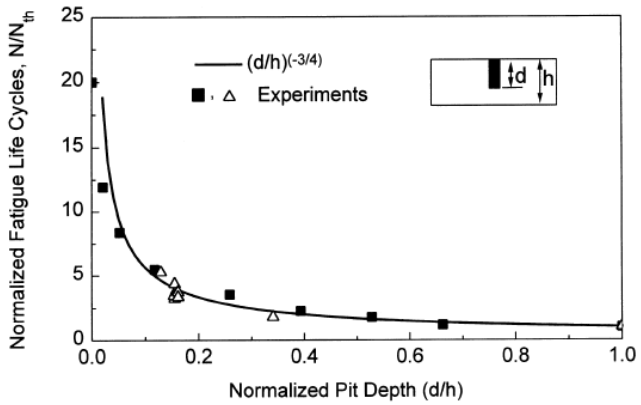


Figure 2.12. Empirical relation obtained from experiments.

A limitation of this work is that the fatigue tests were stopped after a specified number of cycles and then the tensile load was applied until failure. As a result, the model may be considered to be unrealistic. Being restricted to testing using a single stress amplitude and frequency, the study is also limited in terms of investigation of different pit sizes. In spite of the vital role of corrosive environment in determining fatigue lifetime, the tests were carried out in the air.

### 2.5.3 Hu and his co-workers

Hu et al. (2014) described an equation based on Faraday's law to estimate the pit growth time in oil pipelines:

$$t_{pit} = \frac{2\pi nF\rho_0 Z^2}{3MI}(c_0^{\,3} - R_z^{\,3})$$

where $n$ is the number of electrons released during corrosion of the metal, $M$ is the atomic mass of the material, $F$ is the Faraday's constant, $\rho_0$ is the material mass density, $c_0$ is the critical length of crack initiation, $I$ is the corrosion current density,

$R_z$ is the micro roughness of pipe surface and $Z$ is the length/width ratio of the oval shape.

The electrochemical influence is considered but the fatigue stress has not been taken into account.

## 2.6 Finite Element models

This Section is concerned with FE studies of pitting corrosion, which has been validated widely in the literature to characterize the corrosion pits (Kolios et al. 2014). In recent years, there has been an increasing interest in using FEA because of benefits such as a reduction in the cost and time consumed in empirical work.

Turnbull, A et al. (2010) performed elastic-plastic FEA of stress and strain distribution around a single pit in a cylindrical steel specimen under a static tension load. Simulated pits were hemispherical or U-shaped with the depth of 100 or 500 μm. Second order 4-node linear tetrahedral elements were created with a fine mesh around the pit to improve the accuracy. To define the boundary condition, one end of the specimen was fixed and the other end was subjected to a uniform static tension stress equal to 90% or 50% yield strength. The observed maximum stress area in FEA results was seen as an extended area down the sides of a pit. In addition, the plastic strain localisation was seen near the pit mouth. X-ray tomography measurements were carried out on actual pits and the cracks were observed from the real tensile tested specimens. It is reported that the cracks initiated from the area below the pit mouth. Previous studies (Cerit, M et al. 2009) assumed that the crack would propagate from the pit base, but this study (Turnbull, A et al. 2010) predicted that the crack might grow from the area below the pit mouth. Good agreement was shown with X-ray

tomography measurements on the specimens. It was observed that the stress localisation at higher stress ranges occurs at the pit base and leads to plastic strain localisation near the mouth due to the effect of minimum constraint (Turnbull, A. et al. 2009, Horner et al. 2011). This observation highlights the importance of strain localisation sites as a likely place for stress corrosion crack initiation. In other elastic-plastic simulations of buried pipelines, plastic deformation was similarly noted as the responsible factor for pipe wall fracture (Rajabipour and Melchers 2013). As the tip of small cracks shows plastic behaviour, the strength of this FE analysis lies in consideration of the plastic strain.

Zhang, X.-Y. et al. (2013) studies stress concentration factor (SCF) for different pit aspect ratios by using the elastic material model in ABAQUS. FE analysis revealed that the effect of pit depth on SCF was more than the effect of pit width, which is inconsistent with studies by Larrosa et al. (2015) and Xu and Wang, You-de (2015) and Ok et al. (2007). When the aspect ratio was less than unity, an increase in aspect ratio enhanced the SCF value but it had almost no effect on SCF when it exceeded unity. From this FE study, we can see that the maximum stress is not always at the bottom of corrosion pits and it moves toward the pit mouth as the aspect ratio increases. In empirical tests by Zhang, X.-Y. et al. (2013), the SCF values were found to be significantly influenced by aspect ratio when the aspect ratio was less than unity. The aspect ratio had almost no effect on SCF when it was higher than a value of 2. A study by Cerit, Muhammet (2013) assumed the semi-elliptical pit shape in FE models and observed when pit aspect ratio is less than 2.5; the higher aspect ratio resulted in higher SCF but for aspect ratios more than 2.5 there was no change in the SCF. The effect of aspect ratio and pit shape on SCF was also studied by Cerit, M et al. (2009)

resulting in a similar relationship. These workers reported that pit aspect ratio, loading condition and environment affect the location of crack initiation. In other work concerning elastic-plastic simulation of buried pipelines, pit aspect ratio was also noted as an influencing factor on pipe wall fracture (Rajabipour and Melchers 2013).

The influence of secondary pitting at the bottom of a primary pit on SCF was investigated by Cerit, M et al. (2009) and Cerit, Muhammet (2013) using linear elastic FEA. Results indicated that SCF increases significantly within the secondary pit.

Paik et al. (2004) examined the effect of number of pits (pit intensity) on strength of material using nonlinear FE analysis. Results showed the greater the corrosion pit intensity, the larger the localised plasticity.

Many studies have used the linear elastic material model in FEA and therefore stress concentration factor to study the stress distribution around pits (Pidaparti, R. M. and Rao 2008, Cerit, M et al. 2009, Pidaparti, R. M. and Patel, R. K. 2010, Mu et al. 2011, Cerit, Muhammet 2013, Kolios et al. 2014, Ahmmad and Sumi 2010, Xu and Wang, You-de 2015, Ji et al. 2015), although none related to X65 steel. However, as the pit size is of the scale of microstructure, the linear elastic material model assumption may be unrealistic in any simulation of pit behaviour. With the exception of Refs 94 and 98, another limitation of these previous studies is the use of an ideal smooth pit shape, which does not allow evaluation of the real distribution of stresses and strains around the pits. Also, no studies thus far have attempted to consider the effect of microstructure on stress and strain distribution and all of them have used an isotropic material model.

## 2.7 X-ray tomography

Previous studies have investigated the pit-to-crack transition stage using ex-situ surface methods such as optical microscopy or Scanning Electron Microscope (SEM) to probe the exterior of the material intermittently during and after fatigue testing (Turnbull, A and Zhou 2004, Xu and Wang, You-de 2015, Van der Walde and Hillberry 2007, Jones and Hoeppner, D. W. 2006). However, these surface-based two dimensional (2D) approaches are quite limited and observation and monitoring of cracks initiated inside the materials are not possible using this approach (Wu et al. 2017). In recent years there has been an increasing interest in characterising materials using laboratory-based or synchrotron-based X-ray Computed Tomography (CT) and the applicability of this technique in materials science and medicine is well established (Patterson et al. 2016, Withers, P. J. and Preuss 2012). By Using X-ray, it would be possible to observe the features internal to the structures. It has made it possible to create three-dimensional (3D) representations of the structures. The images are made in X-ray microscopes based on the transmission of X-ray by the sample. The images are darker where the sample absorbs more X-ray and it is brighter where the sample transmits more X-ray. The higher the density and thickness, the higher the absorption is. In X-ray Computed Tomography (XCT) the sample is placed between X-ray source and detector. Then it rotates 180 or 360 degree and continuous images are taken from the sample while it is rotating. Each image at one particular angle is called projection. All projections are used by computer algorithms to reconstruct the 3D of the samples. A full model of the material can be made by XCT from millimetre to nanometre resolution and the voids and cracks can be visualised at this scales. Depending on the obtained resolution and the size of features, some features may be missed in the

images. One obvious advantage of this approach is that it is a non-destructive method. Synchrotron-based X-ray CT has been used to study the mechanical performance of materials under static loading (Qian et al. 2008, Toda, Hiroyuki et al. 2011, Maire, Eric et al. 2016, 2007, Cordes et al. 2015, Patterson et al. 2016), cyclic loading (Williams et al. 2011, Khor et al. 2004, Qu, P et al. 2009, Zhang, H et al. 2009, Ludwig, W et al. 2003, Proudhon et al. 2012, Ignatiev et al. 2006, Wu et al. 2016, Marrow et al. 2004) and even to evaluate the localised corrosion rate of inclusions in alloys (Singh et al. 2014). However, the availability of the synchrotron beamlines is limited and thus is an issue (Buffiere, Jean-Yves 2017). Horner and co-workers (Horner et al. 2011) utilized *ex-situ* laboratory-based X-ray tomography to characterize the cracks initiated from corrosion pits under tensile loads. Lu, X. et al. (2018) utilised Laboratory based X-ray tomography to characterise the crack in an elephant dentin. They were able to see the ligament bridging lateral to the crack front in X-ray computed tomography slices. Laboratory-based X-ray was also used in other studies to identify the corrosion process of the alloys in 3D (Lu, X. et al. 2018) and to monitor damage accumulation in a bone under increasing compressive load (Mustansar et al. 2017).

## 2.8 Summary of the state-of-the-art

In this chapter the corrosion, corrosion pitting in oil and gas industry and corrosion fatigue were reviewed. Predictive models for the pit-to-cracking life under fatigue loads are reviewed under the two approaches: the Linear Elastic Fracture Mechanics and empirical methods (S-N, strain-life). Modern X-ray Computed Tomography has improved the ability to characterise the material through three dimensional observations.

Pit-to-crack transitions under static loading have been investigated numerically and experimentally in previous studies (Horner et al. 2011, Cerit, Muhammet 2013, Turnbull, A et al. 2010, Mu et al. 2011, Cerit, M et al. 2009, Paik et al. 2004, Turnbull, A et al. 2006, Turnbull, A. et al. 2009, Rajabipour and Melchers 2013, Kolios et al. 2014). However, in spite of the importance of cyclic loading in reducing the life of components, the variation of local stress around corrosion pits under fatigue loading and its influence on fatigue life prediction have not been established. This issue constitutes a significant knowledge gap in the understanding of the pit-to-fatigue crack transition process. Understanding the mechanism involved in this transition and the initial development of the crack has the potential to improve the prediction of fatigue life (Figueiredo et al. 2015). In reviewing the literature, it became apparent that no previous work was performed on finite element analysis (FEA) of corrosion pits under the cyclic loading.

To the best of the author's knowledge, no studies have been conducted to (a) conduction of small-scale corrosion fatigue tests using specimens presenting a single defined pit exposed to an aqueous sour environment, and (b) utilization of laboratory-based X-ray CT to monitor the nucleation of fatigue cracks induced from corrosion pits during *in-situ* corrosion fatigue tests. The corrosion fatigue vessels reported in Section 2.2 were not suitable for the purpose of *in-situ* X-ray tomography or for the corrosion fatigue test in an environment consisting of toxic gas. Consequently in this work, an environmental apparatus and procedure was developed to facilitate the aforementioned tests and thereby visualise the initiation of a fatigue crack from a corrosion pit in X65 steel using X-ray CT were carried out. To acquire tomography data during experiments, a novel '*in-situ* interrupted test' protocol was developed

whereby the test specimen under load was imaged at defined intervals. The design features and representative results from experiments are presented in future Sections and the advantages and limitations of this approach are discussed.

# Chapter 3: Experimental

## 3.1 Material

The material of interest in this study is seamless API-5L X65 grade pipeline steel that was provided by the industrial sponsor. The chemical composition was obtained by optical emission spectroscopy at TWI Ltd. and the mechanical properties were obtained from the literature (Fatoba and Akid, Robert 2014), both of which are shown in Table 3.1 and 3.2 respectively. Although the composition of the steel used in this work is not exactly the same as that given for X65 steel in Ref. (Fatoba and Akid, Robert 2014), the difference does not affect the mechanical properties of the material.

Table 3.1: Chemical composition of API-5L X65 steel (mass %).

| C | Si | Mn | Mo | Cr | P | Cu | S | Ni | V |
|---|---|---|---|---|---|---|---|---|---|
| 0.06 | 0.11 | 1.38 | 0.21 | 0.27 | 0.01 | 0.027 | 0.002 | 0.022 | 0.053 |

Table 3.2: Mechanical properties of API 5L-X65 steel (Fatoba and Akid, Robert 2014).

| Monotonic load | | Cyclic load | |
|---|---|---|---|
| Elastic modulus, $E$ (GPa) | 211.33±0.6 | Fatigue Strength Coefficient, $\sigma'_f$ (MPa) | 801.8 |
| Upper Yield Strength, $YS_U$ (MPa) | 520±2 | Fatigue Strength Exponent, $b$ | -0.068 |
| Lower Yield Strength, $YS_L$ (MPa) | 516±4.4 | Fatigue Ductility Coefficient, $\varepsilon'_f$ | 0.372 |
| Ultimate Tensile Strength, $\sigma_{UTS}$ (MPa) | 614±3.4 | Fatigue Ductility Exponent, $C$ | -0.584 |
| Percentage Elongation, %*E1* | 15.72±0.9 | Cyclic Yield Strength, $YS'$ (MPa) | 420 |
| Strength Coefficient, $K$ (MPa) | 910±8.05 | Cyclic Strength Coefficient, $K'$ (MPa) | 923 |
| Strain Hardening Exponent, $n$ | 0.127 | Cyclic Strain Hardening Exponent, $n'$ | 0.118 |
| True Fracture Strength, $\sigma_f$ (MPa) | 1034 | | |

The engineering stress-strain curve of X65 steels was obtained from tensile tests data carried out at TWI Ltd. and the true stress ($\sigma_T$)-strain ($\varepsilon_T$) was calculated using equation 3.1 and 3.2. Both curves are shown in Figure 3.1. The cyclic true stress-strain curve was obtained from the literature (Figure 3.2).

$$\sigma_T = \frac{\sigma_E}{(1-\nu\varepsilon_E)^2} \tag{3.1}$$

$$\varepsilon_T = \ln(1+\varepsilon_E) \tag{3.2}$$

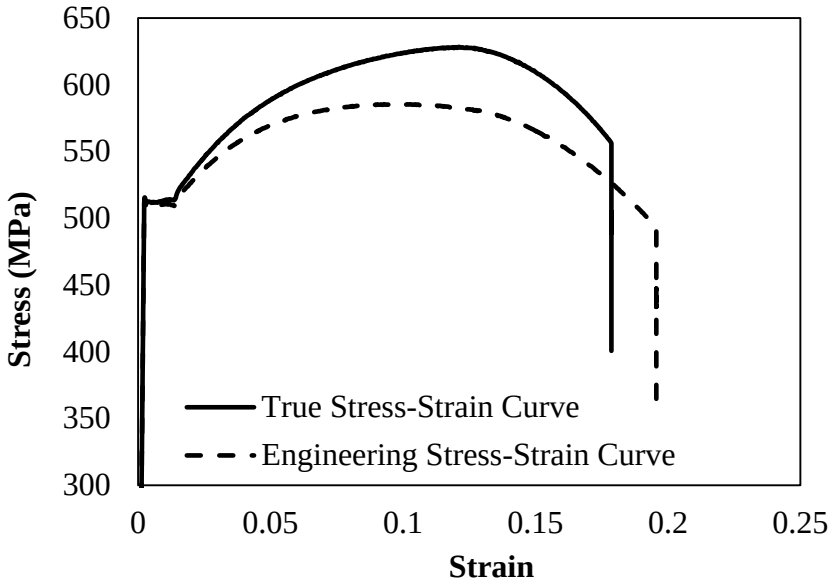


Figure 3.1. Monotonic stress-strain curves for X65 steel pipeline.

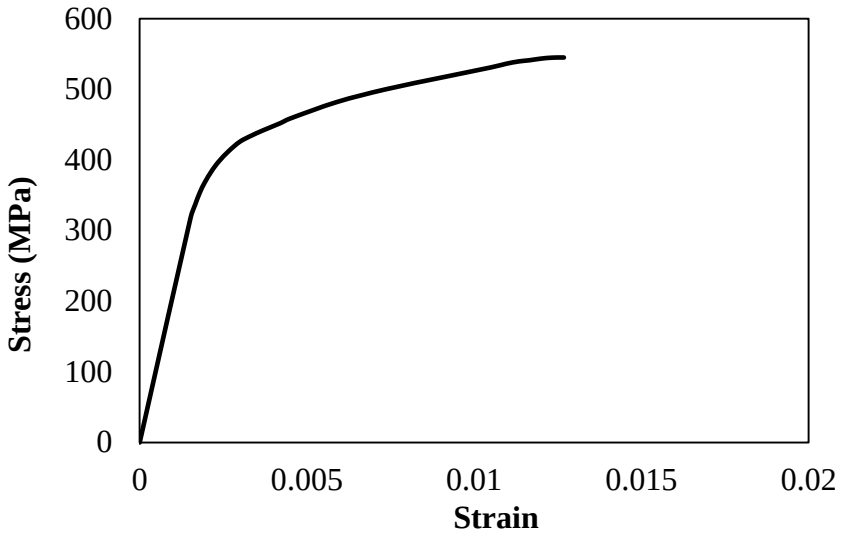


Figure 3.2. The stress-strain curve for X65 steel pipeline under cyclic loading (Fatoba and Akid, Robert 2014).

Figure 3.3 shows the microstructure of material as visualized by light optical microscopy, for specimens extracted in the longitudinal, transverse and short transverse directions of the pipe, as shown in Figure 3.4. The average grain size was determined to be in the range 3-7 μm (Hashemi 2011).

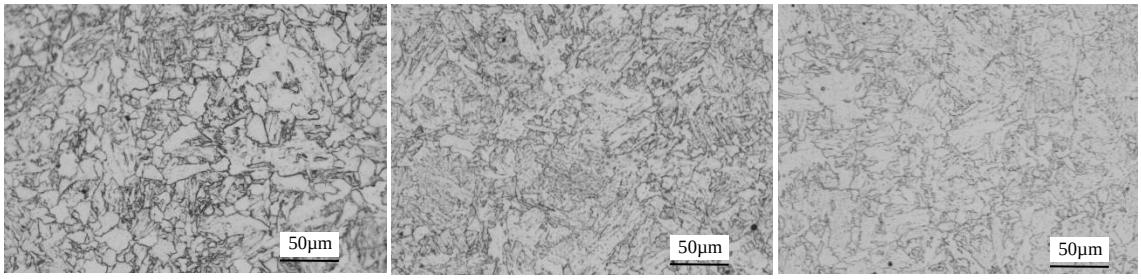


(a) (b) (c)

Figure 3.3. Optical micrographs of API-5L X65 pipeline steel microstructure in a) longitudinal (L), b) short transverse (S), c) transverse (T) directions of pipe.

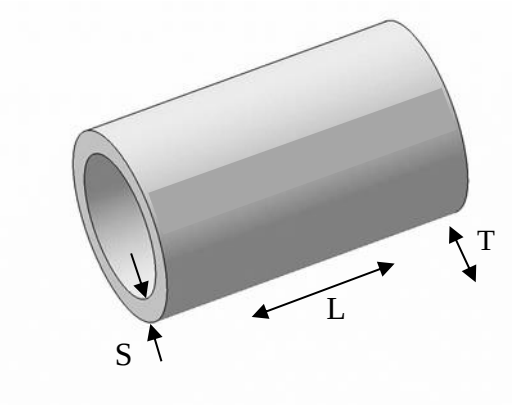


Figure 3.4. Longitudinal (L), transverse (T) and short transverse (S) directions of the pipe.

## 3.2 Pre-pitting the specimens using an electrochemical cell

The specimens used in fatigue tests (defined in Section 3.3 and 3.5) were pre-pitted using a micro-electrochemical cell built at TWI Ltd. The electrolyte used during these studies was 3.5% NaCl solution (in ambient air). Figure 3.5 shows the main components of the electrochemical workstation including the electrochemical microcell and Figure 3.6 is a close-up view of the microcell. The cell was installed on a VersaSCAN device that allows precise positioning of the cell along three orthogonal axes. A standard three-electrode configuration (i.e. working, counter and reference electrodes) was employed, using a platinum wire as the counter electrode and an Ag/AgCl reference electrode. All the electrodes are attached to VersaSTAT 4. Both the VersaSCAN and VersaSTAT 4 potentiostat were controlled using VersaStudio software and a laptop PC. The purpose of the microcell is to control the size of the wetted area of the specimen surface, by using a micro-capillary to form a droplet that can be positioned on the specimen surface and thus enable the electrochemical corrosion process. A video camera accessory is used to accurately position and monitor the droplet at the specimen surface prior to and during the electrochemical

corrosion (i.e. pitting) process. Figure 3.7 shows a close-up view of a pre-pitted specimen. The experiments can be configured in order to apply and maintain either a constant current (galvanostatic control) or constant potential (potentiostatic control) to the specimen. In this study, both the galvanostatic and potentiostatic methods were investigated for the purpose of creating single pits of desired sizes and shapes on the specimens. Initial galvanodynamic and potentiodynamic scans were performed in order to select appropriate current and potential values for subsequent work. Figure 3.8 and 3.9 show the obtained galvanodynamic and potentiodynamic scans. The red arrows indicate the selected current (200μA) and potential (1V) values located in the stable area of the curve. Figure 3.10 and 3.11 show the evolution of galvanostatic and potentiostatic data obtained as a function of time, during polarisation and pitting of the specimens. Following polarisation, the specimens were placed in a Pyrex glass beaker containing acetone and cleaned by ultrasonication. The as-grown pits were characterised using an Alicona Laser Scanning Confocal Microscope. The pit depth and lateral dimensions were recorded across four directions as shown in Figure 3.12. The average of the measured values for the four profiles was used to define the final depth and width of pits. A representative confocal microscopy scan and a 2D-cross-sectional profile are shown in Figure 3.13 and 3.14 respectively.

The obtained pit geometry using this method were  real in-service data provided by the industrial sponsor (i.e. data collected using Non Destructive Testing (NDT) methods on steel production risers The pits generated using these method are similar to the pits seen on the internal surface of the pipes as observed in samples provided by industrial sponsor of this project.

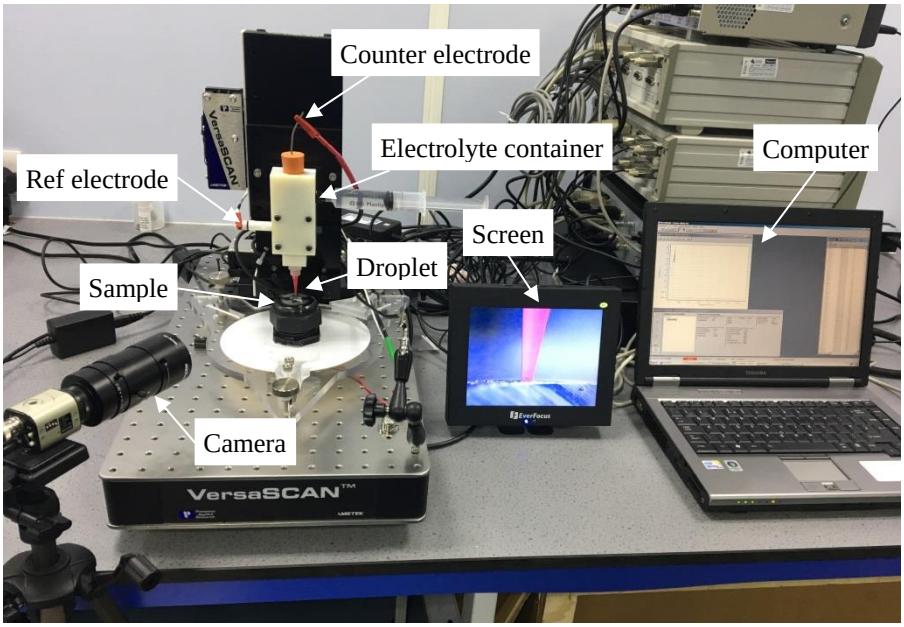


Figure 3.5. Overview of the micro-electrochemical apparatus used to create the corrosion pits.

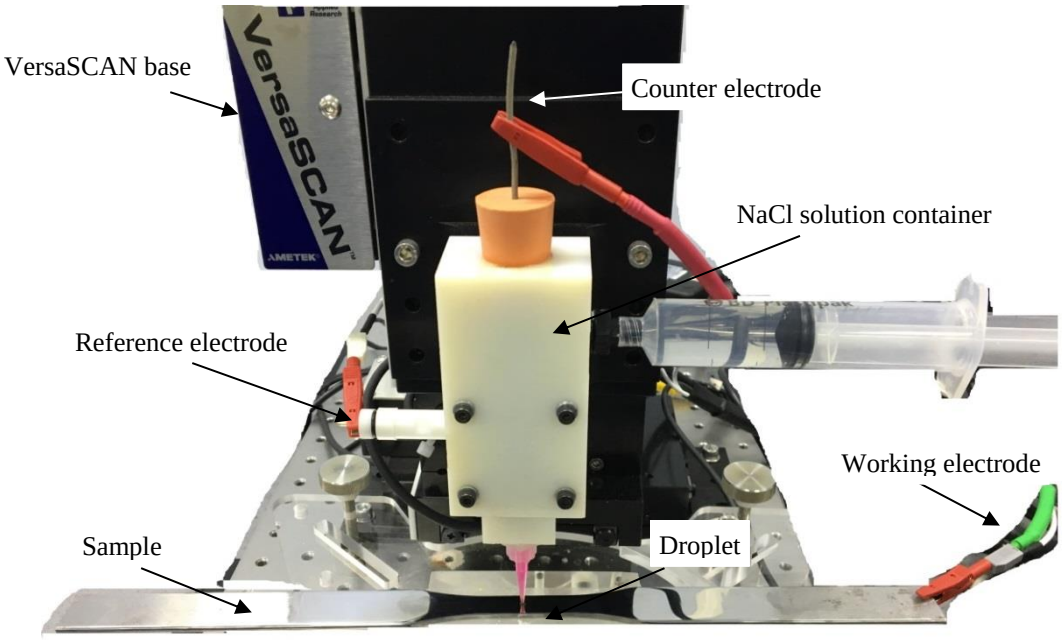


Figure 3.6. Close-up view of the electrochemical micro-capillary cell used to create a single corrosion pit.

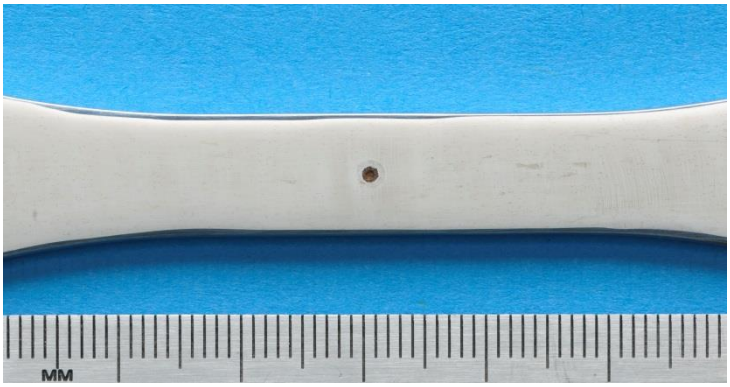


Figure 3.7. Close-up view of a pre-pitted specimen.

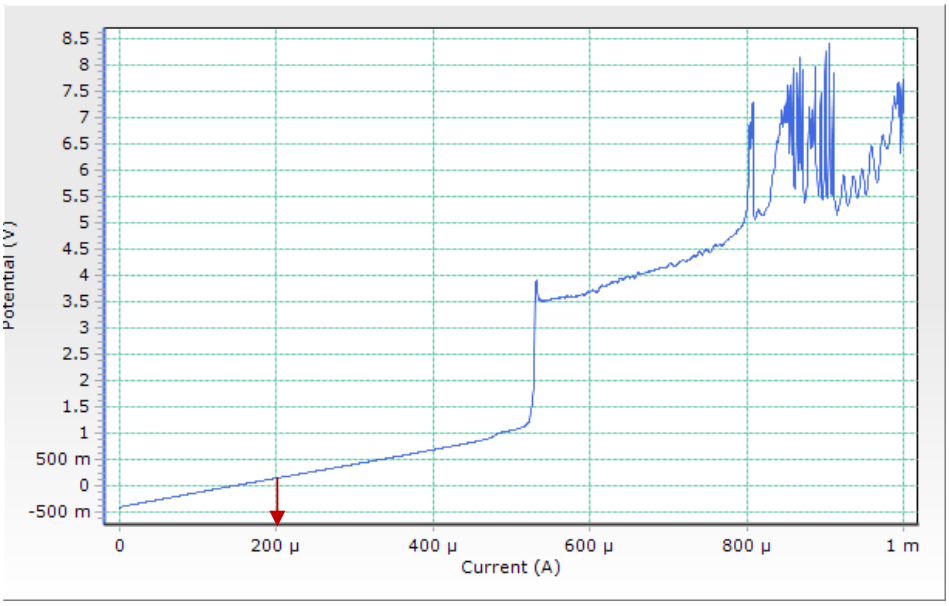


Figure 3.8. Galvanodynamic polarisation plot indicating the current value of 200µA (red arrow) selected for subsequent galvanostatic polarisation studies

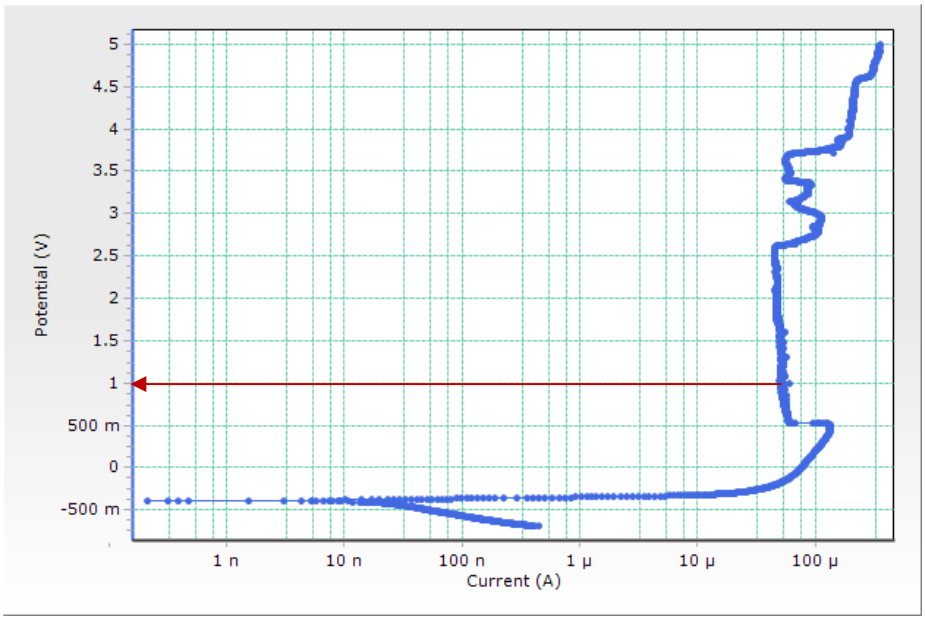


Figure 3.9. Potentiodynamic polarisation plot indicating the potential value of 1V (red arrow) selected for subsequent potentiostatic polarisation studies.

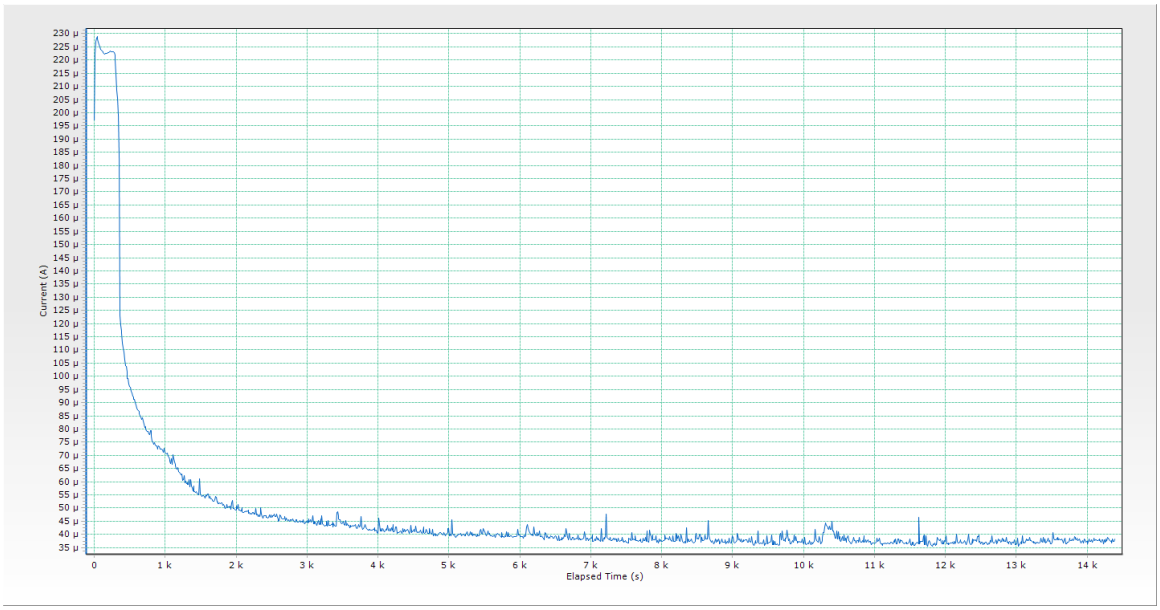


Figure 3.10. The galvanostatic curve obtained during polarisation.

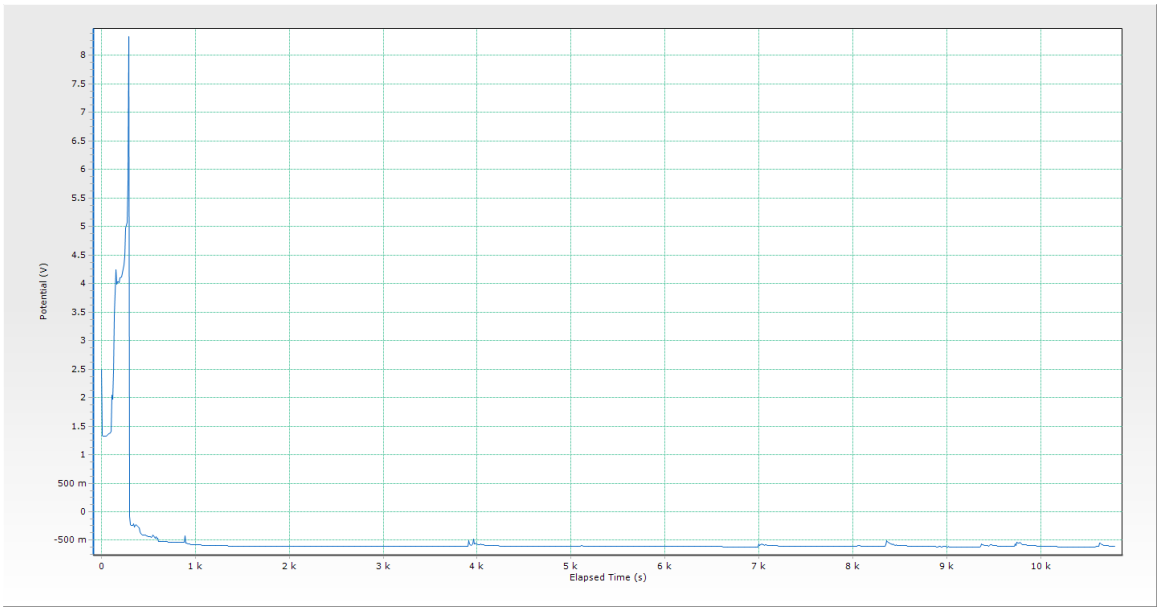


Figure 3.11. The potentiostatic curve obtained during polarisation.

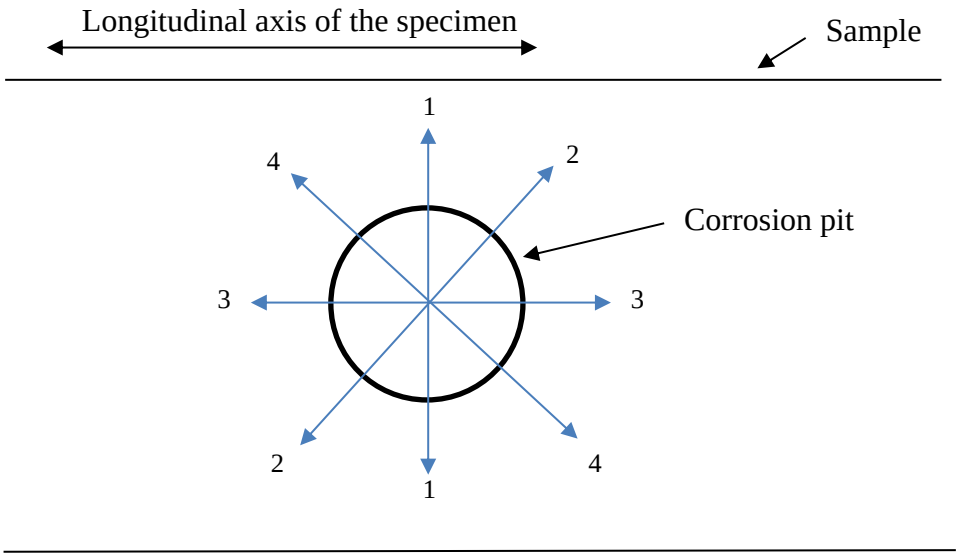


Figure 3.12. Schematic showing the directions of each profile taken from confocal microscopy scan to measure the pit depth and pit width.

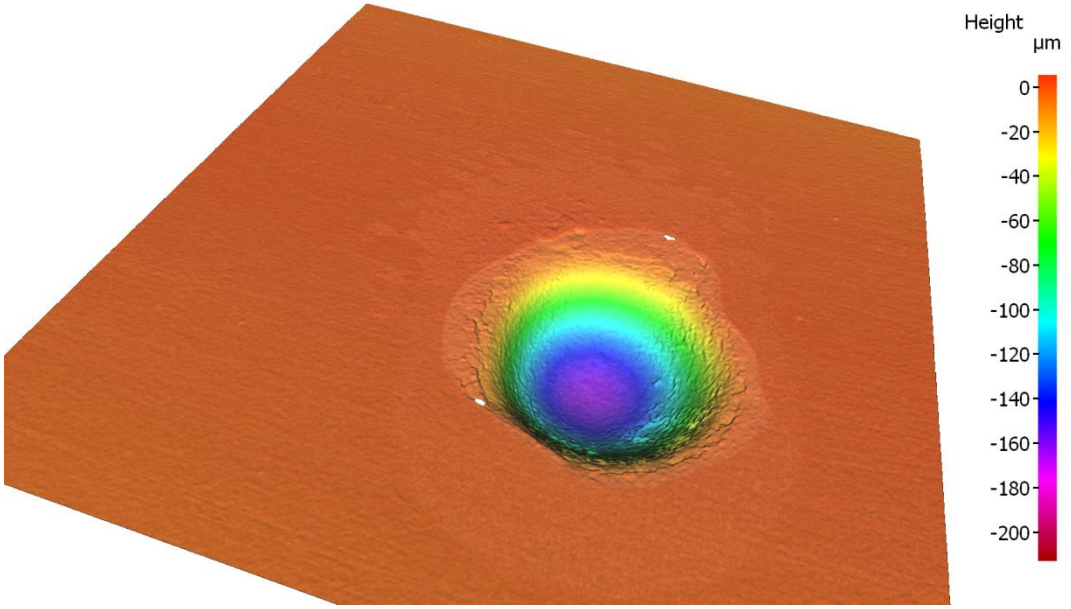


Figure 3.13. Confocal microscopy scan of a pit.

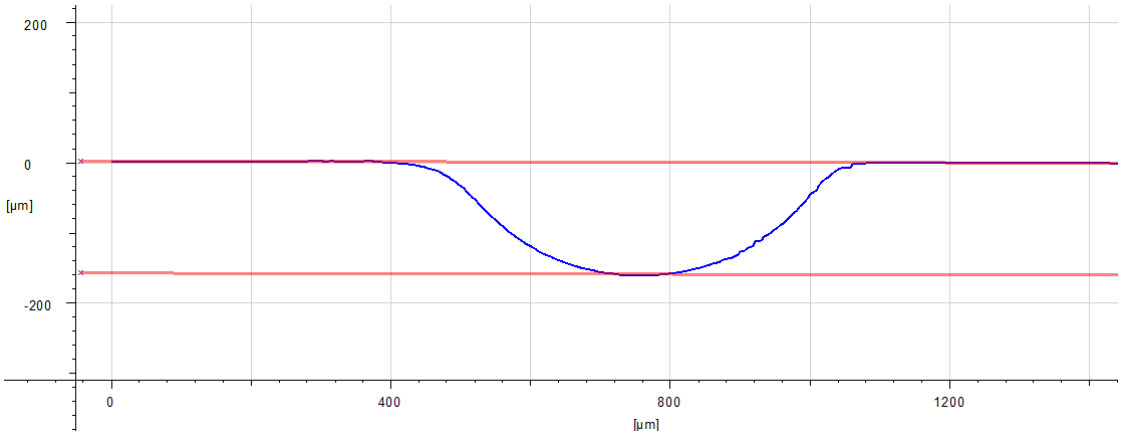


Figure 3.14. A profile taken from confocal microscopy scan of a pit for measuring pit depth and width.

## 3.3 Fatigue tests in the air on smooth specimens and pre-pitted specimens

There is a paucity of published data on the cyclic mechanical behaviour of X65 steel, therefore to assess the relationship between applied stress amplitude and the number

of cycles to failure (S-N curve) in X65 steel, load controlled fatigue tests were carried out. Flat smooth specimens were designed in accordance with ASTM E466 (Figure 3.15) and machined from the longitudinal length of the pipes provided by the industrial sponsor (Figure 3.16).

The seamless pipe had an outer diameter of 273mm and wall thickness of 29mm. Only parent material remote from the girth weld was used in the present study. The surface of all specimens was ground with papers to a 4000 grit finish and polished longitudinally with 3µm diamond to minimise the potential effects of residual stress and surface roughness on fatigue behaviour (Figure 3.17).

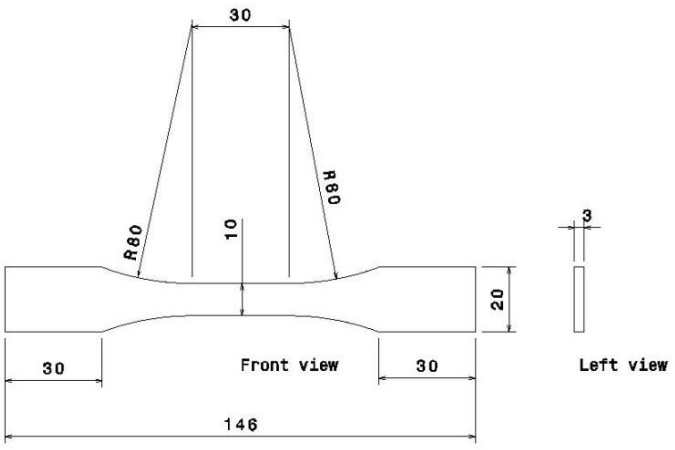


Figure 3.15. Test specimen geometry and dimensions (mm).

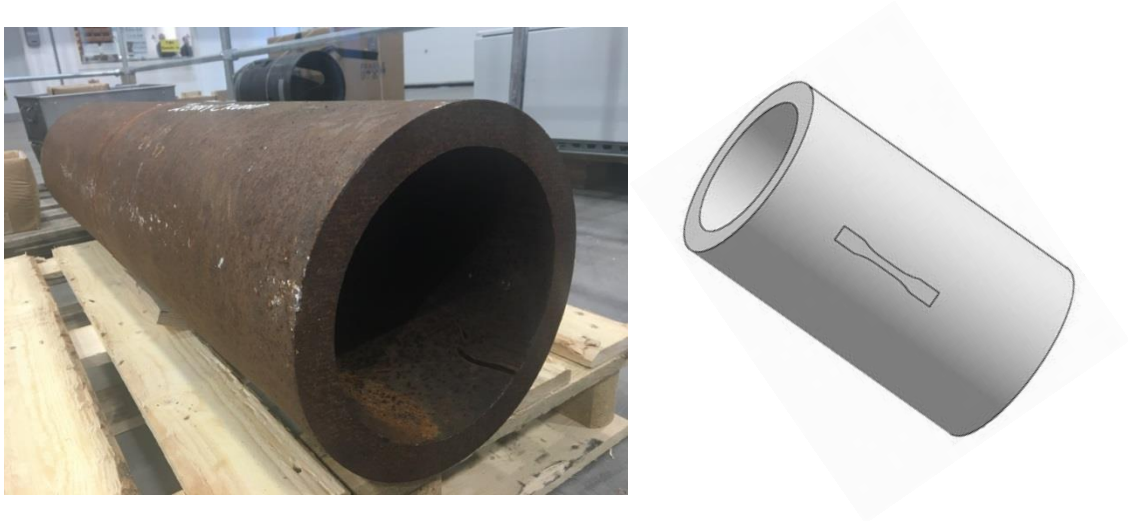

(a) (b)

Figure 3.16. (a) As-received X65 seamless pipe with outer diameter of 273mm and wall thickness of 29mm. b) Schematic to show orientation of test specimens extracted from pipe.

Figure 3.17. Polished specimens.

Five smooth specimens were tested using sinusoidal tension-compression cyclic loading (stress ratio of -1) at a frequency of 10Hz and different stress amplitudes in the range 150MPa to 280MPa. A servo-hydraulic fatigue testing machine with a load capacity of 50KN was used (Figure 3.18). In order to avoid excessive machine times,

tests were terminated at $2\times10^6$ cycles in the absence of specimen failures ('run-outs'). For the purpose of mean stress consideration on the S-N curve, force-controlled fatigue tests were carried out on five specimens under a sinusoidal wave tension-tension cyclic loading (stress ratio of 0.1) at the frequency of 15 Hz by using a 30kN servo-hydraulic fatigue testing machine. The applied stress amplitude levels ranged between 198MPa and 230MPa. For these series of tests, run-outs were considered at $10^7$ cycles.

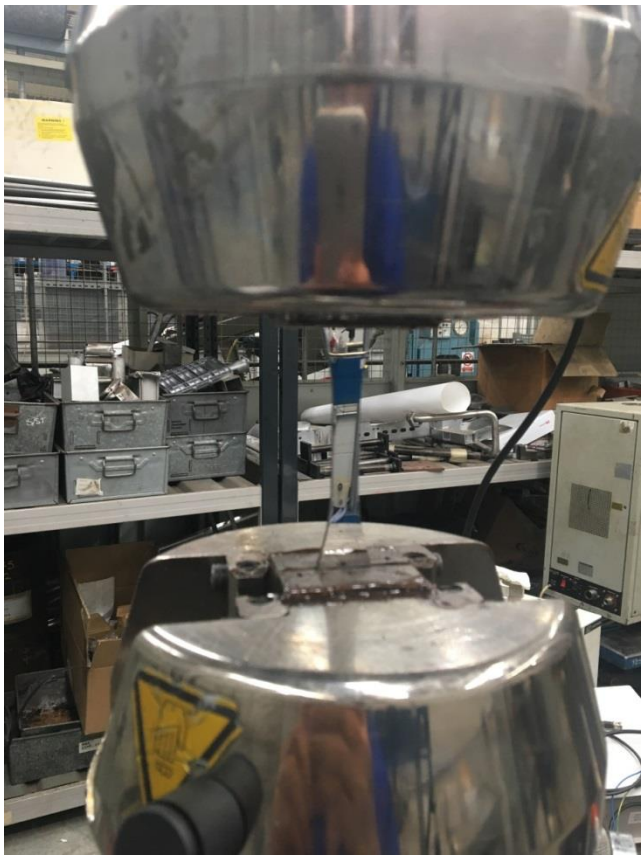

Figure 3.18. Test specimen assembled in a servo-hydraulic fatigue testing machine with a load capacity of 50KN.

Using the same test condition, fatigue tests were undertaken also on four pre-pitted specimens. A corrosion pit was created on the centre of each specimen, prior to starting the fatigue tests, by using the VersaScan electrochemical instrument and

standard methods explained above utilising galvanostatic polarisation with the constant current of 200µA. Table 3.3 shows the size of the pit on each specimen. All the fatigue tests were carried out in the air at ambient temperature (21°C). The fatigue test methods were performed in accordance with ASTM standard E468-11 and alignments conducted as based on ASTM E606 prior to starting the test.

Table 3.3: Pit geometries created on each fatigue tests specimen.

| Specimen Code | Pit depth, *a* (mm) | Pit width, 2c | Aspect Ratio, a/2c | |
|---|---|---|---|---|
| B01 | 0.0344 | 0.271 | 0.13 | 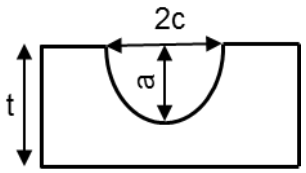 |
| B02 | 0.179 | 0.315 | 0.57 | |
| B03 | 0.0763 | 0.6 | 0.13 | |
| B04 | **0.**0851 | 0.676 | 0.13 | |
| B05 | 0.0674 | 0.608 | 0.11 | |



## 3.4 In-situ corrosion fatigue test apparatus

This section details the development of environmental apparatus to facilitate the environmental tests and visualise the initiation of a fatigue crack from a corrosion pit in X65 steel using X-ray CT. The test cell comprises five main elements, viz. the vessel body, vessel lids, locking rings, followers and grippers. A schematic of the cell is given in Figure 3.19. The vessel body was machined from a transparent cast acrylic (poly(methyl methacrylate); Perspex) tube. Similar designs for the basic vessel body have been reported by Williams *et al.*(Williams et al. 2011), Singh *et al.*(Singh et al. 2016) and Chapman *et al.* (Chapman et al. 2015). Perspex was selected as the most suitable material of construction on the grounds of chemical, mechanical and optical properties. Crucially, Perspex is resistant to chemical degradation in saline solutions containing dissolved $H_2S$ and has excellent X-ray transmission properties. This

material has been used as a material of construction for vessels used in X-ray scanners (Nadimi et al. 2017, Chapman et al. 2015, Cordes et al. 2015). The optical transparency of Perspex provides the same practical advantages as glass, including clear observation of the specimen in the test cell during set up of the location parameters and region of interest in the X-ray scanner, in addition to enabling visual inspection of the test solution in the vessel (i.e. level checks during solution transfer, indication of solution loss, changes in colour or clarity, etc). The anticipated mechanical loads placed on the vessel required minimum wall thickness values of around 5mm. However, additional considerations led to the decision to use a value of 10mm. Specifically, these factors included the need to provide further assurance that the test cell would not distort during specimen loading (i.e. under the compression load applied via the vertical bolts placed in the grippers, as the latter maintains the tensile load on the specimen). Increased wall thickness also reduced concerns regarding the modest creep strength of Perspex. Finally, the increase in dimension was necessary in order to provide an O-ring groove around the circumference.

The provision of robust sealing for the test cell was a vital consideration, due to the toxic nature of the $H_2S$ contained therein and the need to exclude oxygen from the test environment. The configuration employed in this work ensured that the contents of the cell were fully isolated from the external environment throughout testing using axially loaded small-scale tensile specimens. Sealing was achieved using two O-ring pairs. One pair of O-rings (14x1.5 VI75 type) are located around the specimen top and bottom, between the vessel lid and the elliptical follower, and reside inside the vessel lid groove. The second pair (75x2.5 VI75 type) sit in grooves located in the top and bottom of the vessel body and are placed between the vessel body and the vessel lid.

Prior to placement, O-rings were lubricated with a clear silicon grease to reduce interfacial friction. By placing all the followers, tightening screws and locking rings, the O-rings were held in place and sealing was ensured.

The top and bottom vessel lids were machined from PEEK (polyether ether ketone), a thermoplastic with excellent mechanical properties and chemical resistance to corrosive sour environments. Four ports were machined to allow for entry and exit of both test gas and solution. The lids were designed to allow for the rotation of the specimen and prevent the application of a torsional load to the test specimen when tightening the locking ring. The locking rings (see item 5 in Figure 3.19) were made of 316L grade stainless steel and threaded to provide smooth travel with the threads on each end of the vessel body.

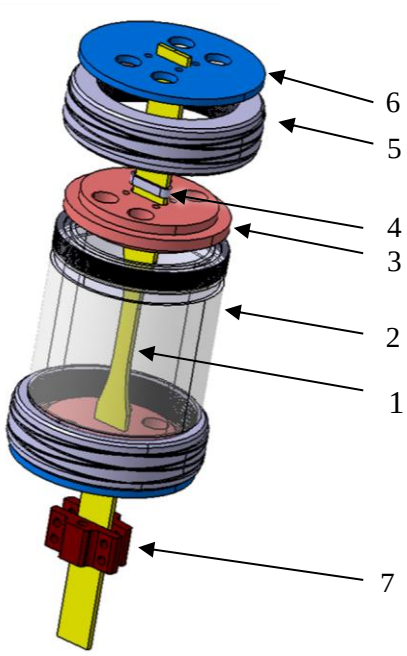


| Part number | Part name | Material |
|---|---|---|
| 1 | Specimen | X65 steel |
| 2 | Vessel body | Perspex |
| 3 | Vessel lid | PEEK |
| 4 | Elliptical follower | PEEK |
| 5 | Locking rings | 316 Stainless Steel |
| 6 | Compression plate | 316 Stainless Steel |
| 7 | Specimen grippers | 316 Stainless Steel |

Figure 3.19. An expanded isometric view of the in-situ corrosion-fatigue testing apparatus.

A notable benefit of the vessel load bearing design is that it allows data to be collected over the complete 360° scan (i.e. without the presence of artefacts or shadows in images) in the X-ray tomography instrument, due to the absence of load bearing side members on the vessel body. The ability to lock-off the test specimen under a static load is desirable in order to keep the crack open during X-ray scanning. This feature was considered especially important as it assists with monitoring a crack and reduces the risk of crack wedging and/or premature crack closure. To achieve this requirement, the grippers shown in Figure 3.19 and 3.20 were designed and built to be placed at the top and bottom of the specimen after interrupting the fatigue test and applying a static tensile load. Four horizontal bolts on the grippers maintain friction between the specimen and grippers faces. Two vertical bolts provide the means to apply a compressive load on top of the compression plate. This arrangement ensures that a similar tensile load is applied to the specimen during the X-ray inspection process.

The overall outer diameter of the vessel is 102mm, a value that was consistent with the maximum working distance between the detector and X-ray source for the XRadia instrument. The overall height of the vessel was chosen to be 130mm to accommodate the specimen dimensional requirements stated in ASTM E466. The vessel size provided sufficient clearance in the X-ray scanner to allow for fittings on the top and bottom of the vessel. Figure 3.20 shows the vessel placed inside the fatigue test machine. The gas/solution inlets and outlets are also shown.

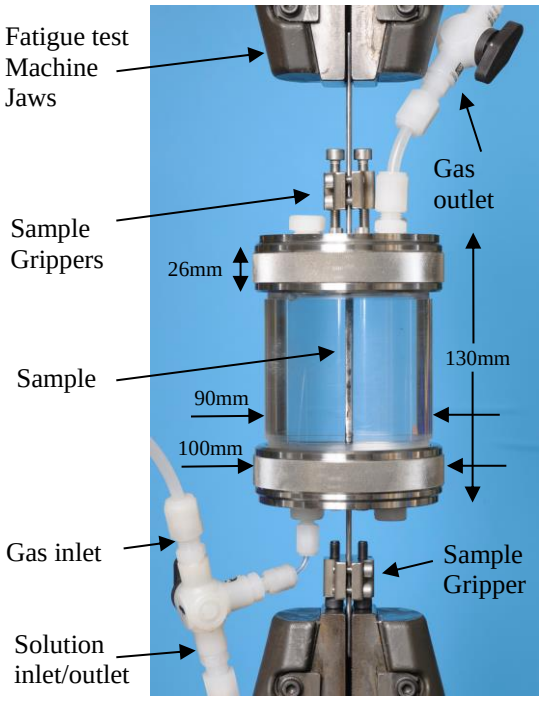


(a)

Figure 3.20. The corrosion fatigue test apparatus mounted in the fatigue test machine showing the inlets and outlets of gas and solution and key dimensions.

## 3.5 Fatigue tests in the sour environment on smooth and pre-pitted specimens

All experiments were carried out on specimens extracted longitudinally from parent material from X65 steel pipe. Two types of fatigue specimens were used during environmental tests, viz. smooth (Figure 3.21a) and pre-pitted (Figure 3.21b), both of which were designed in accordance with ASTM E466. Initial trials indicated that in order to decrease the computed tomography artifacts on X-ray images and optimise the resolution, it was necessary to reduce the width of the pre-pitted specimens from 10mm to 3mm (Figure 3.21b). In order to make a smooth contact between the O-rings and the specimen, a curved edge was used on all specimens. Figure 3.21c shows the size of the fillet that was machined on the edge of all test specimens. All test

specimens were ground to a 4000 carbon-silica paper finish prior to a final polish using a 3μm cloth. A corrosion pit of the desired dimensions was created in the centre of the test section of the specimen by using the electrochemical cell utilising the potentiostatic method and potential of 1.0V (see Section 3.2). The pit-to-fatigue crack transition was investigated by monitoring the pre-pitted specimen during the *in-situ* corrosion fatigue test using X-ray micro-tomography.

An initial corrosion fatigue test was performed using the smooth test specimen to both check the performance of the apparatus and also obtain an estimate of the number of cycles to failure in a corrosive environment and thus plan the scanning intervals (i.e. determine the appropriate number of cycles to run in each case before interrupting the test, locking off the specimen under load, and performing periodic X-ray tomography scans). The specimens were tested under the constant amplitude loading condition and sinusoidal waveform in the high cycle fatigue regime. The applied stress ratio (R) was held constant at 0.1 for all tests. The applied stress amplitude was varied from 135 to 209 MPa (corresponding maximum stress was varied from 300 to 464 MPa) for ten smooth specimens each possessing cross-sectional area of 3x10 $mm^2$ (see Figure 3.21a). Fourteen pre-pitted specimens of cross-sectional area 3x3 $mm^2$ (Figure 3.21b) were tested at two different stress amplitude of 165 and 185 MPa, with the corresponding maximum stress values of respectively 367 MPa (70% YS) and 413 MPa (80% YS). To investigate the pit-to-crack transition and its evolution, fatigue tests for three different pre-pitted specimens were interrupted at different intervals during the fatigue cycle. Table 3.4 and 3.5 show the size of corrosion pits on the specimens for uninterrupted (eleven specimens) and interrupted (three specimens) corrosion fatigue tests respectively. A frequency of 0.3Hz was applied in order to

allow the corrosive environment to interact with the specimen. Testing was conducted at ambient pressure and temperature. The test environment comprised 3.5% w/v NaCl solution saturated with a gas mixture containing 12.5% $H_2S$ in $CO_2$ balance.

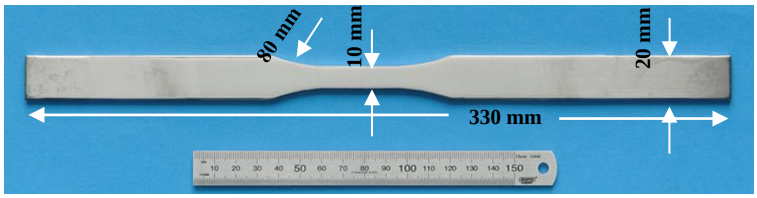


(a)

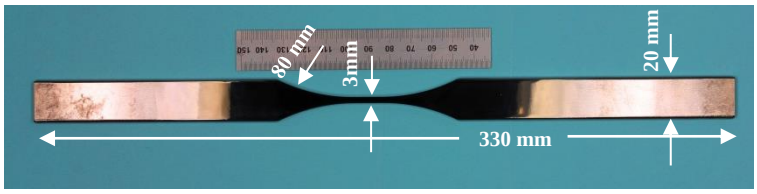


(b)

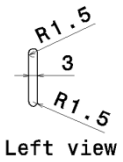


(c)

Figure 3.21. (a) Smooth corrosion fatigue test specimen, (b) Pre-pitted corrosion fatigue test specimen, (c) side view of specimens showing the size of the fillet.

Table 3.4: The corrosion pit size for specimens from uninterrupted corrosion fatigue tests.

| Specimen Code | Pit depth, *a* (mm) | Pit width, 2c | Aspect Ratio, a/2c |
|---|---|---|---|
| F01 | 173.59 | 519.7 | 0.33 |
| F02 | 154.12 | 533.48 | 0.29 |
| F03 | 288.67 | 641.64 | 0.45 |
| F04 | 231.18 | 580 | 0.40 |
| F05 | 245.2 | 597 | 0.41 |
| F06 | 302.5 | 700 | 0.43 |
| F07 | 312.11 | 590 | 0.53 |
| F08 | 307.53 | 584.2 | 0.53 |
| F09 | 271.1 | 511.9 | 0.53 |
| F10 | 166.76 | 502.64 | 0.33 |
| F11 | 172.6 | 486.58 | 0.35 |

Table 3.5: The corrosion pit size of specimens for interrupted corrosion fatigue tests.

| Specimen Code | Depth, *a* (mm) | Pit width, 2c | Aspect Ratio, a/2c |
|---|---|---|---|
| E01 | 160.028 | 546.54 | 0.29 |
| E02 | 168 | 537 | 0.31 |
| E03 | 303.98 | 671 | 0.45 |

The sour corrosion fatigue tests were performed in the Gooch laboratory at TWI Ltd. in Cambridge, which has fixed $H_2S$ sensors for monitoring and suitable extraction and safety procedures in place. A full risk assessment was carried out with the relevant staff prior to experimental work. Prior to starting the test, 3.5% NaCl solution was deaerated by purging with high-purity nitrogen for 24 hrs in a sealed High-Density Polyethylene (HDPE) barrel. Previous work at TWI Ltd. has shown that this process reduces the measured dissolved oxygen content to below 10 ppb. For each test, once the apparatus and specimen were assembled and placed in the fatigue loading machine, a leak test was carried out by pressurising the test cell with nitrogen to 0.5 barg to ensure that the seals did not leak. Following confirmation of seal integrity, the test cell was deaerated using a fast purge of nitrogen for 1hr, then charged with 3.5% NaCl solution, and then purged once again with nitrogen for approximately one hour. Upon completion of this process, the test solution in the cell was saturated with sour test gas (i.e. containing 12.5% $H_2S$) using a fast purge for 1 hr. Finally, fatigue load was applied to the specimen with the frequency of 0.3Hz and stress ratio of 0.1. The vessel contains about 380 $cm^3$ of the solution. Figure 3.22 shows the experimental setup.

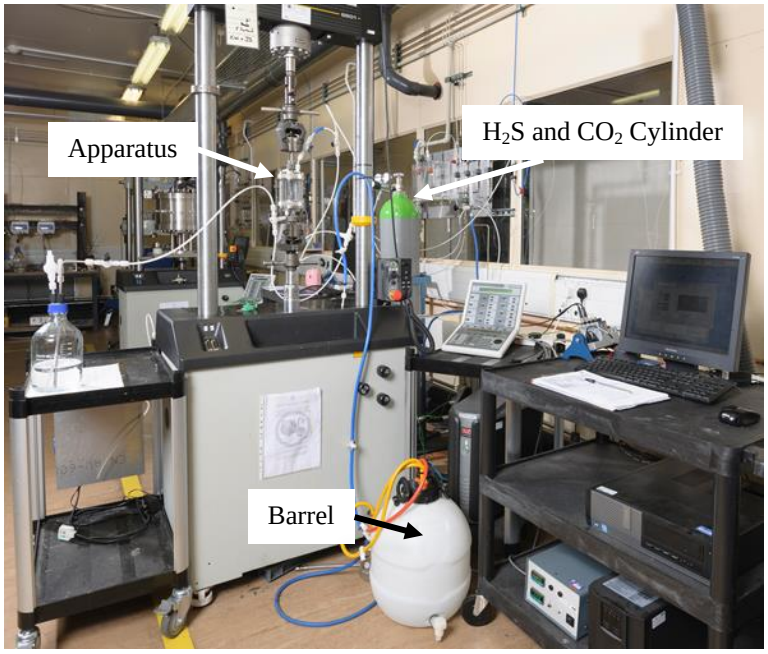


Figure 3.22. Experimental set up of corrosion-fatigue test.

To investigate the pit-to-crack transition and its evolution, the fatigue test of three pre-pitted specimen were interrupted at different points in the test cycle. At each interval, the cell contents were drained and the cell filled with nitrogen to minimise the risk of air ingress in the test cell and oxidation of the specimen including crack surfaces. The presence of residual moisture, retained in the cell following draining (ca.50ml of 3.5%NaCl solution saturated with nitrogen), was anticipated to ensure that the specimen and in particular exposed crack surfaces remained wetted during X-ray scans. A tensile stress of magnitude equivalent to half the value of the maximum cyclic stress was applied to the test specimen. This stress was maintained by tightening the grippers on the top and bottom of the specimen. Once secured, the cell was released from the fatigue test machine and put on the bespoke base and placed in the X-ray micro-tomography instrument (Figure 3.23). The stress applied during

scanning was well below the yield strength of the material (516 MPa), but still sufficient to hold the crack open in order to assist with imaging the crack.

Following each X-ray scan (a period of around13 hrs) the fatigue test was resumed promptly. The aforementioned sequence was repeated until the specimen failed. No leaks of toxic $H_2S$ (as detected by personal or fixed laboratory sensors and alarms) were recorded during any tests and no evidence for air ingress (e.g. formation of elemental sulphur) was noted. Due to the formation of electrically conducting corrosion product (i.e. iron sulphide), the use of direct current potential drop (DCPD) or alternating current potential drop (ACPD) for monitoring of crack initiation was not considered in this study.

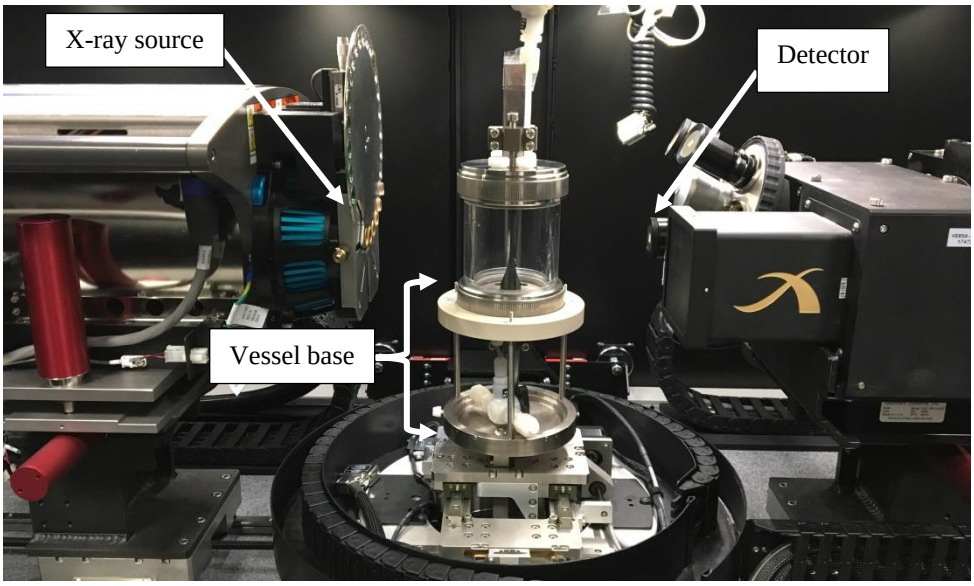


Figure 3.23. Test vessel inside X-ray scanner.

# Chapter 4: Life predictions and modelling

## 4.1 Predication approaches

### 4.1.1 Stress based approach

In 1860s, Wohler proposed the stress-life approach to predict the total fatigue life. The concept of a fatigue endurance limit was then evolved from his work. The approach is empirical and mainly used in fatigue analysis of components exposed to low stress amplitude values and long fatigue life, i.e. the high cycle fatigue (HCF) regime. The stress-life (S-N) curve is generally obtained by testing the standard fatigue test specimens under tension-compression, tension-tension, plane bending or rotating bending load (Suresh 1998). ASTM E466-468 (American Society for Testing and Materials) outlines the testing method for undertaking force controlled fatigue tests and acquiring S-N curves using smooth specimens. Basquin in 1910 proposed a relationship between stress amplitude and number of reversals to failure in a fully reversed, constant amplitude fatigue test that is known as Basquin equation (Stephens, R. I. et al. 2000):

$$\frac{\Delta\sigma}{2} = \sigma'_f (2N_f)^b \tag{4.1}$$

### 4.1.2 Strain based approach

The strain based approach was first introduced by Coffin and Monson (working independently) in 1954. This approach is employed to predict the fatigue life when considerable plastic strain occurs, due to high levels of applied stress and/or the presence of stress concentrators in the components that lead to reduced fatigue life, i.e.

the low cycle fatigue (LCF) (Suresh 1998). Coffin and Monson found a linear relationship between plastic strain amplitude, $\frac{\Delta\varepsilon_p}{2}$, and the number of load reversals to failure, $2N_f$, which can be written as:

$$\frac{\Delta\varepsilon_p}{2} = \varepsilon'_f (2N_f)^c \tag{4.2}$$

In which fatigue ductility coefficient, $\varepsilon'_f$, and fatigue ductility exponent, $c$, are material parameter obtained from cyclic strain-life curve. Combining the Basquin equation (Eq. 4.1) and Coffin-Mansion equation, the total strain amplitude can be written as (Stephens, R. I. et al. 2000):

$$\frac{\Delta\varepsilon}{2} = \frac{\Delta\varepsilon_e}{2} + \frac{\Delta\varepsilon_p}{2} = \frac{\sigma'_f}{E}(2N_f)^b + \varepsilon'_f (2N_f)^c \tag{4.3}$$

ASTM E606 includes the test methodology for strain controlled fatigue testing and the acquisition of the strain-life curves using smooth specimens.

Both the stress-based and the strain-based approaches correlate the total number of cycles for fatigue crack initiation and propagation till the final failure (Suresh 1998).

## 4.2 Notch effect

Flaws that are present in engineering structures are typically areas of localised stress concentration. As a result, the presence of flaws modifies the stress and strain fields in the structure and consequently become the likely locations for fatigue initiation. The effect of these notches on stress concentration is well understood and characterised through the theoretical elastic stress concentration factor, $K_t$, which is the ratio of local maximum stress to applied stress. Only the geometry and loading mode affect this

factor. In the case of cyclic loading, $K_t$ is substituted by an experimental or empirical parameter called $K_f$, the fatigue notch factor, defined by the ratio of unnotched specimen fatigue limit to the notched specimen fatigue limit. Generally, $K_f$ has a lower value than $K_t$ that is characterized by the notch sensitivity index, $q$:

$$q = \frac{K_f - 1}{K_t - 1} \tag{4.4}$$

The localised stress and strain can be predicted by Finite Element Analysis (FEA) or well-known semi-analytical models. The following sections introduce the two aforementioned approaches that are also used in the present study.

### 4.2.1 Finite Element Analysis (FEA)

In this study, 3D FEA has been conducted by employing ABAQUS to evaluate the stress and strain around single corrosion pits (i.e. a pit assumed to be a notch) possessing a range of different geometries. The stress and strain distribution around a pit in API 5L-X65 steel specimen was analysed using an elastic-plastic material model and applying a static or cyclic load.

#### *4.2.1.1 Static analysis*

For static analysis, a 3D plate specimen with a constant length ($L$), width ($W$) and plate thickness ($t$) was considered. Plate length and width were held at the same value ($L$=$W$), which was notably greater (20x) than the value for the plate thickness (Figure 4.1). A hemispherical or semi-elliptical pit of desired size was generated in the middle of the plate (Table 4.1). The dimensions of plate were held constant in all cases. The applied static tensile stress was 80% of the material yield strength (YS), equivalent to

that to be used in subsequent empirical work. Data for the 10%YS and 50%YS cases were also collected using the model. To reduce the calculation time, only one-quarter of the plate was simulated in ABAQUS, thus in the cutting surfaces of plate symmetry, boundary conditions were applied. An elastic-plastic material model was used to account for the effect of plastic deformation in the vicinity of a pit. The true stress-strain curve of X65 steels (Figure 3.1) was used as input in ABAQUS, with values of modulus of elasticity and Poisson's ratio of 211.33 GPa and 0.3, respectively. For numerical analysis, use of uniform geometric elements is important in order to minimise 'shape effects' in results. Consequently, in this work, the model has been meshed by using the 10-node tetrahedral (C3D10) element. To enhance the accuracy of stress and strain calculations, a finer mesh was used around the stress concentration location. As uniformity in the size of elements may affect the results, the mesh density around the pit was changed when the pit dimensions were altered. This procedure provides a similar level of accuracy, although the mesh created in each model is not identical. A mesh convergence study was conducted to provide assurance for the accuracy of the mesh. Consequently, it was ensured that the maximum stress and strain in the pit region were convergent and not dependent on mesh size. Figure 4.2 shows the finite element model of one-quarter of the test plate, utilised mesh, plane of applied load and planes of symmetry. The load plan is outlined in red and is perpendicular to the x-axis. The symmetry planes are marked with red and blue triangles on the edges. In order to provide a better indication of the model validity, the results for semi-elliptical pit were compared with a semi-analytical method (Neuber's rule) as explained in Section 4.2.2.

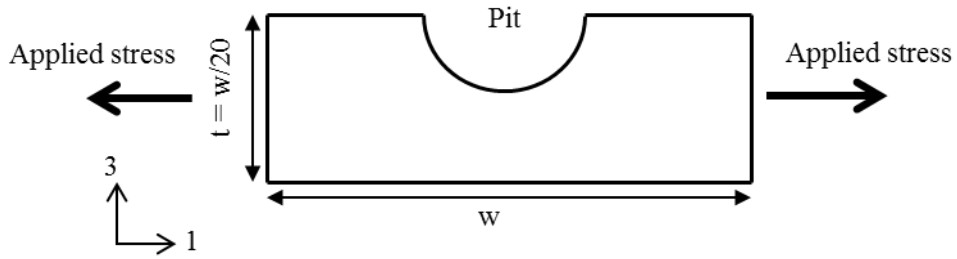


Figure 4.1. Cross-sectional geometry of plate containing a pit.

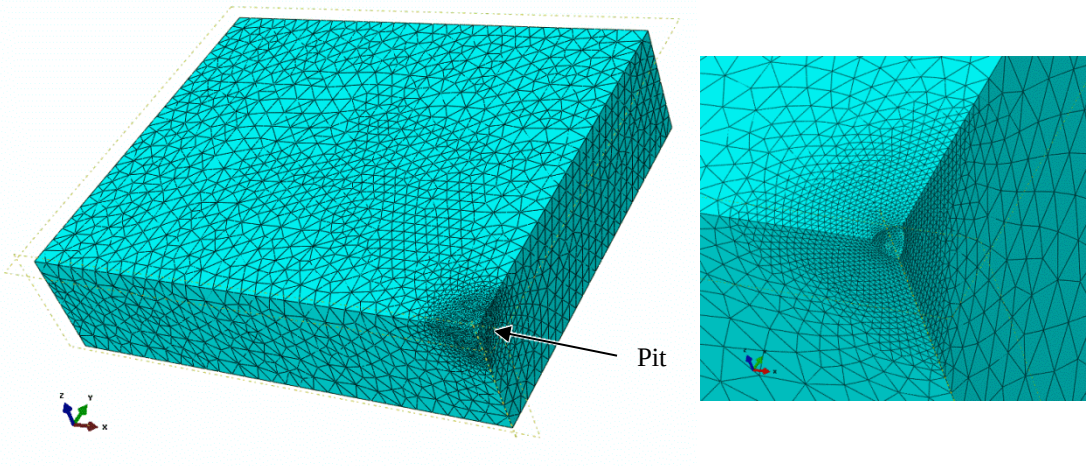


(a) (b)

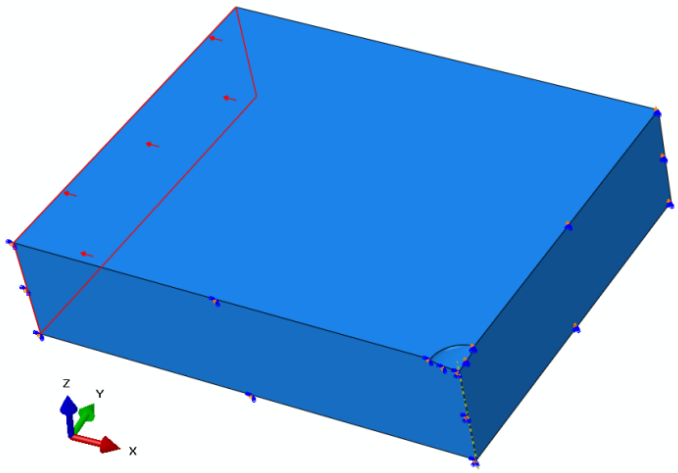


(c)

Figure 4.2. (a) Finite element model of 1/4 plate containing a pit, showing mesh (b) Local mesh around the pit. (c) Defined planes of symmetry boundary condition and applied load.

Table 4.1: Geometry of the simulated corrosion pits and parameters used in model.

| Pit shape | Hemispherical pit 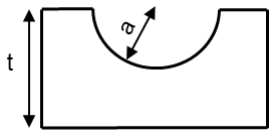  | Semi-elliptical pit 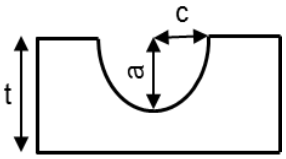  |
|---|---|---|
| Geometric variables used in model | *t* = const. ; *a*/*t*= 0.01, 0.06, 0.1, 0.2, 0.3, 0.5 | *t*, *c* = const. ; *a*/*t*= 0.02, 0.06, 0.08, 0.1, 0.14, 0.2, 0.25, 0.3, 0.5 |

#### *4.2.1.2 Fatigue analysis*

Recently, there has been increasing interest in use of FEA for evaluation of stress and strain in corrosion pits that are mentioned in Section 2.3.2. However, it is important to note that these studies have been restricted to elastic material models and static loading. This is a significant limitation, particularly in the context of fatigue damage, due to the important effect of cyclic loading and plastic deformation around the pit on crack initiation (as described in chapter 2), Consideration of the above provides motivation for the present study where 3D elastic-plastic FEA has been conducted, using ABAQUS software, to investigate the local stress and strain behaviour at the pit under fatigue loading.

Details of the routine are summarised as follows. A specimen was modelled using a plate of thickness and length values of 3mm and 10mm respectively. A semi-elliptical pit of desired geometry was created in the middle of the plate, as represented in Table 4.2. Importantly, pit sizes were selected on the basis of real in-service data provided

by the industrial sponsor (i.e. data collected using Non Destructive Testing (NDT) methods on steel production risers). To decrease the calculation time, only one-quarter of this plate was analysed under symmetry boundary conditions. A sinusoidal cyclic load was applied for ten cycles at a stress ratio of 0.1 and amplitude stress values of 90MPa, 146MPa, 169MPa with the corresponding maximum stresses of 200MPa, 325MPa, 375MPa respectively (noting that these values are less than X65 steel cyclic yield strength of 420MPa). The combined Isotropic-Kinematic hardening elastic-plastic material model was utilised, incorporating data from the cyclic true stress-strain curve of X65 steel reported in the literature (Fatoba and Akid, Robert 2014) (Figure 3.2).

Table 4.2: Simulated pit geometries.

| Number | Depth, *a* (mm) | Aspect Ratio, a/2c | Depth/Specimen thickness, a/t | |
|---|---|---|---|---|
| 1 | 0.15 | 0.1 | 0.05 | 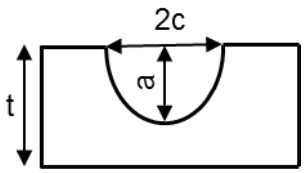  |
| 2 | 0.15 | 0.3 | 0.05 | |
| 3 | 0.15 | 0.54 | 0.05 | |
| 4 | 0.3 | 0.9 | 0.1 | |
| 5 | 0.45 | 1.3 | 0.15 | |

### 4.2.2 Semi analytical

There is a framework of analytical methods, which were very popular in the 1970s and 1980s when the computing power was low. Even with today's available computation resource, these analytical methods are still a useful complement to FEA as the former offers quicker analysis and are also useful for parametric studies. Neuber developed a model to include the contribution of plastic strain in evaluating the notch stress and strain (Neuber 1961). Glinka has also improved the calculation methods of the notch root strain by taking account of plastic yielding around the notch root

(Glinka 1985). In this study, the pit maximum stress and strain under static load were evaluated using the Neuber's rule (Eq. 4.5 and 4.6) (Stephens, R. I. et al. 2000) and compared with the FE results. The value for $K_t$ in equation 4.5 is calculated using equation 4.7 (Ahn et al. 1992), where $K$ is strength coefficient equal to 713 MPa and $n$ is strain hardening exponent equal to 0.06 taken from the engineering stress-strain curve in Figure 3.1.

$$\sigma_{\max}.\varepsilon_{\max} = \frac{(K_t.\sigma_{applied})^2}{E} \tag{4.5}$$

$$\varepsilon_{\max} = \frac{\sigma_{\max}}{E} + (\frac{\sigma_{\max}}{K})^{(1/n)} \tag{4.6}$$

$$K_t = 1 + 1.25\sqrt{\frac{2}{1+(\frac{c}{a})^2}} \tag{4.7}$$

For fatigue simulations, the local stress and strain ranges at corrosion pits were calculated by simultaneously solving the material's cyclic stress-strain relationship (Eq. 4.8) with either the Neuber's (Eq. 4.9) (Stephens, R. I. et al. 2000, Neuber 1961) or Glinka's rule (Eq. 4.10) (Glinka 1985, Stephens, R. I. et al. 2000). The required cyclic and monotonic mechanical properties in these equations, i.e. $E, n'$ and $K'$, were taken from Table 3.2. The required stress concentration factor, $K_t$ in Eq. 4.10, and fatigue notch factor, $K_f$ in Eq. 4.9, were calculated using equations 4.7 and 4.11, where $r$ was found by Eq. 4.12 (Ahn et al. 1992). The parameter $a'$ in Eq. 4.11 is a material constant (Ahn et al. 1992) that in this study equals to 0.226 mm (Ahn et al. 1992). The results were compared with FEA results. It should be noted that advanced computational techniques such as elastic-plastic FEA can be a more powerful notch stress/ strain monitoring method (Zeng and Fatemi, A 2001).

$$\Delta\varepsilon = \frac{\Delta\sigma}{E} + 2\left(\frac{\Delta\sigma}{2K'}\right)^{(1/n')} \tag{4.8}$$

$$\Delta\varepsilon.\Delta\sigma = \frac{(K_f.\Delta S)^2}{E} \tag{4.9}$$

$$\frac{\Delta\sigma^2}{E} + \frac{4\Delta\sigma}{n'+1}\left(\frac{\Delta\sigma}{2K'}\right)^{(1/n')} = \frac{(K_t.\Delta S)^2}{E} \tag{4.10}$$

$$K_f = 1 + \frac{K_t - 1}{1 + \frac{a'}{\mathrm{r}}} \tag{4.11}$$

$$\mathrm{r} = \frac{\mathrm{a}}{2}\left(1 + \left(\frac{\mathrm{c}}{\mathrm{a}}\right)^2\right) \tag{4.12}$$

The SWT equation (Smith et al. 1970) has been successfully applied to predict the crack initiation life (Htoo et al. 2016). The advantage of this model is that it allows consideration of the effect of mean stress on fatigue life. In the present study, following determination of the local stress and strain values by finite element simulations, the Smith-Watson-Topper equation (Eq. 4.13) (Stephens, R. I. et al. 2000, Smith et al. 1970) and the cyclic mechanical behaviour of X65 steel were utilised to predict fatigue life to the formation of a small crack under cyclic loading, i.e. $N_i$. In other words, the maximum stress at the pit and local strain range were taken from the FEA output and then inputted in equation 4.13 along with the material mechanical properties from Table 3.2. A MATLAB code was written to solve equations 4.8 to 4.13. In the SWT equation, mean stress effect is accounted for by the maximum stress term as shown in Eq. (4.13).

$$\varepsilon_a\sigma_{\max} = (\sigma'_f)^2\frac{(2N_i)^{2b}}{E} + \varepsilon'_f\sigma'_f(2N_i)^{b+C} \tag{4.13}$$

# Chapter 5: Results and discussions

This Section includes fatigue tests in ambient air and in sour environment on both smooth and pre-pitted specimens, numerical and analytical models to study the fatigue behaviour of corrosion pits and a life prediction model for corrosion pit-to-fatigue crack transition. The test condition, sample schematic and stress amplitude level are summarised in Appendix A.

## 5.1 Empirical fatigue testing

### 5.1.1 Smooth specimens (ambient air)

The stress-life curve (S-N curve) is generally adopted for high cycle fatigue regions. The relationship between the applied stress amplitude and the number of cycles to failure (S-N) at a stress ratio of -1 was obtained by substituting the cyclic load mechanical properties of API-5L X65 steel ($\sigma'_f$, fatigue strength coefficient and $b$, fatigue strength exponent) from Table 3.2 into equation 5.1 (Stephens, R. I. et al. 2000). At a stress ratio of 0.1, this relationship was also estimated by using the Gerber equation (Eq. 5.2) and equation 5.1. The Gerber equation (Stephens, R. I. et al. 2000) is one of the widely used empirical relations in fatigue analysis and takes account of the mean stress effect, which is expressed in terms of the stress ration (or R ratio) in the S-N data. Experimental results shown in Figure 5.1 indicate good correlation with the values determined using the approach outlined above.

$$\frac{\Delta\sigma}{2} = \sigma_a = \sigma'_f (2N_f)^b \tag{5.1}$$

$$\frac{\sigma_a}{\sigma_e} + \left(\frac{\sigma_m}{\sigma_{UTS}}\right)^2 = 1 \tag{5.2}$$

There is a lack of published data on the cyclic mechanical behaviour of X65 steel pipeline material, therefore in order to assess the relationship between applied stress amplitude and the number of cycles to failure (S-N curve), load controlled fatigue tests were carried out on X65 steel specimens. Figure 5.1 shows that the results of experiments are close to the estimated S-N curve in both tested stress ratios (for a given life, the difference (or scatter) in stress amplitude lies in the range 0-11%), therefore the estimated S-N curve is representative of X65 steel used in this present study and is valid for use in future Sections.

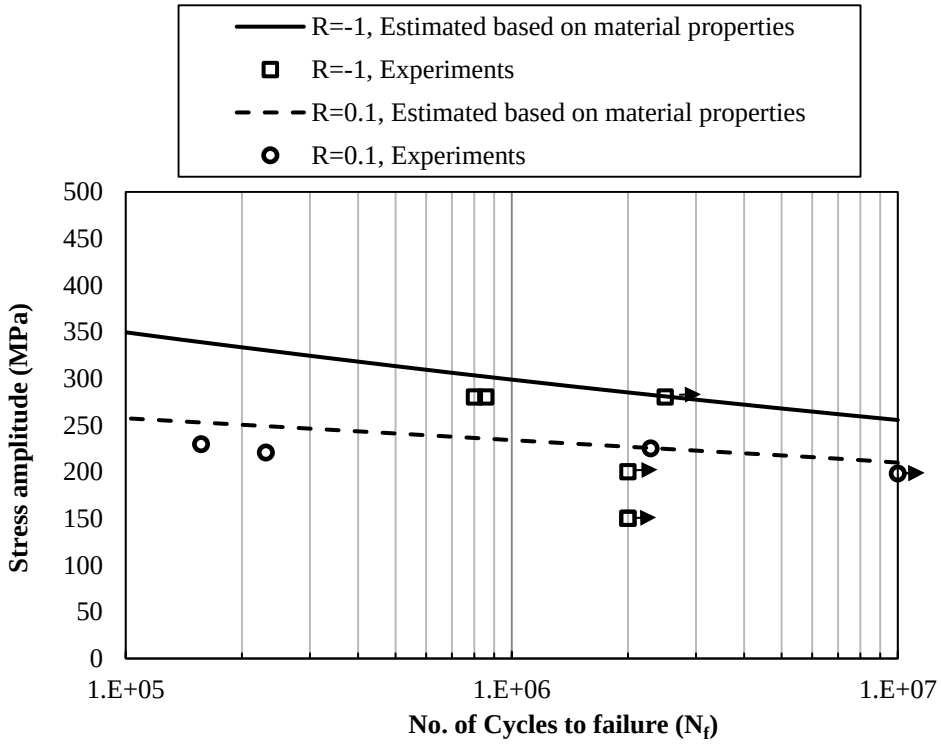


Figure 5.1. Stress-life (S-N) curve for X65 steel tested in R= -1 and R= 0.1. Arrows indicate run-out tests.

### 5.1.2 Pre-pitted specimens (ambient air)

Using the same test conditions as described in Section 5.1.1, fatigue tests were also undertaken on five pre-pitted specimens. The pit sizes and specimen geometry are reported in Section 3.3. Table 5.1 shows the value of applied stress amplitude and the number of cycles to failure for each specimen. It should be noted that due to the limited thickness of the specimens *i.e.* 3mm, the number of cycles to crack initiation can be considered to be comparable to the number of cycles to failure.

Table 5.1: The number of cycles to failure for pre-pitted specimens at $R$=0.1.

| Specimen code | Pit depth, $a$ (mm) | Aspect Ratio, a/2c | Stress Amplitude (MPa) | $N_f$ |
|---|---|---|---|---|
| B01 | 0.0344 | 0.13 | 225 | 377,358 |
| B02 | 0.179 | 0.57 | 225 | 120,295 |
| B03 | 0.0763 | 0.13 | 225 | 292,691 |
| B04 | **0.**0851 | 0.13 | 225 | 210,077 |
| B05 | 0.0674 | 0.11 | 230 | 455,758 |

Following specimen failure, fractographic analysis was undertaken using SEM. Prior to microscopy, specimens were cleaned by ultrasonication in DI water and Pyrene to remove surface contamination. Figure 5.2 provides a low magnification overview of the main surface features observed for all fractured specimens. In all case, cracking originated at the corrosion pit and subsequently propagated across the fatigue zone. The absence of progression marks (beach marks) in this zone demonstrates that there was no variation in the applied stress during tests and consequently constant crack growth rate followed. Variation in the stress level would be anticipated to lead to variation in crack growth rates and development of progression marks on the fracture surface (Sachs 2005). In the fatigue zone, striation marks representing a single stress cycle are visible at very high magnifications (Figure 5.3). The plane of the fatigue zone developed perpendicular to the plane of maximum load. Finally, cracks develop and grow to a point where brittle fracture can occur in the overload zone resulting in rapid crack propagation. Another surface feature that is commonly found in fatigue failures is ratchet marks, which represent the coalescence boundary between two adjacent cracks initiated on different geometric planes. An example of ratchet marks between two crack initiation sites is given in Figure 5.4 (Sachs 2005). In Figure 5.5, ratchet marks and crack origins are indicated for specimen B01. SEM images recorded for specimens B01, B02, B03, B04 and B05 revealed that crack nucleation occurred

near the mouth, at the walls and at the bottom of pits. X-ray image analysis and plan view inspection of fractured specimens showed that there were no other cracks initiated from the pit in other planes except the fractured plane (Figure 5.6). It should be noticed that the pits in specimen B01 to B04 were very shallow with an aspect ratio of about 0.12.

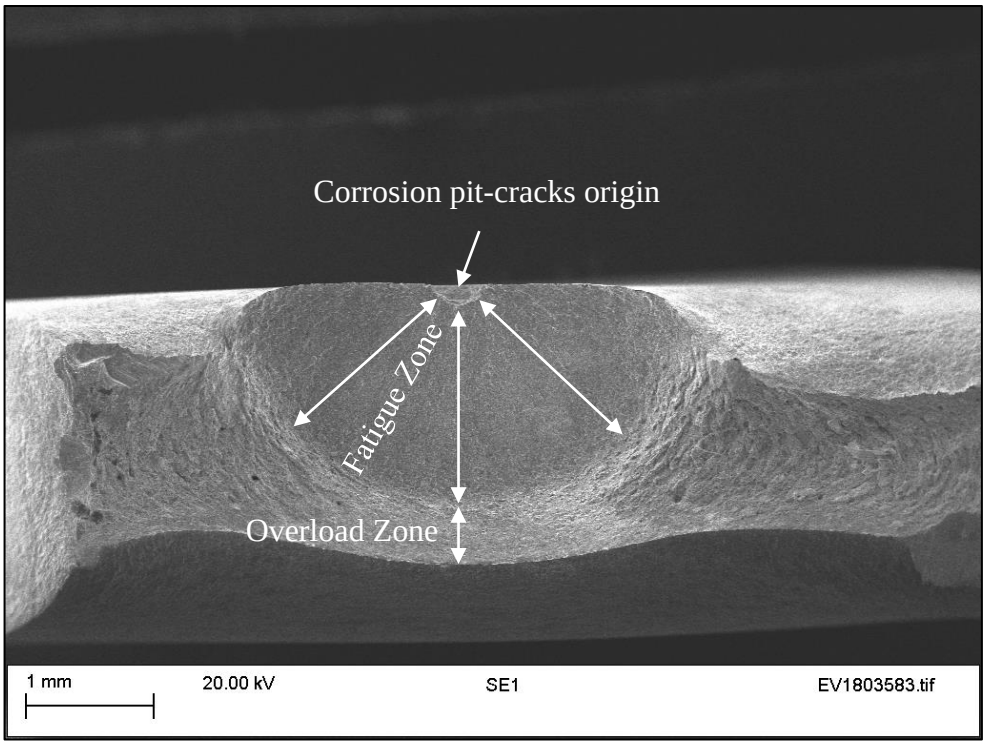


Figure 5.2. SEM image of a fractured specimen surface showing the overall surface morphology and features observed on all the fractured specimens.

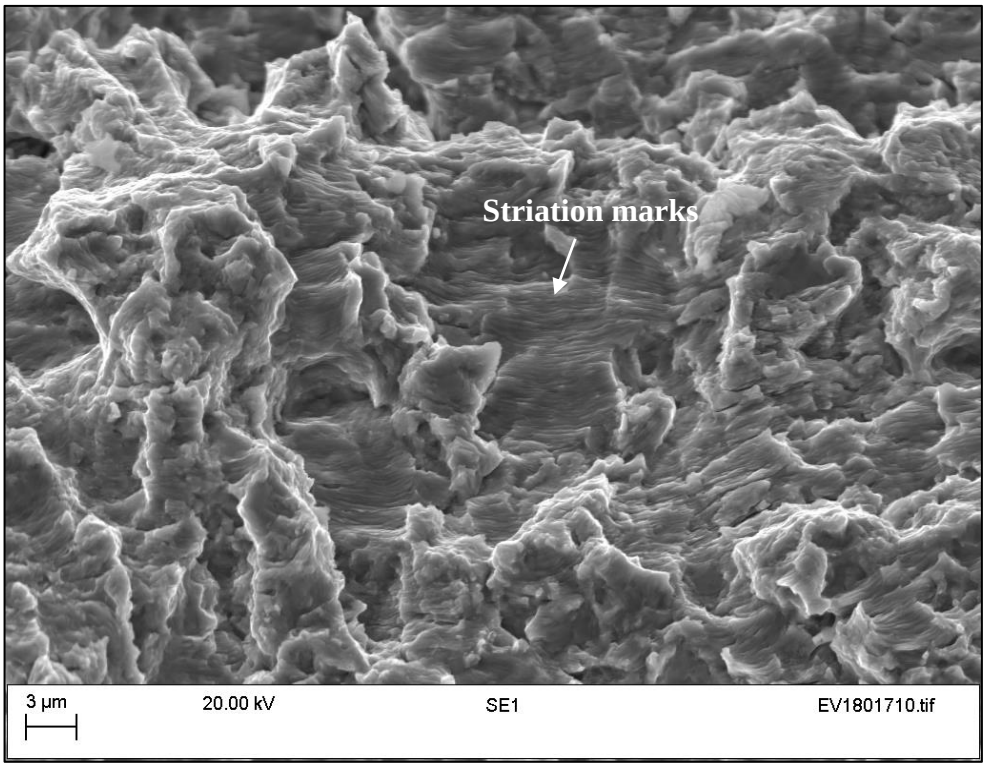


Figure 5.3. SEM image showing the striation marks observed on the specimens after fatigue failure (ambient air condition).

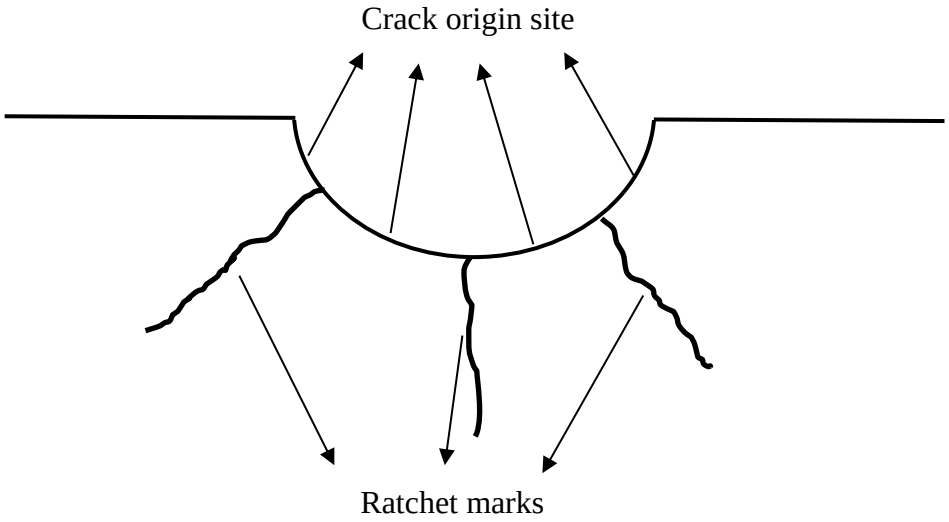


Figure 5.4. Ratchet marks and crack initiation sites, after (Sachs 2005).

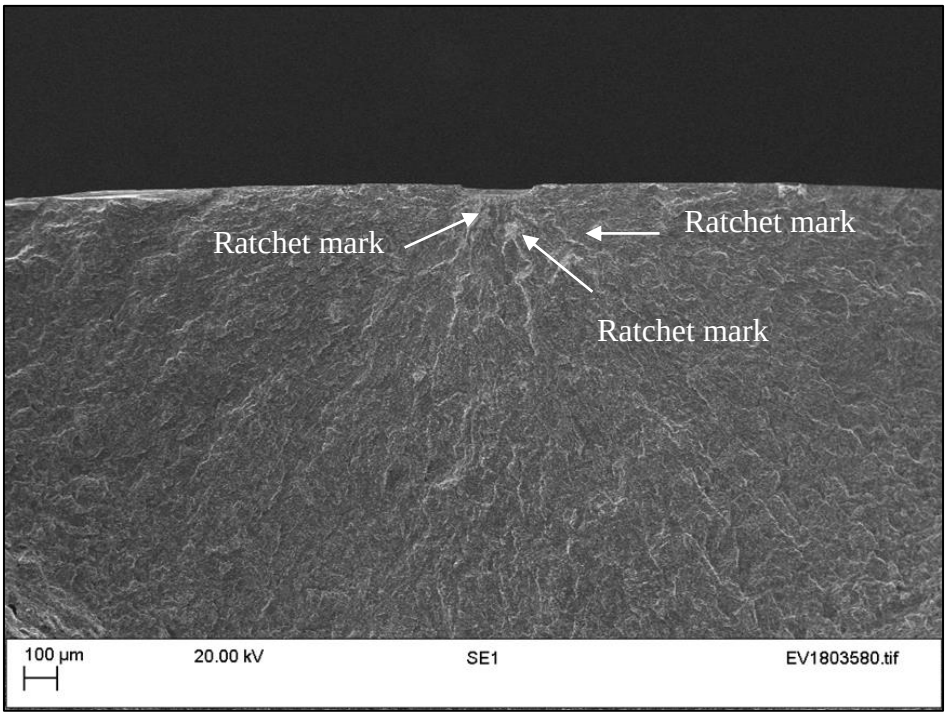


(a)

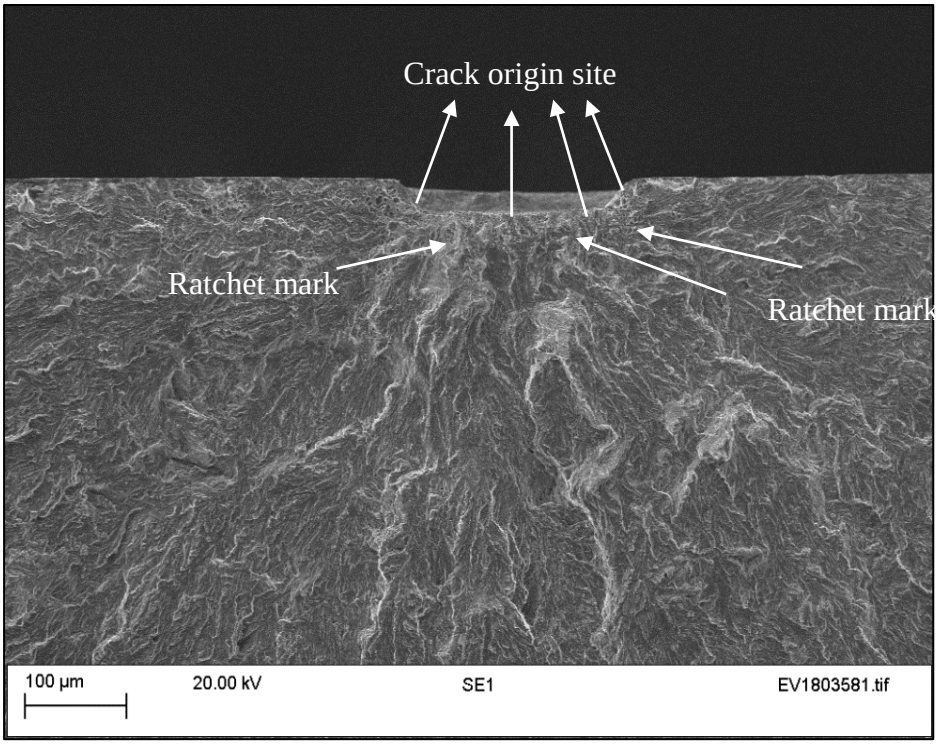


(b)

Figure 5.5. (a) Ratchet marks and crack origins for specimen B01. (b) Close-up view.

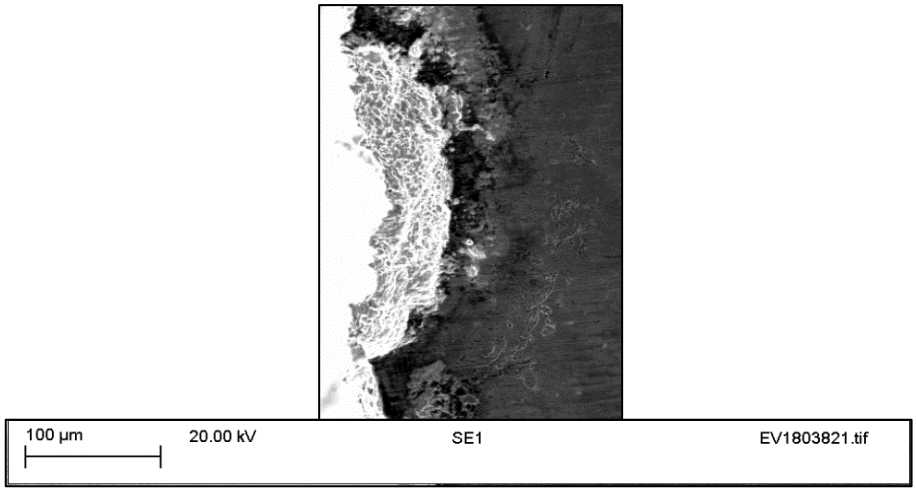


Figure 5.6. SEM image from the top view of B01 specimen.

### 5.1.3 Smooth specimens (sour environment)

Using the test protocol explained in Section 3.4 and the specimens shown in Section 3.5, *in-situ* corrosion fatigue tests were carried out on ten smooth specimens to obtain the S-N data in the sour environment. Test results are plotted in Figure 5.7 and it can be seen that in the sour environment, a significant reduction in fatigue strength is apparent for all stress levels investigated in comparison to the corresponding fatigue strength in air. The test measured S-N curve from the smooth specimens was used for the life prediction of pre-pitted specimens reported in later Sections. Comparison of the best-fitted S-N curve with the one obtained in the air condition indicates that the fatigue strength reduction was more significant at lower stress amplitudes. This finding is consistent with literature studies in this area where a corrosive environment was shown to reduce the fatigue life more significantly at lower stress amplitudes (Chlistovsky et al. 2007, Goto and Nisitani 1992). This happens because at lower

stress amplitude the environment has more time to affect the material and consequently weaken the material strengths.

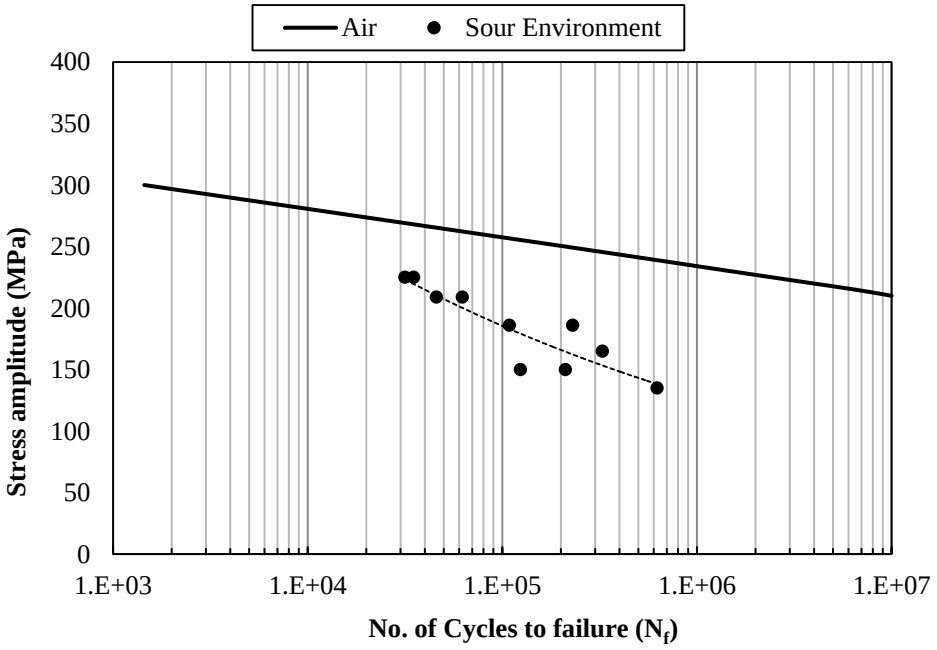


Figure 5.7. Stress-life (S-N) curve for X65 steel used in R= 0.1 in the air and sour environment.

### 5.1.4 Pre-pitted specimens (sour environment)

Sour corrosion fatigue tests were performed on specimens described in Tables 3.4 and 3.5, using the procedure outlined in Section 3.4, at two different stress amplitude levels, *i.e.* 165 MPa and 185 MPa and maximum stress values of 367 MPa (70% YS) and 413 MPa (80% YS), respectively. Figure 5.8 shows the plot of aspect ratio vs. the number of cycles to crack initiation. As mentioned previously (Section 5.1.2), due to the reduced thickness (cross-section) of fatigue test specimens, the number of cycles to crack initiation can be approximated as the number of cycles to failure. It is apparent from Figure 5.8 that there is a relationship between pit geometry *i.e.* pit aspect ratio, applied stress and the number of cycles to failure. More specifically,

higher aspect ratio values and higher applied stress lead to shorter crack initiation times.

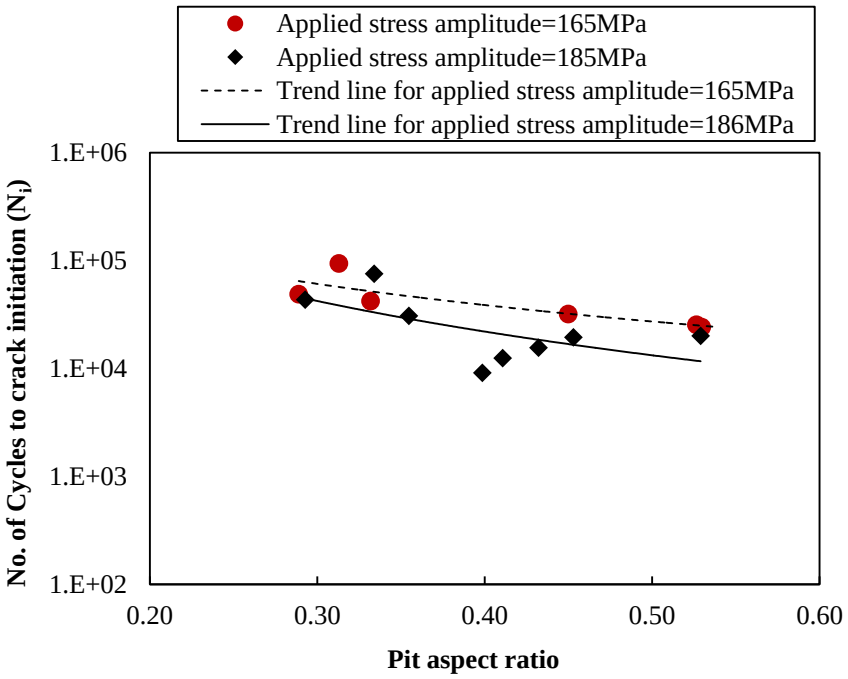


Figure 5.8. Relationship of number of cycles to crack initiation vs. pit aspect ratio at two applied stress levels.

Figure 5.9 shows the typical fracture surface observed for these specimens. Features noted include the crack origin (nucleation site), ratchet marks, fatigue and overload zone, as previously mentioned (Section 5.1.2). Figure 5.10 and 5.11 show the ratchet marks and crack origin for specimens F03 and F06. As can be seen, there are multiple crack nucleation sites around the pit. SEM images of other specimen fracture surfaces reveal the same pattern of damage with crack origins around the corrosion pits. The SEM images from the top view of the specimens show that other cracks are initiated independent of the primary crack at the corrosion pit in other geometric planes close

to the centre of the pit (Figure 5.12). However, these features are not dominant cracks and did not contribute directly to the final failure.

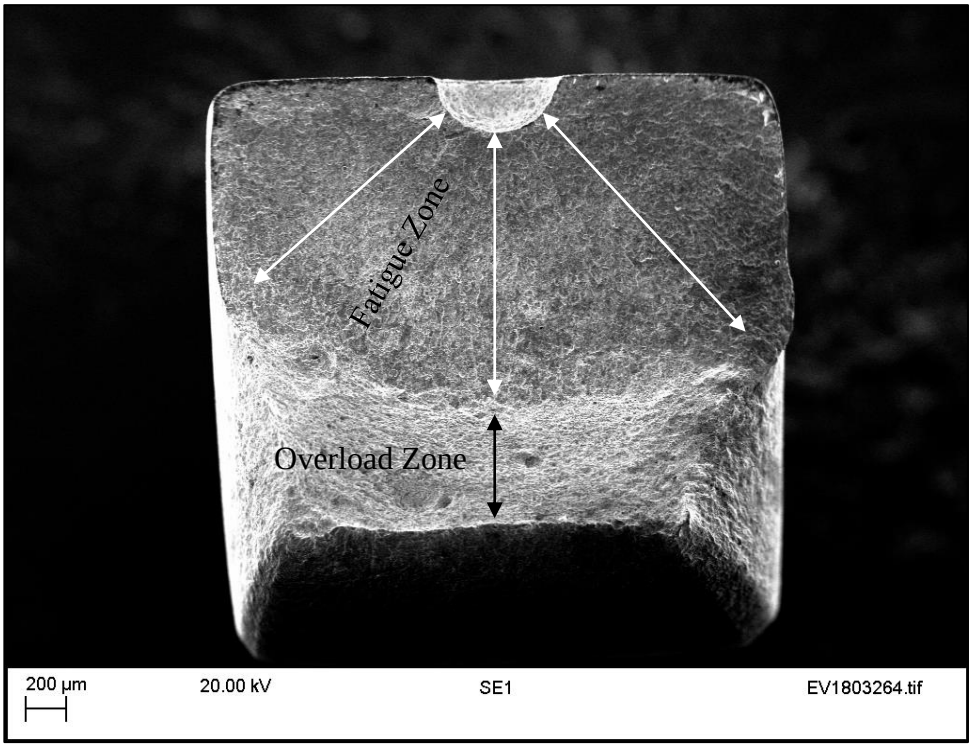


Figure 5.9. SEM image of typical fractured specimen surface tested in the sour environment.

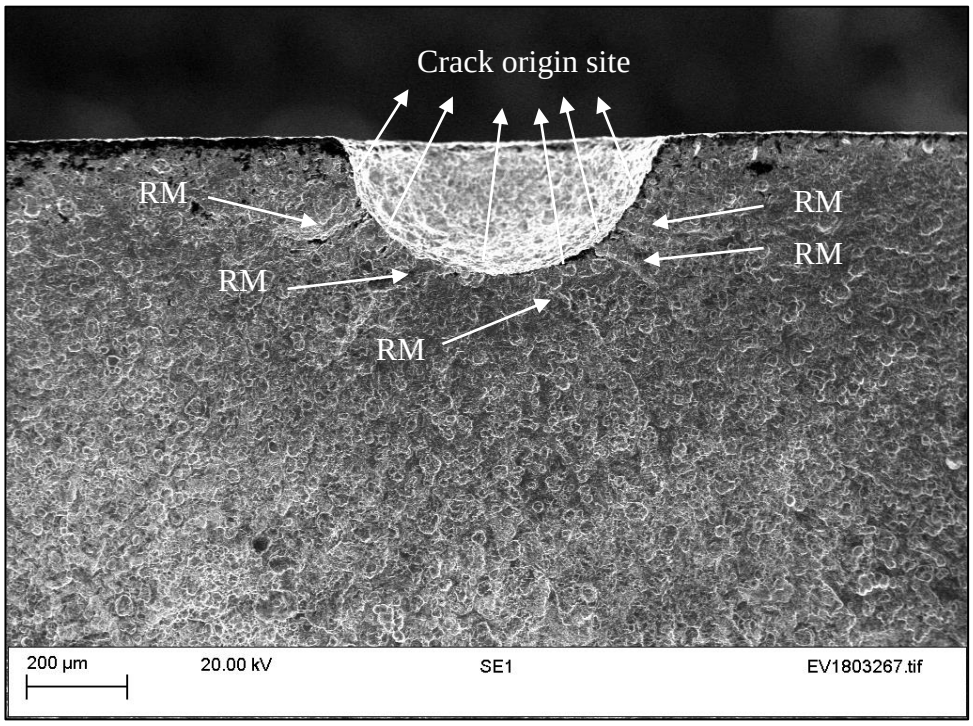


Figure 5.10. SEM image showing the ratchet marks and crack origins in specimen F03, aspect ratio 0.45, tested at applied stress amplitude of 165MPa.

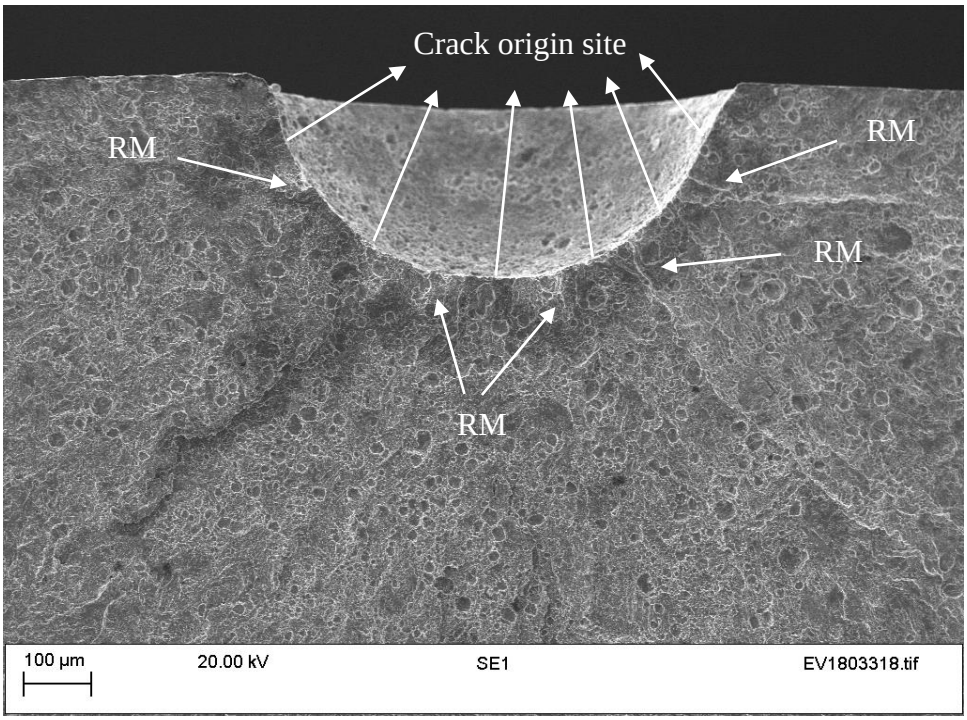


Figure 5.11. SEM image showing the ratchet marks and crack origins in specimen F06, aspect ratio 0.45, tested at applied stress amplitude of 186MPa.

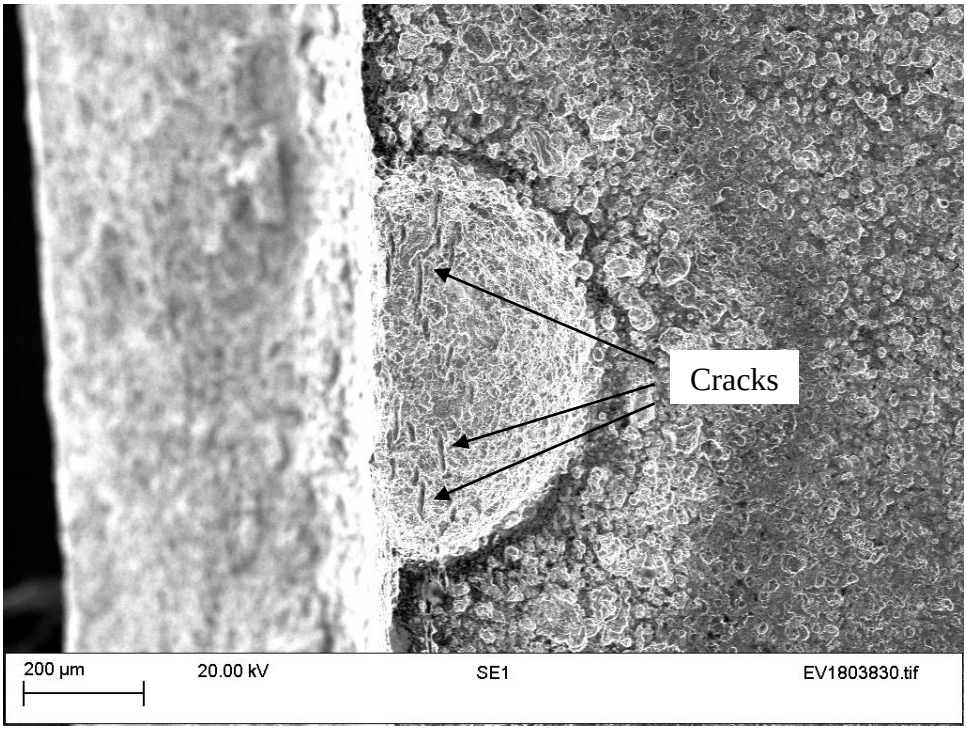


(a)

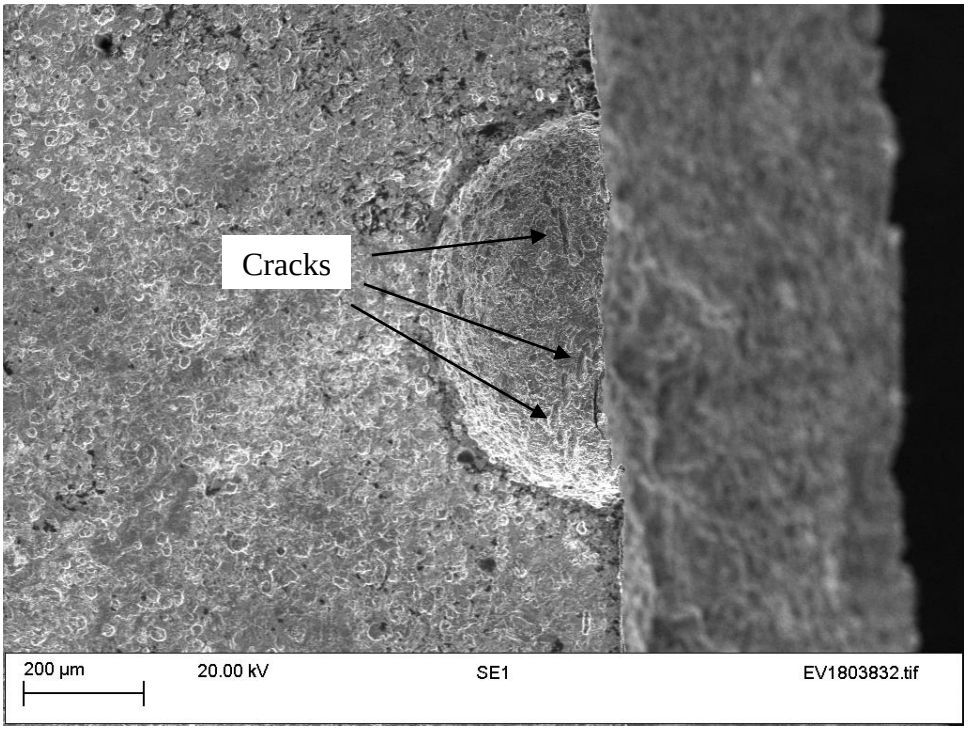


(b)

Figure 5.12. SEM images from the top view of specimen F03 showing non-propagating cracks in the (a) top half (b) corresponding bottom half of the specimen.

### 5.1.5 Pre-pitted specimens (interrupted fatigue-XCT test, in sour environment)

To investigate the pit-to-crack transition, fatigue tests for three different pre-pitted specimens were interrupted periodically at different number of cycles to allow X-ray tomography to be performed. Full details of the test procedure are given in Chapter 3. In brief, X-ray micro-computed tomography was performed using a ZEISS X-Radia 520 VersaScan instrument at TWI Ltd. in Cambridge. Proprietary software (Scout and Scan) was used to reconstruct the data obtained from the laboratory X-ray source. The corrosion pit was further analysed by commercially available image processing software, Avizo 9.4. Table 5.2 provides a summary of the scanning timeline used during periodically scanned fatigue tests, *i.e* data on the number of cycles to interruption for each test specimen, at what cycle crack were first observed via X-ray tomography and finally the number of cycles to failure. Following initial confirmation of cracking via tomography, the approach taken was to run the test to final failure. For specimen E02, the crack was not observed during interrupted cycles due to temporary limitation of access to the fatigue machine, hence the decision was taken to run the specimen to failure and start another test (*i.e.* E03 specimen).

Table 5.2: The number of cycles at each X-ray interval, the number of cycles to crack initiation observed by X-ray tomography and the number of cycles to failure.

| Specimen code | Stress amplitude (MPa) | Interrupted at (cycle numbers) | $N_i$ | $N_f$ |
|---|---|---|---|---|
| E01 | 185 | 20000, 40000 | 40,000 | 43,490 |
| E02 | 165 | 40000, 42000, 44000, 46000, 48000 | - | 94,337 |
| E03 | 185 | 13500, 14500, 15500, 17500 | 17,500 | 19,429 |

The processed X-ray images taken during tests for specimen E01 are shown in Figure 5.13, in which it can be seen that a crack initiated at the bottom of the pit with a length of 240 µm (Figure 5.13b). Figure 5.13c shows the top view of this crack in the y-direction as shown. This crack subsequently propagated and led to the failure of the specimen at 43,000 cycles (Figure 5.14). The crack propagation time was very small because of the limited thickness of the specimen. The crack initiation site is shown in SEM images in Figure 5.15. Specimens were cleaned by ultrasonication in DI water and Pyrene prior to SEM characterisation. These images show the initiation site from the bottom of the pit, thus confirming observations made through X-ray tomography during experiments tomography. Figure 5.16 reveals the presence of additional cracks at the bottom of the pit that may have been too small to be identified during X-ray tomography. As such, these cracks could have nucleated at any point during the test, but did not propagate to the same extent as the primary crack.

A key advantage of the *in-situ* corrosion fatigue procedure developed during this study is that it enables the researcher to monitor a crack initiated not only from the surface, but also from the walls and base of the pit, without the need to remove the specimen from the test the cell. This is advantageous as it avoids the risk of exposing the specimen to air, leading to undesirable chemical reactions and thus disqualifying the test. Also, the detailed evolution of fatigue crack can be monitored by interrupting the test more frequently (e.g. every 1000 cycles) upon detection of the initial crack. The outlined test protocol has the potential to provide a more thorough understanding of the pit-to-fatigue crack transition mechanism than has previously been the case.

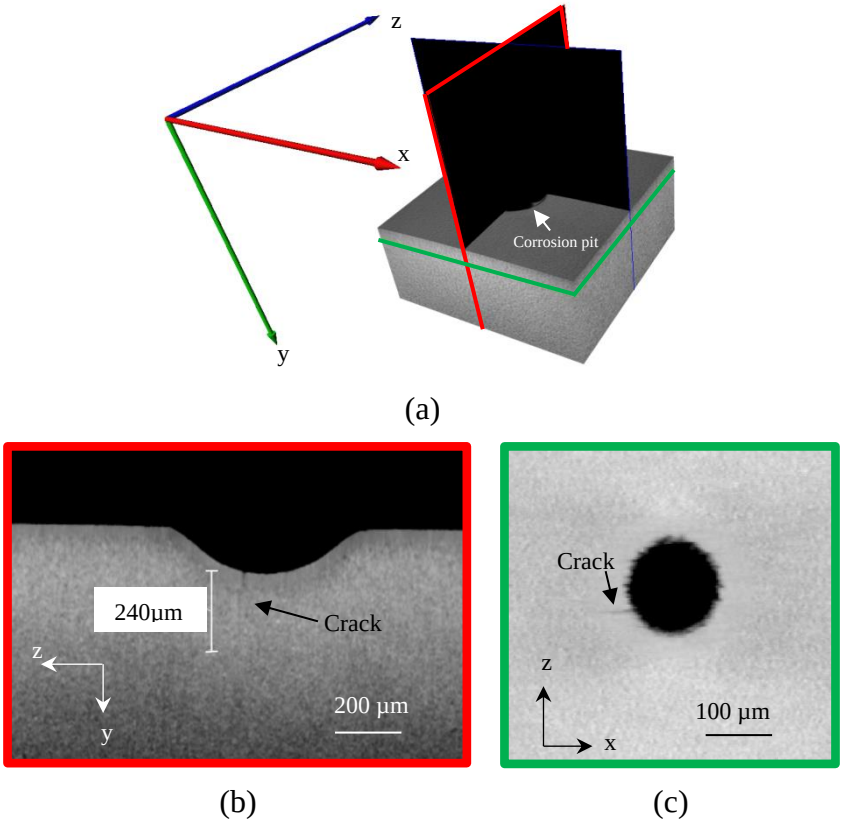


Figure 5.13. (a) 3D view of X-ray tomography processed images of corrosion pit from Specimen E01 after 40,000 load cycles with z-axis being the loading direction. (b), (c) y-z slice and x-z slice through the specimen showing an initiated crack from pit base.

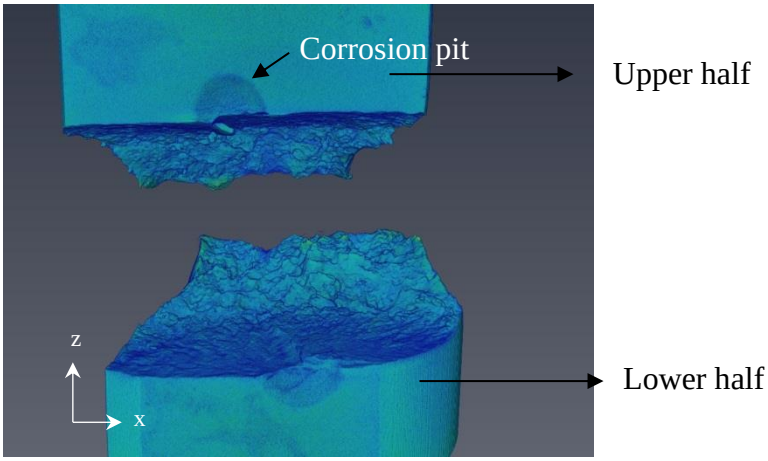


Figure 5.14. Top view of the processed X-ray images of a failed specimen.

A current limitation of this lab-based methodology is the restriction placed on test specimen size, due to the increasing artefacts in X-ray images and a decrease in the

resolution of the image with increasing size. As a result, the maximum cross-sectional area for scans was limited to no greater than 3x3 $mm^2$.

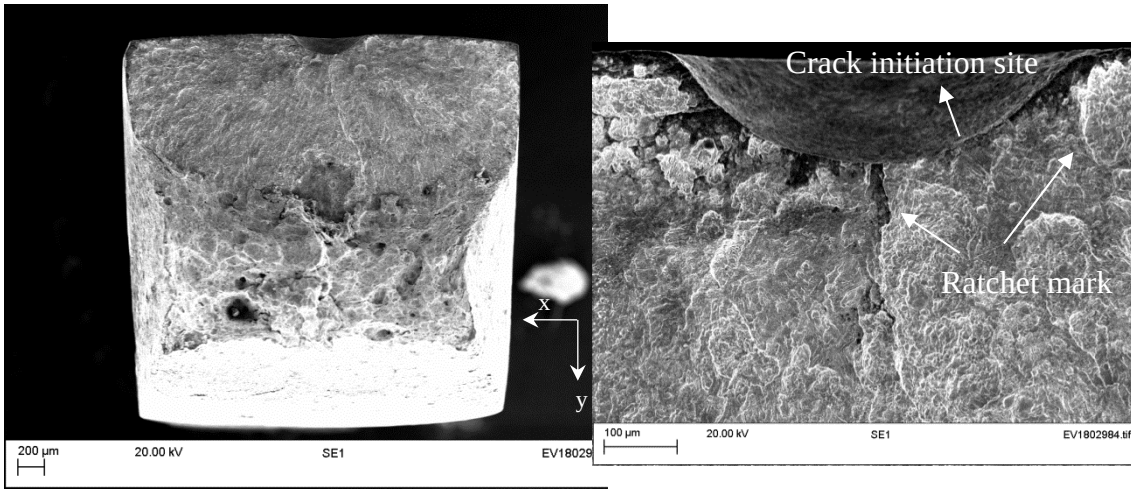


(a) (b)

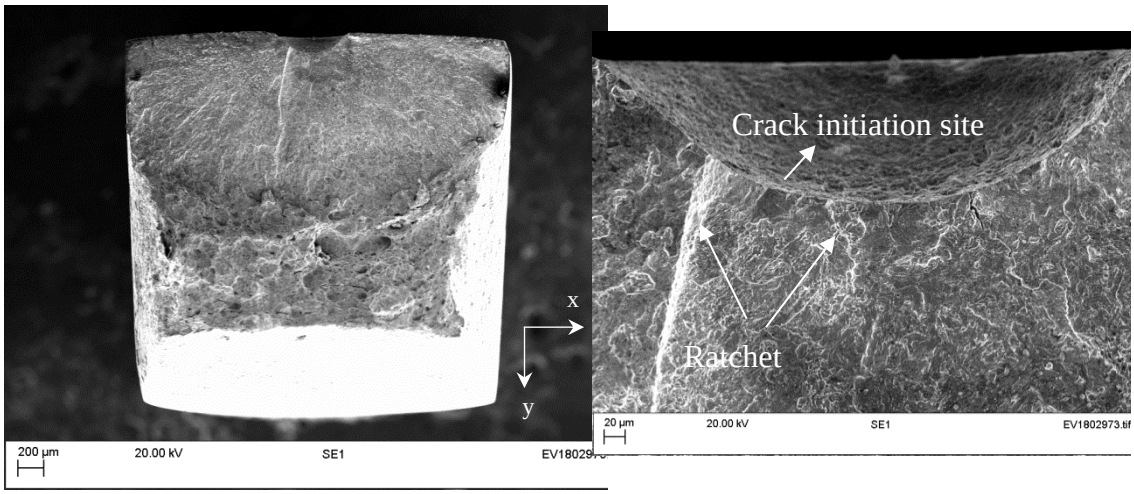


(c) (d)

Figure 5.15. SEM images: (a), (b) lower half, (c), (d) upper half of the failed specimen (refer to Figure 5.14 for the upper and lower half definition).

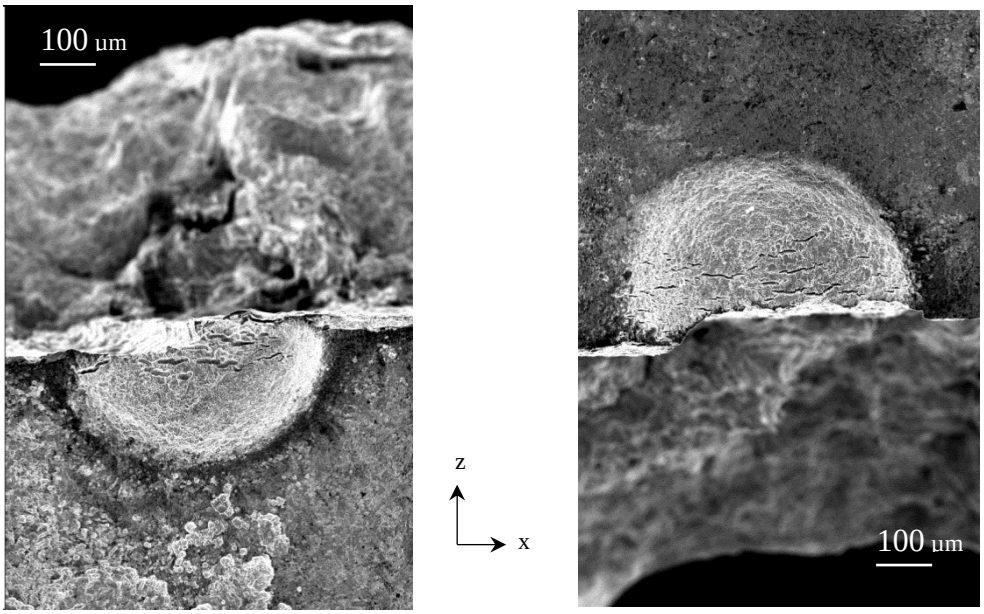


(a) (b)

Figure 5.16. SEM images (a) lower half (b) upper half of the failed specimen.

## 5.2 Numerical and analytical results

In this Section, 3D FEA has been conducted by employing ABAQUS to evaluate the stress and strain around single corrosion pits (i.e. a pit assumed to be a notch) possessing a range of different geometries. The stress and strain distribution around a pit in API 5L-X65 steel specimen was analysed using an elastic-plastic material model and applying a static or cyclic load. An assessment of the relationship between pit size and maximum stress and strain is provided.

### 5.2.1 Static stress-strain analysis

#### *5.2.1.1 Hemispherical pit*

Stress and strain contours around a pit were plotted for half-plate model (Figures 5.17 and 5.18). The stress distribution (stress in the load direction) for two different pit

depths is shown in Figure 5.17. It can be seen that stress is highly localized (red area) at the pit base for both pit depth values investigated. Furthermore, the maximum stress does not increase markedly with increased pit depth. Figure 5.18 provides the strain contours in the load direction. It is clear that when the pit depth is smaller, strain is localized near the pit mouth, whereas for increasing the pit depth the maximum strain increases and the location is shifted to the bottom of the pit. A possible explanation for this observation could be that localization of stress at the pit base may decrease the constraint near the pit mouth, leading to plastic strain localization in that area. Importantly, these areas of high strain localization are more likely to be sites for crack initiation under static loads. The results suggest that when the pit depth is small (*i.e.* $a/t$ is about 0.06), the crack may initiate near the pit mouth, whereas when the pit depth increases (*i.e.* $a/t$ is about 0.3), the crack may emanate from both pit mouth and bottom, *i.e.* locations of strain localization. These results are in good agreement with those obtained in the literature (Turnbull, A. et al. 2009, Horner et al. 2011).

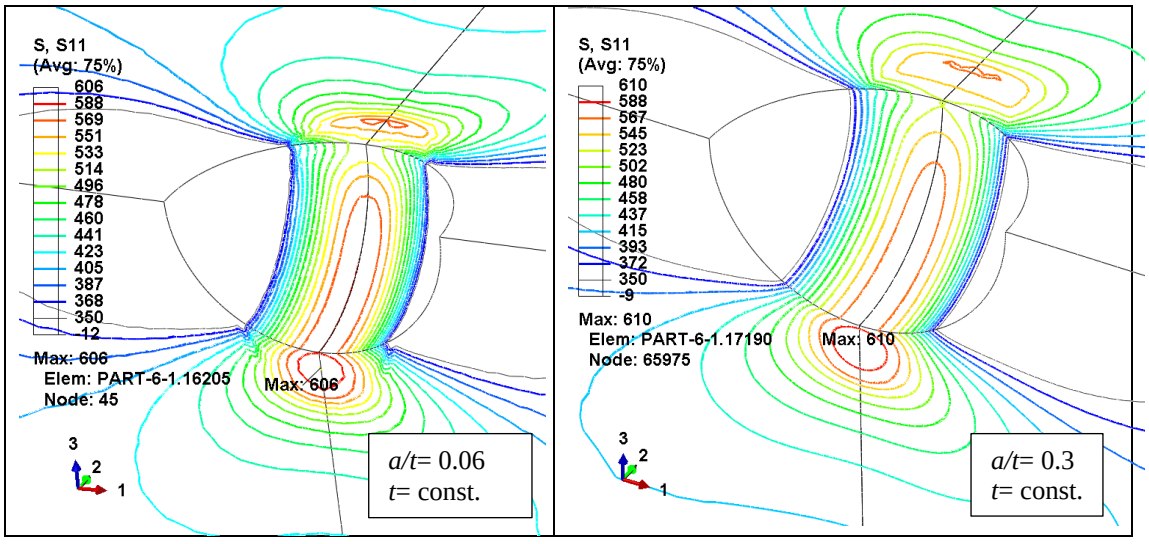


Figure 5.17. Stress component in the load direction for pit depth to plate thickness ratios of 0.06 and 0.3.

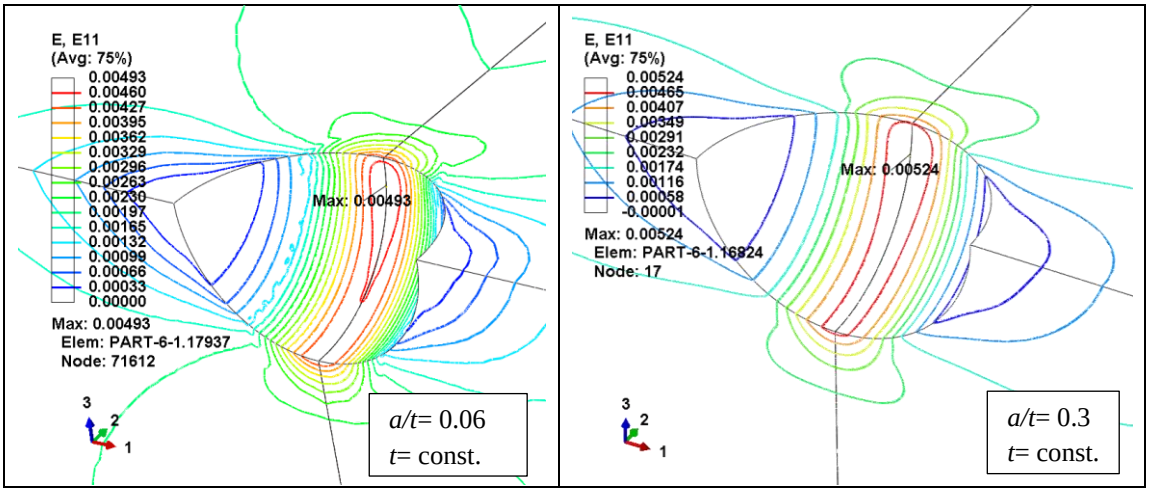


Figure 5.18. Strain in the load direction for pit depth over plate thickness ratios of 0.06 and 0.3.

Figures 5.19 and 5.20 present the maximum stress and strain respectively against the normalized value of hemispherical pit depth (*i.e.* pit depth divided by plate thickness). The maximum stress in each direction around the pit does not change considerably upon increasing the pit depth. This is to be expected, as after the local material has yielded, the stress increment is insignificant as evident in the monotonic stress-strain curve of the material. However, the maximum strain in the load direction (Figure 5.20) is increased with the increasing pit depth. These results suggest that under static loading, stress-based analysis should not be applied after the local material yields and that strain-based analytical strategies may need to be employed for pit-to-crack transition life prediction. This statement is supported by literature concerning components with corrosion pits, for which the behaviour of material at the regions of pits is best considered in terms of strain (Stephens, R. I. et al. 2000).

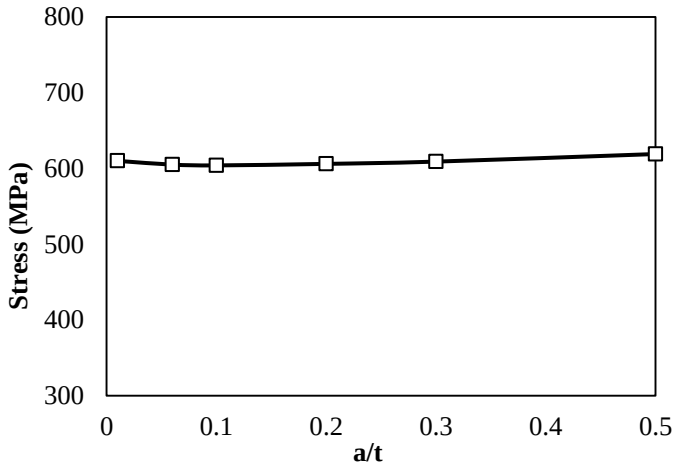


Figure 5.19. Hemispherical pit: maximum stress in loading direction vs. ratio of pit depth to plate thickness.

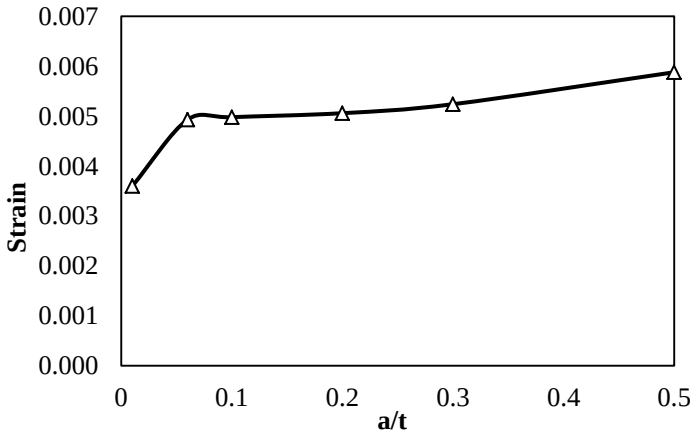


Figure 5.20. Hemispherical pit: maximum strain in loading direction vs. ratio of pit depth to plate thickness.

The volume of plastic deformation was also evaluated by FEA, to study the change of plastic zone volume with respect to pit size (pit volume). Figure 5.21 presents the relationship between the normalized value of plastic zone volume (*i.e.* plastic zone volume divided by pit volume) and the normalized value of pit depth (pit depth divided by plate thickness). This plot reveals that the larger the pit, the larger the plastic zone volume that is what is expected. Figure 5.22 shows the changes in strain

for a normalized value of plastic zone size. It is particularly interesting to note the sudden increase in maximum strain when the normalized plastic zone volume reaches a value of 0.2. The normalized pit depth ($a/t$) at this point is 0.06. A sudden increase in the strain also can be seen at this point ($a/t$ = 0.06) in Figure 5.20. It follows that this point may reflect the critical pit depth for transition into the crack under static loading.

The implications of this result may be important and warrant further discussion. The working hypothesis is that the ratio of plastic zone volume over pit volume may provide a threshold value for critical pit condition from which cracking may initiate. The relationship between normalized plastic zone volume and critical pit condition can be verified by empirical studies. In this project the focus of experimental study has been cyclic loading and due to time limitations no further experiments have been carried out under static load to verify the hypothesis or otherwise.

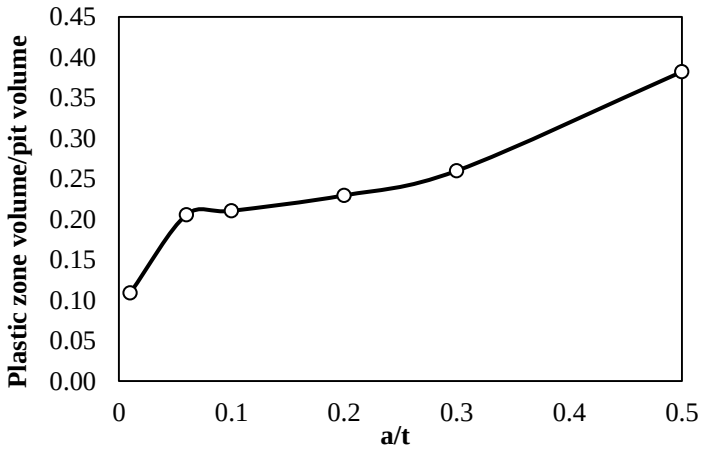


Figure 5.21. The relationship between normalized plastic zone volume (plastic zone volume divided by pit volume) and normalized pit depth (pit depth divided by plate thickness).

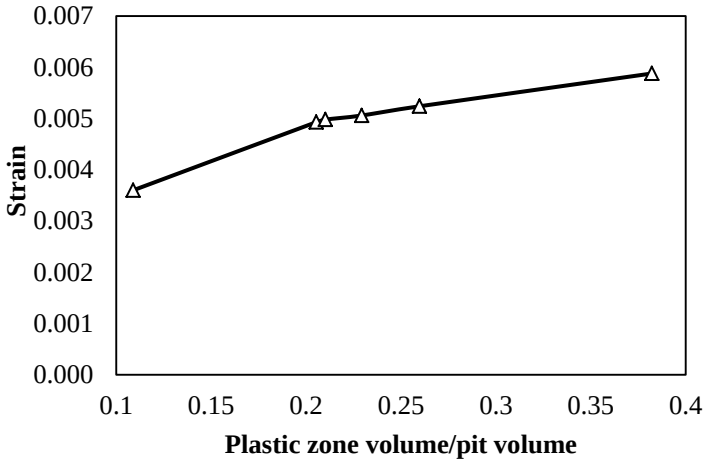


Figure 5.22. Maximum strain in load direction vs. normalized plastic zone volume.

#### *5.2.1.2 Semi-elliptical pit*

For the semi-elliptical pit, stress and strain contour maps (Figures 5.23 and 5.24) show the same pattern of localization as the hemispherical pits. The maximum stress is concentrated at the bottom of the pit for different aspect ratios, but the strain is localized near the pit mouth. As the aspect ratio is increased, the strain localization is also shifted to near the pit bottom. It is, therefore, likely that when the pit aspect ratio is small, the crack may initiate near the pit mouth but when the pit aspect ratio increases, cracks may equally originate from the pit base.

Figures 5.23 and 5.24 provide contour plots of the maximum stress and strain in the loading direction. It can be seen that by increasing the pit depth, the maximum stress and strain increase until the ratio $a/t$ reaches a value of 0.3, whereupon the maximum stress and strain tend to remain constant. The effect of pit width, $2c$, is also shown in these figures. These data suggest that an increase in the value of $c$ will decrease the maximum stress and strain.

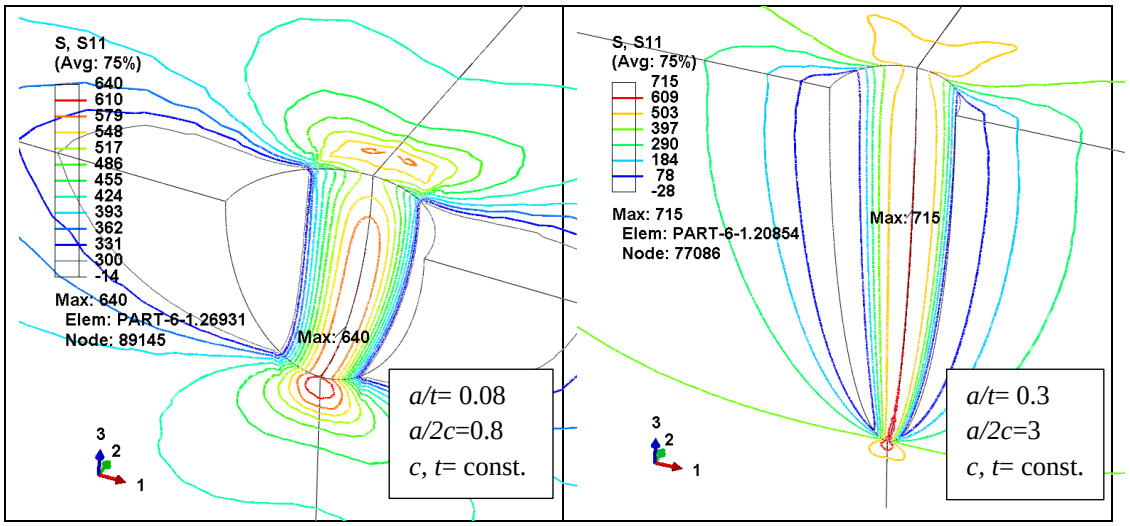


Figure 5.23. Stress in load direction for pit aspect ratios 0.8 and 3.

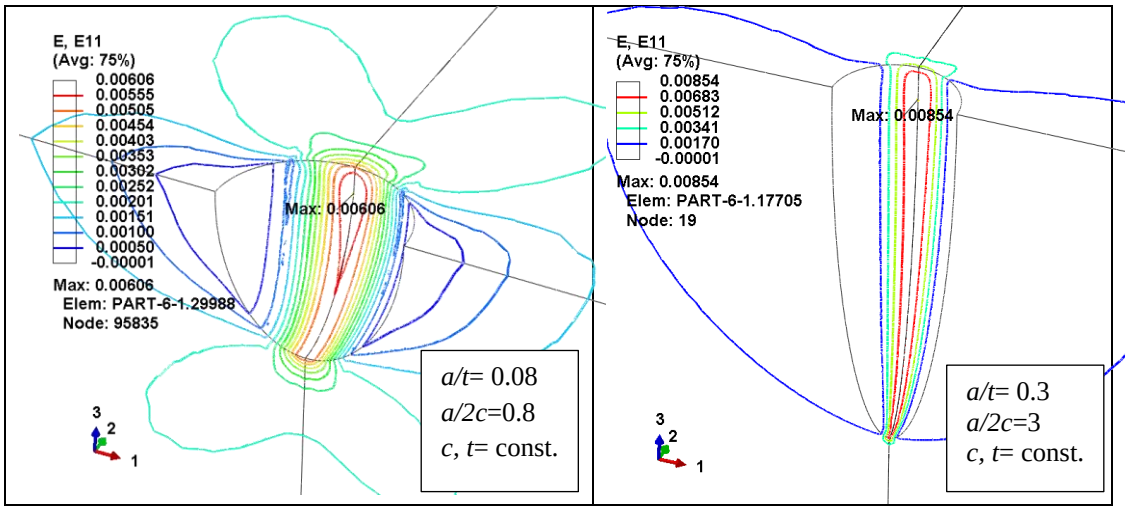


Figure 5.24. Strain in load direction for pit aspect ratios 0.8 and 3.

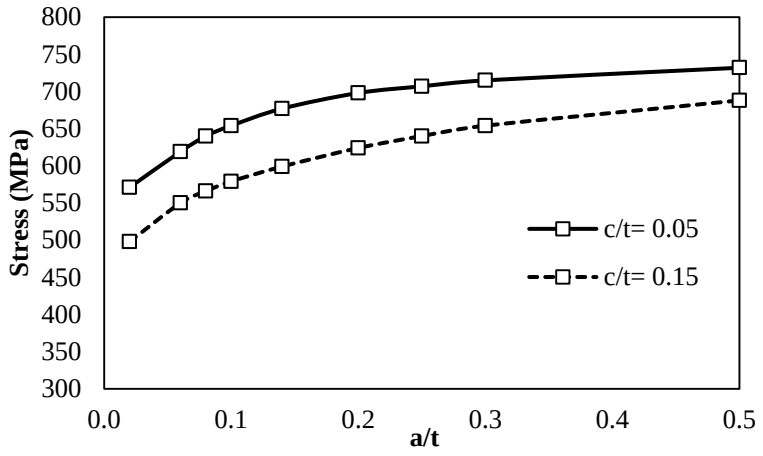


Figure 5.25. Maximum stress in load direction vs. pit depth over plate thickness ratio.

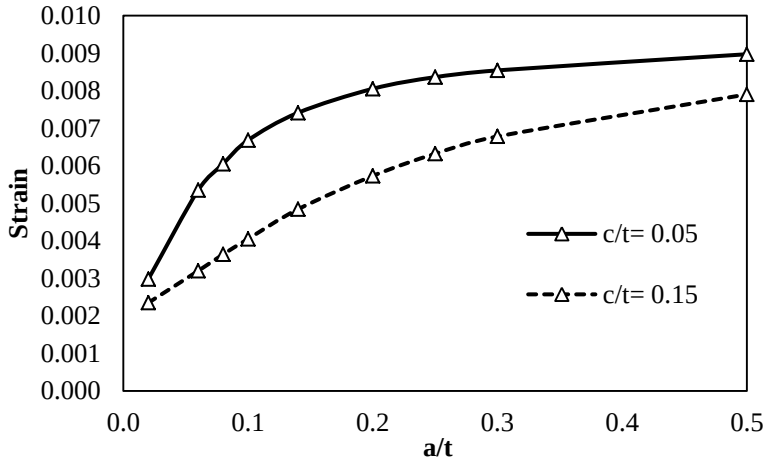


Figure 5.26. Maximum strain in load direction vs. pit depth over plate thickness ratio.

The pit maximum stress and strain were also evaluated using the Neuber's rule (Stephens, R. I. et al. 2000) and compared with the FE results (Figures 5.27 and 5.28). Figures 5.27 and 5.28 reveal that Neuber's rule underestimates the stress and overestimates the strain. This result is not unexpected, as analytical methods such as Neuber's rule cannot provide a high level of accuracy when plastic deformation is involved and thus can only be used to provide an initial approximation. Computational

analysis and/or experimental measurement are expected to provide more realistic results (Zeng and Fatemi, A 2001). The divergence in results obtained using FEA and Neuber's methods are much reduced when the applied stress is low and close to 10% of the material yield strength (Figure 5.29). These results are in agreement with a published study (Zeng and Fatemi, A 2001).

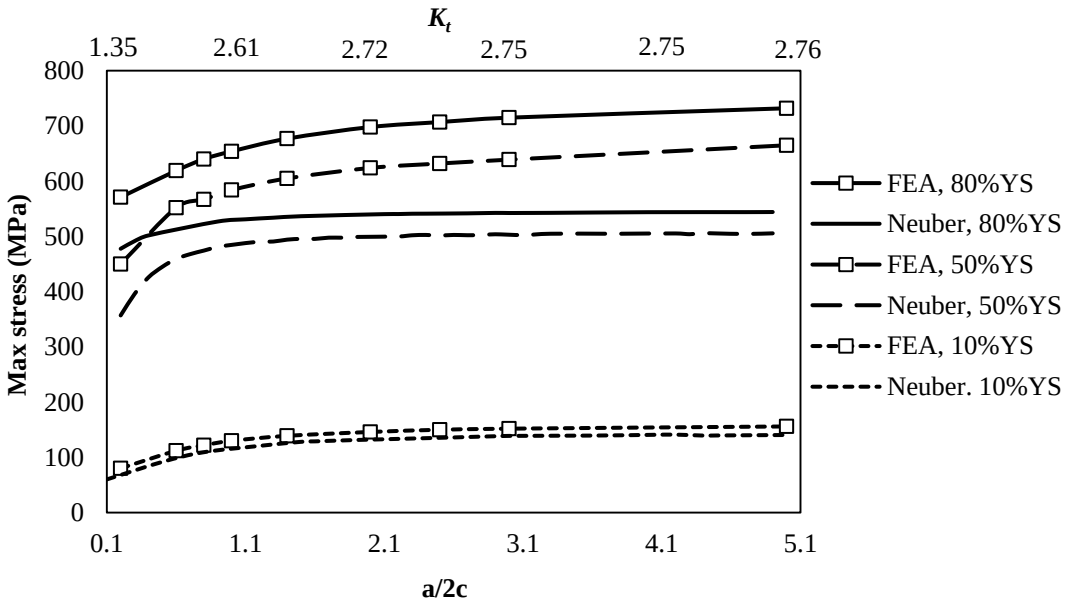


Figure 5.27. Comparison of FEA and Neuber's rule calculated the maximum stress in load direction vs. pit aspect ratio (and $K_t$) for applied stress of 10%YS, 50%YS and 80%YS (square mark shows stress obtained from finite element simulations).

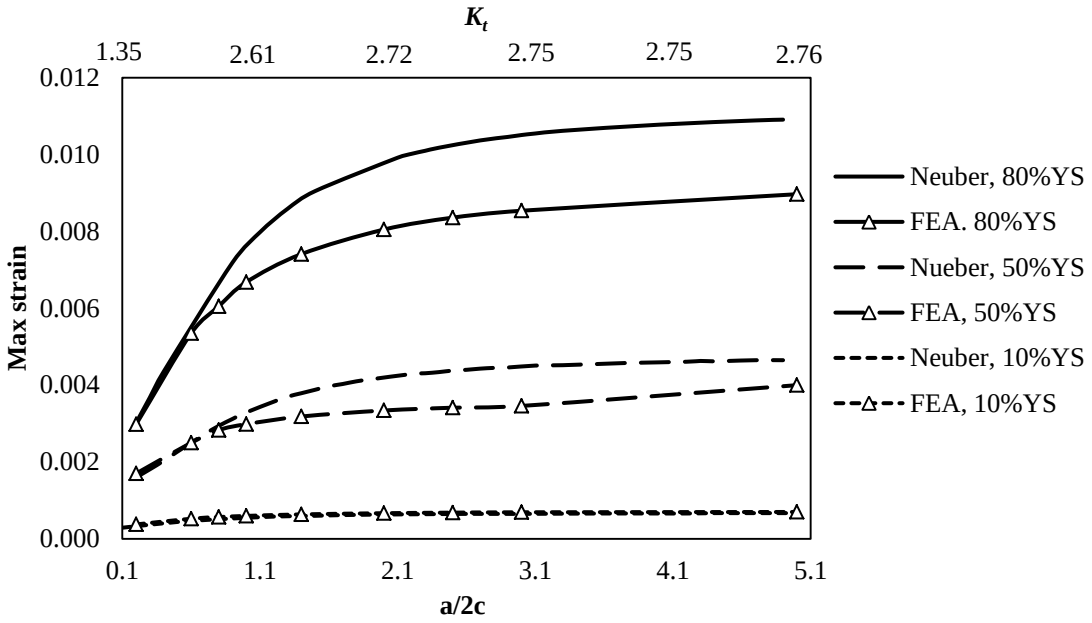


Figure 5.28. Comparison of FEA and Neuber's rule calculated the maximum strain in load direction vs. aspect ratio (and $K_t$) for applied stress 10%YS, 50%YS and 80%YS (triangle mark shows strain obtained from finite element simulations)..

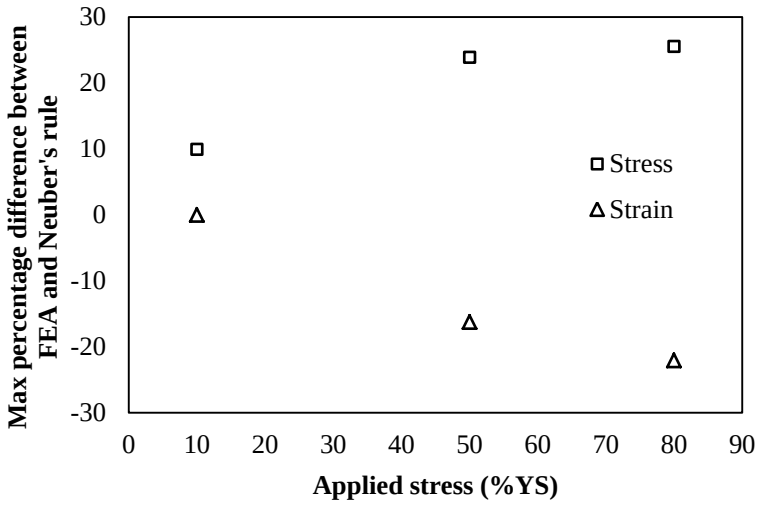


Figure 5.29. Maximum percentage difference between FEA and Neuber's rule.

Figure 5.30 shows normalized plastic zone volume vs. normalized pit depth. Considerable plastic deformation occurs around the pit, which increases with the increase of pit depth. The increase in plastic zone volume is also expressed in terms of

pit aspect ratio in Figure 5.31. Results suggest that the size of the plastic deformation zone is a function of both pit depth and the pit aspect ratio.. Results are in agreement with a recent study of the development of the plastic zone around a pre-existing corrosion pit on the surface of a steel pipe (Rajabipour and Melchers 2013). Again, it may be hypothesized that the ratio of plastic zone volume over pit volume may be the controlling factor that defines the critical pit size and crack initiation under static loading.

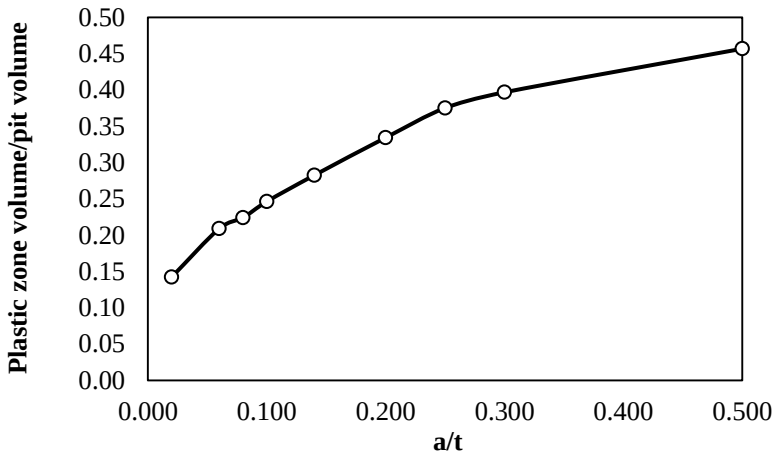


Figure 5.30. The relationship between normalized plastic zone volume and normalized pit depth.

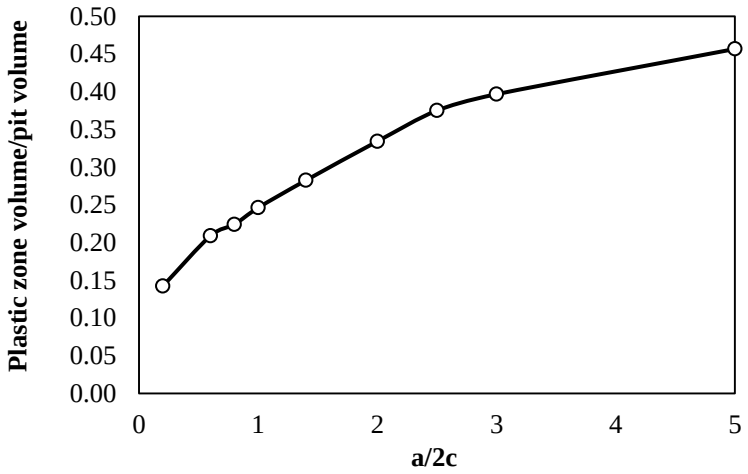


Figure 5.31. The relationship between normalized plastic zone volume and pit aspect ratio.

This part of study was set out to extend the understanding of pit-to-crack evaluation in API 5L-X65 steel. Strain contours of two pit geometries studied in this work confirm that for high values of applied static stress (80%YS), the maximum strain localization occurs near the pit mouth when the pit depth is small. When the pit depth is increased, the maximum strain localization occurs near the pit bottom. In both cases, the maximum strain localization indicates the likely locations for crack initiation from a pit under static loading. The plastic zone size was studied in terms of a dimensionless parameter ($a/t$). Considerable plastic deformation occurs around the pit when the applied stress is 80%YS, which changes with changing pit geometry. Another finding is that the ratio of plastic zone volume to pit volume may provide a threshold value for the critical pit size and thereby provide information on the predicted site(s) for crack initiation. These findings may enhance understanding of pit-to-crack evaluation in API X65 steel under static loading. A key strength of the present study is the use of an elastic-plastic material model, which allows a more realistic study of the pit-to-crack process.

### 5.2.2 Cyclic stress-strain analysis

To study the behaviour of a corrosion pit under cyclic loading, elastic-plastic FEA was carried out on a specimen containing a pit under the cyclic load-controlled condition at a fixed stress ratio of 0.1 with different stress amplitudes. Figure 5.32 presents the as-calculated stress-strain hysteresis loops of a node at the base of the pit in three different applied stress amplitudes, for a pit with an aspect ratio of 0.54 (*i.e.* pit number 3 in Table 4.2). The stable condition was reached in these loops, *i.e.* stress-strain loops no longer change shape from one cycle to another. This illustrates that the stress-strain hysteresis is fully elastic when the applied stress amplitude is less than 146 MPa. At higher applied stress amplitudes, a plastic deformation is seen at the first cycle, but the stress-strain response becomes linear during subsequent cycles. This cyclic plastic deformation process can lead to multiple crack initiation at the relevant locations in the pit (Htoo et al. 2016), as observed during the present study and evidenced in SEM fractography images. The variation of the local stress ratio across this pit cross-section is shown in Figure 5.33. Of particular note is that by increasing the applied stress value and maintaining the applied stress ratio at 0.1, the pit local stress ratio decreases from 0.1 to -0.2. To understand this local behaviour of stress-strain response, the plastic strain around the pit was investigated by elastic-plastic FEA. The plastic strain distribution around the pit in the first cycle is presented in Figure 5.34 for the same pit geometry. It is seen that for this pit morphology, plastic deformation is developed near the pit base when the applied stress amplitude is 146MPa or 164MPa. Comparison of Figure 5.33 and 5.34 reveals that where plastic strain occurs, the local stress ratio is decreased to a negative value, which means a compressive local stress has developed at the unloading reversal. Although this

behaviour is counter-intuitive to some extent, it can be rationalised relatively simply. When the applied stress reaches the maximum value, the plastic area experiences tensile stress but when the applied stress reaches the corresponding minimum, a compressive stress develops in the plastic zone because it is surrounded by a counterbalancing elastic region that can be considered to be an effective constraint. This compressive stress thus reduces the mean stress and the local stress ratio. This mechanism can be confirmed by comparing Figure 5.33 (showing the local stress ratio for different applied stress) and Figure 5.34, showing that for higher applied stress, plastic deformation occurs and that it decreases the local stress ratio where plastic strain is observed.

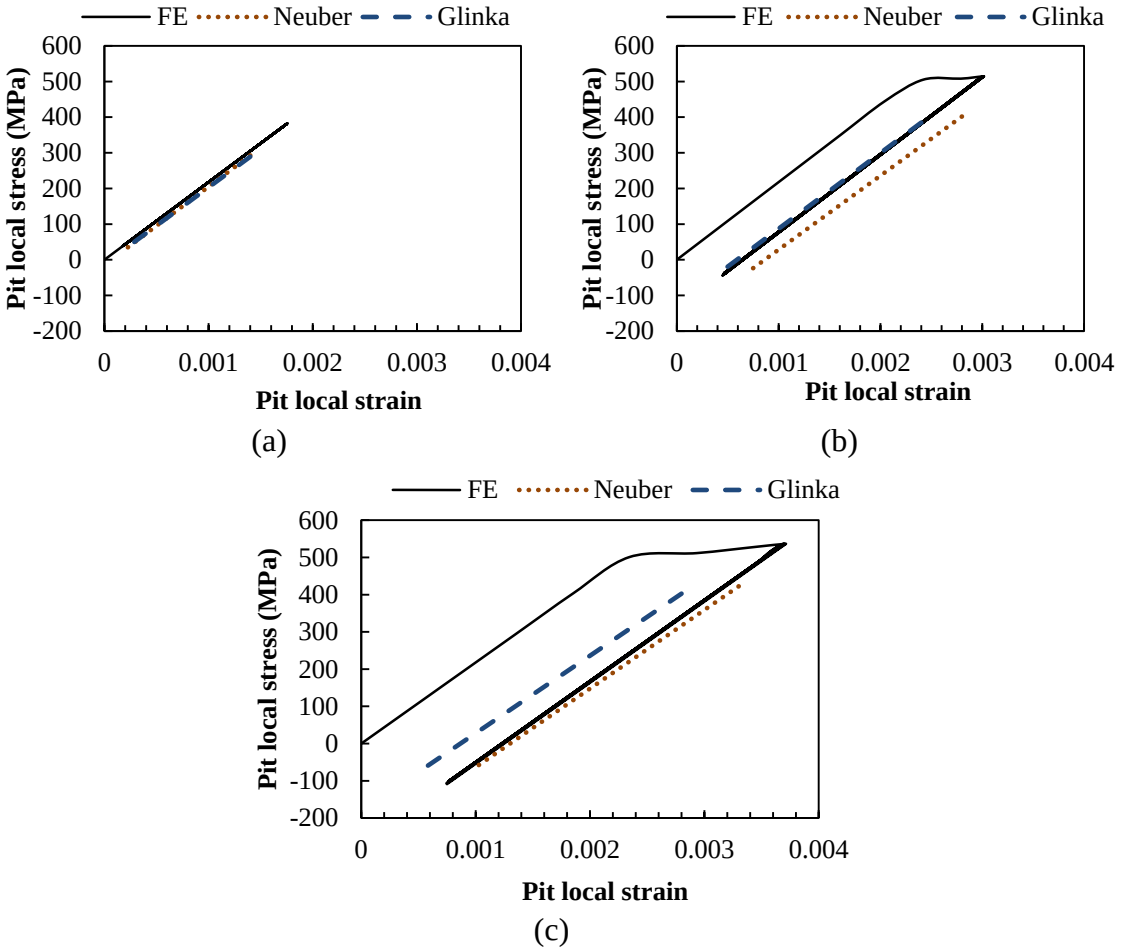


Figure 5.32. FEA delivered local Stress-strain curves for pit aspect ratio of 0.54 at the pit base in a) applied stress amplitude 90 MPa, b) Applied stress amplitude 146 MPa, c) Applied stress amplitude 164 MPa.

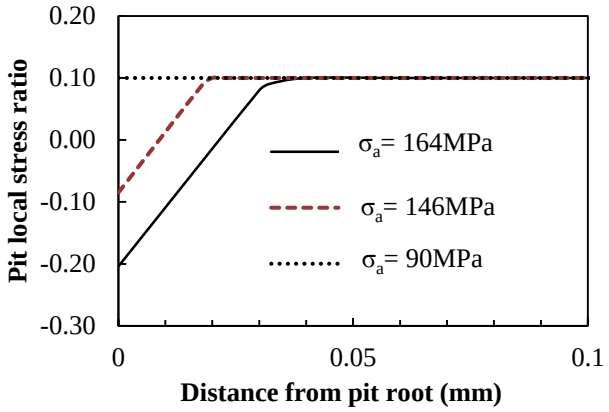


Figure 5.33. Pit local stress ratio change along the distance from the pit root for pit aspect ratio of 0.54.

The results suggest that plastic deformation around the pit leads to a local compressive stress and a decreased local stress ratio. Collectively, these results are in line with previous studies on fatigue behaviour of notches (Htoo et al. 2016) and provide an important insight in understanding the behaviour of corrosion pits under fatigue loading. The authors further note that the areas with the stress ratio less than zero, which are under compression, are likely to be cathodic in an electrolyte (i.e. corrosion salt solution as used in present study) relative to the adjacent regions under tension (which will be anodic).

The maximum and minimum stress and strain at the pit were also calculated by Neuber's rule and Glinka's rule, under the same cyclic loads, and are compared with the hysteresis loop obtained from FEA in Figure 5.32. It is shown that as the applied stress increases, the difference between the stress or strain range obtained by FEA and analytical models increases. It also reveals that these two analytical models underestimate the stress range and strain range. Further analysis of data provided in Figure 5.32 (*i.e.* calculating the local stress ratio from three different methods)

indicates that the local stress ratio from Neuber's rule and Glinka's rule calculated for all levels of applied stress are close to the local stress ratio obtained from FEA (Figure 5.35). Finally, Figure 5.35 appears to indicate that the Glinka approach shows a closer estimation to the FEA results at highest applied stress amplitude.

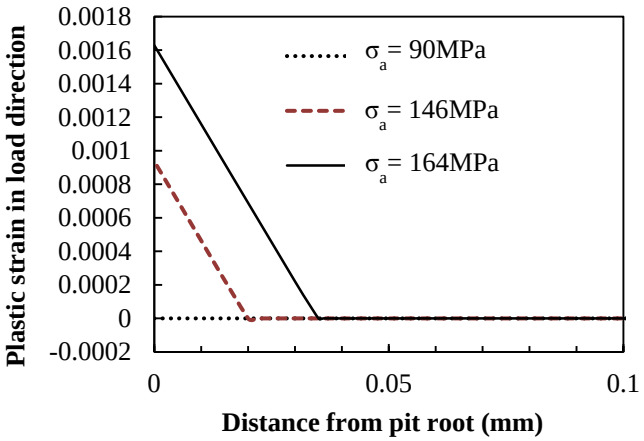


Figure 5.34. The plastic strain along the distance from pit root obtained by FEA in the first cycle for pit aspect ratio of 0.54.

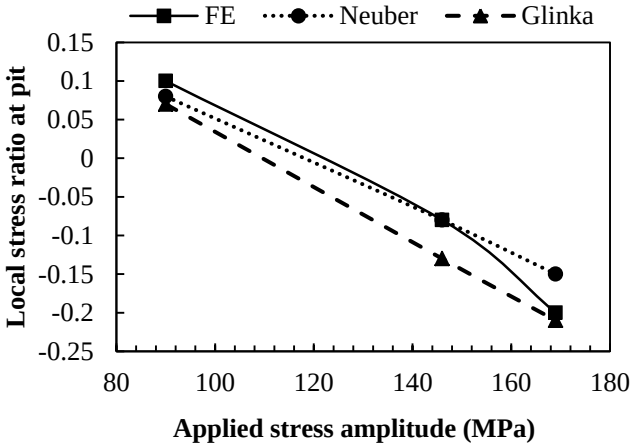


Figure 5.35. Pit local stress ratio obtained by FEA, Neuber and Glinka's rule for pit aspect ratio of 0.54.

In reviewing the literature, it became apparent that no previous study had been performed on FEA of corrosion pits under cyclic loading. To assess the effect of pit morphology on pit fatigue behaviour, the local stress ratio for different pit shapes was

obtained using FEA. The reader is reminded that an applied stress ratio at the macroscale will impose a local pit stress ratio at the microscale level. The consequences of this are made apparent in the following text.

Figure 5.36 presents the relationship between pit aspect ratio and pit local stress ratio. There is a clear trend of decreasing pit local stress ratio with increasing pit aspect ratio and applied stress, a result that is rather significant. It is clear that when the applied stress amplitude is low (90 MPa), the local stress ratio remains the same as the applied stress ratio for all pit geometries, meaning that the pit geometry does not affect the local stress ratio at the pit when the applied stress is low. These results are likely to be related to plastic deformation around the pit. For lower pit aspect ratios and applied stress, no plastic deformation occurs, therefore, the local pit stress ratio remains the same as the applied stress ratio. By contrast, in the case of increasing pit aspect ratio and/or applied stress, plastic deformation increases resulting in lower local stress ratio and lower local mean stress. Taken together, these results suggest that there is an association between plastic deformation around the pit and the local stress ratio. To find the effect of pit geometry on local amplitude stress occurring at the pit, the relationship between pit aspect ratio and local maximum stress is shown in Figure 5.37. It is seen that for all levels of applied stress, pit geometry has a significant effect on local stress experienced in this area. However, it is also apparent that the rate of increase in local maximum stress decreases as the pit aspect ratio increases.

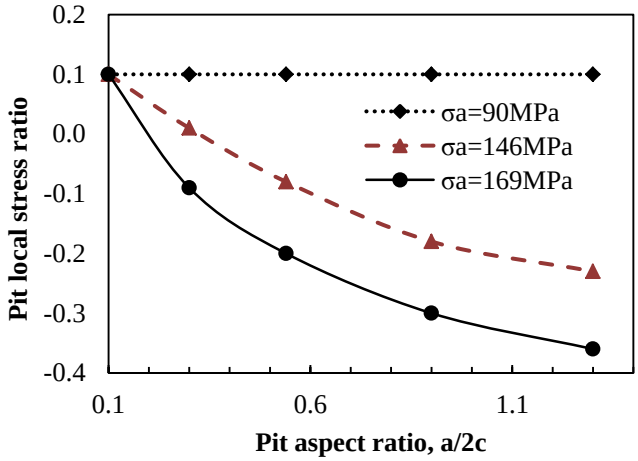


Figure 5.36. Local stress ratio as function of pit geometry under different applied stress values.

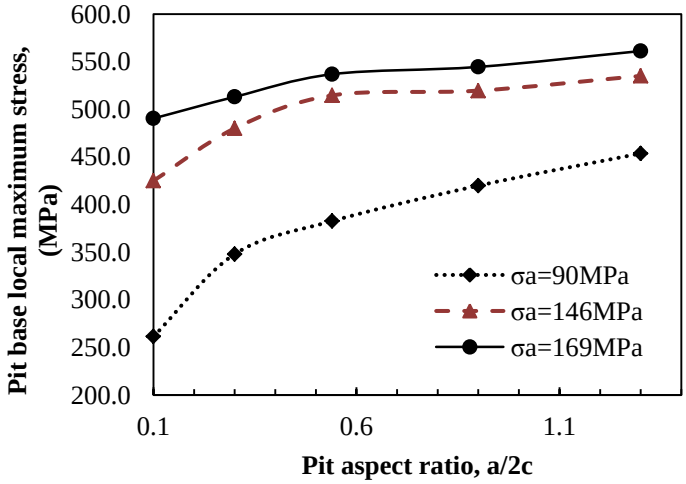


Figure 5.37. Pit base maximum stress vs. pit aspect ratio.

## 5.3 Life prediction

### 5.3.1 Ambient air

The prediction approach used in this Section is described in Chapter 4, and in short is to combine the elastic-plastic FE stress/strain analysis (for both loading and unloading

reversals in a load cycle) with material's S-N data (or the Strain-Life data in the case of higher applied load, e.g. in the low cycle fatigue regime). In this study, the strain-life data is expressed by the Smith-Watson-Topper (SWT) equation. The SWT approach (Eq. 4.13) was used to predict the fatigue life in terms of the initiation of a small crack of the order of 1mm at the pit under cyclic loading, *i.e.* crack initiation life $N_i$, by using the local stress and strain of the location where the maximum stress occurs when stress-strain loops become stable. This location was found to be on the pit wall for all the geometries by FE modelling. The crack initiation life, determined using a combination of FEA and SWT, is shown in Figure 5.38 (showing the effects of pit aspect ratio and applied stress). It is shown that under the same applied stress, the pit with an aspect ratio of 1.3 is the most critical pit because of shorter crack initiation life.

The Gerber equation (Eq. 5.2) and the *S-N* data for R= -1 in Figure 5.1 was also used to predict crack initiation life by using the local stress amplitude and the local mean stress obtained from the FEA at the location where the maximum stress occurs at the pit when the stress-strain loops become stable. Figure 5.38 presents these prediction data.

Comparing the two prediction approaches, Figure 5.38 shows that for the lower aspect ratio of 0.54 the two methods give similar predicted life, whereas increasing the aspect ratio (higher local stresses and strains) will increase the difference between the two predictive approaches. At a lower applied stress amplitude of 90MPa, the *S-N* approach predicts a longer crack initiation life than that by the SWT method, although it was expected to be the same values at this stress level as there is no plastic strain in

all the pits. At two higher applied stress values, the *S-N* approach predicted shorter fatigue life.

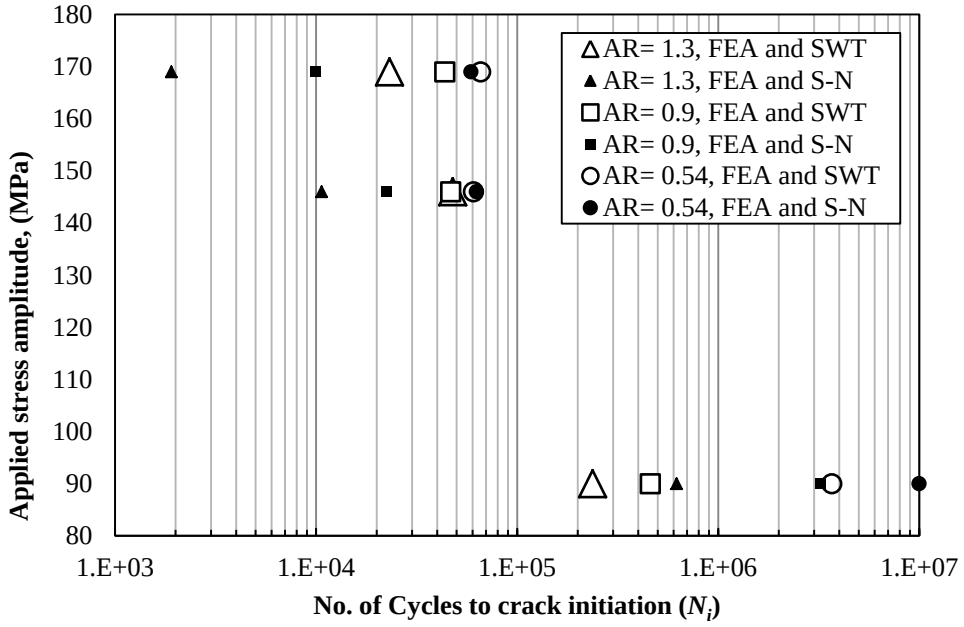


Figure 5.38. Crack initiation life from different pit aspect ratios (AR) vs. applied stress amplitude using the prediction method combining FEA and SWT or FEA and theoretical S-N curve in Figure 5.1.

The experimental results in air reported in Table 5.1 are compared with predicted load cycles to crack initiation in Figure 5.39. As mentioned earlier due to the limited thickness of the fatigue test specimens *i.e.* 3mm, the number of cycles to crack initiation was considered to be very similar to the number of cycles to failure. The difference in values was estimated to be of the order of 7% of the fatigue life, as evidenced through X-ray tomography analysis. The ordinate (y-axis) in Figure 5.39 corresponds to the elastic-plastic local stress amplitude at the pit base, which for prediction 1 and 2 is calculated by FEA, and for experimental data is predicted by Glinka's rule. As shown by this figure, the predicted lives by both prediction methods were in good agreement with the experimental results (*i.e.* for a given life, the relative

error in local stress amplitude lies in the range 8-10%). For lives higher than about $1.5\times10^5$ cycles, where the two prediction approaches coincide, the local stress amplitudes of experimental results are closer to prediction 2 and for lower lives are closer to prediction 1. This can explain in terms of lower lives where the cyclic plasticity could be higher and where the SWT approach accounts for the effect of cyclic plasticity.

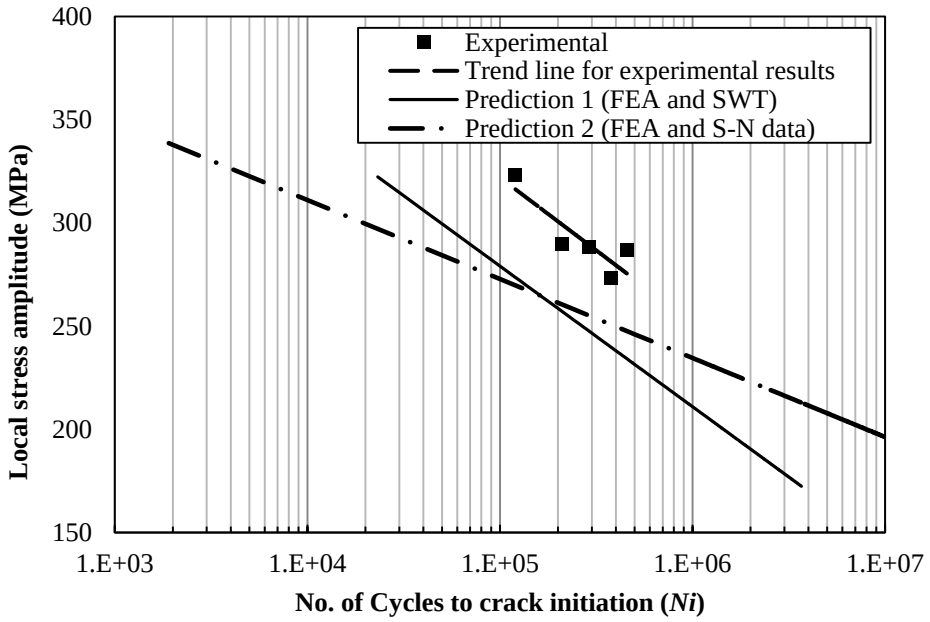


Figure 5.39. Comparison of predicted crack initiation lives with experimental tests in ambient air condition.

### 5.3.2 Sour environment

To predict the crack initiation life in the pre-pitted specimens tested in the sour corrosive environment, the local stress amplitudes at corrosion pits were calculated by method described in Chapter 4, by simultaneously solving the material's cyclic stress-strain relationship (Eq. 4.8) with the Glinka's rule (Eq. 4.10). Thereafter, the obtained

local stress amplitude and mean stress were used to predict fatigue crack initiation life ($N_i$) using the material's S-N data test measured in the sour environment as presented in Figure 5.7.

Figure 5.40 shows the relationship of the pit local stress amplitude (calculated by the aforementioned method) vs. the number of cycles to crack initiation. This figure compares the prediction with the experimental test results. It is apparent that the prediction is in a good agreement with experimental results (*i.e.* for a given life, the relative error in local stress amplitude is between 2-14%). The relative error of the trend line and the prediction is about 8%. One of the reasons for this error is that the S-N approach predicts the crack initiation life (because the pit local stress has a high gradient of the stress concentration) whereas the experimental results are the specimen's total life (i.e. number of cycles to failure).

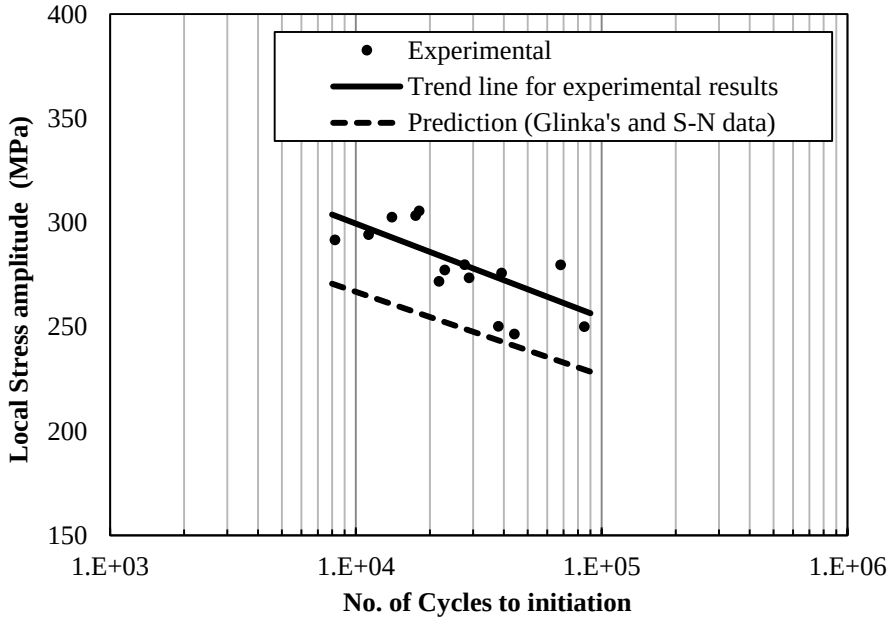


Figure 5.40. Comparison of predicted crack initiation lives with experimental tests in the sour environment.

# Chapter 6: Conclusions and future work

## 6.1 Summary

Oil and gas production pipelines often operate under sour corrosive environments that contain $H_2S$ gas in combination with the effects of cyclic loading. In this environment, steel is prone to a type of localised corrosion called corrosion pitting. The corrosion pits may lead to through-wall failure and loss of containment in pipelines, either directly through corrosion or indirectly following a pit-to-cracking transitional stage. Therefore a better understanding of this transitional stage in sour corrosive environment and a more reliable corrosion fatigue life model is required to reduce costs due to failures and their remediation and to increased operational safety. The aim of this study was to assess the effect of in-service sour corrosive environment on crack initiation at corrosion pits in API-5L X65 pipeline steel under cyclic loading.

In this project the investigation includes fatigue tests in ambient air and in sour environment on both smooth and pre-pitted specimens (sections 3 and 5.1), numerical and analytical models to study the fatigue behaviour of corrosion pits (sections 4.2 and 5.2) and a life prediction model for corrosion pit-to-fatigue crack transition (sections 4.1 and 5.3). Five groups of experimental fatigue test were carried out: 1) Smooth specimens in air, 2) Smooth specimen in sour corrosive environment, 3) Pre-pitted specimens in air, 4) Pre-pitted specimens in sour corrosive environment, and 5) Interrupted tests on pre-pitted specimens in sour environment. The purpose of the first and the second series of tests were to obtain S-N curves of API-5L X65 grade steel risers and the aim of the third, fourth and fifth series were to investigate the fatigue crack initiation from corrosion pits.

## 6.2 Novel contributions

1. Elastic-plastic Finite Element modelling of corrosion pit under cyclic loading, and using the pit local stress and strains to predict the crack initiation life in conjunction with the material S-N data obtained.
2. Considering the need in replicating the in-service sour environment to obtain more representative data, an environmental apparatus was designed and manufactured to facilitate the environmental fatigue tests. The test cell comprises five main elements, viz. the vessel body, vessel lids, locking rings, followers and grippers. Chemical, mechanical and optical properties of materials were considered in the materials selection process for each element to ensure the requirements of mechanical strength, visual monitoring of the test solution and test specimen within the vessel (e.g. to visualise sulphide film growth on the specimen and to alert for any air ingress leading to precipitation of sulphur), resistance to chemical degradation in saline solutions containing dissolved $H_2S$ and finally to provide excellent X-ray transmission. A bespoke gripping system was considered to lock-off the test specimen under a static load in order to keep the crack open during X-ray scanning. This feature is especially important as it assists with monitoring a crack and reduces the risk of crack wedging or crack closure after removing specimen from the test machine.
3. The new corrosion fatigue test methodology allowed X-ray micro-CT to be performed in-situ. The cell design facilitates periodic X-ray micro-CT, without the need to remove the specimen from the environmental cell.

4. Fractography of specimens tested in sour corrosive environment has been carried out for identification of the crack initiation site.
5. A pitting corrosion fatigue model is proposed for predicting the life from corrosion pit to fatigue cracking in sour corrosive environment and in ambient air. The local stress and strain ranges at corrosion pits were calculated by simultaneously solving the material's cyclic stress-strain relationship with either the Neuber's or Glinka's rule. Thereafter, the obtained local stress amplitude and mean stress were used to predict fatigue crack initiation life ($N_i$) using SWT equation for ambient condition and the measured material's S-N data test for the sour environment.
6. As the design of new environmental cell allows the specimen to be scanned under load without removal from the cell, issues relating to crack closure or degradation in the air are avoided. The safe and reproducible performance of the apparatus and test methodology for the study of the corrosion pit-to-crack transition in X-65 steel in sour saline solutions has been demonstrated.
7. The S-N curve in sour environment was obtained using smooth specimens in the developed environmental vessel. The obtained S-N curve was used for life prediction model.

## 6.3 Conclusions

### 6.3.1 Finite element stress analysis under the cyclic loads

- The maximum local stress under the static load does not change considerably with different pit geometries after material yielding, owing to the low strain hardening of this material; therefore the study of critical pit form under static

load can be based on the local strain and the location of strain localisation, from which fatigue crack may initiate.

- At high values of applied stress (e.g. 80%YS), the maximum strain localisation occurs near the pit mouth if the pit depth is small. When the pit depth is increased, the maximum strain localisation occurs near the pit bottom.
- Considerable plastic deformation occurs around the pit when the applied stress is 80%YS, which changes with the pit aspect ratio.
- The ratio of plastic zone volume to pit volume can influence the critical pit size and crack initiation location.
- Cyclic stress-strain hysteresis loops at the pit were determined by the finite element method. The analysis has revealed that by increasing the applied stress value and maintaining the applied stress ratio (e.g. at 0.1), the pit local stress ratio decreases and it can decrease further to a negative value if the applied stress and/or pit aspect ratio increase.
- Owing to the cyclic plasticity effect, local stress ratio at corrosion pit is considerably different from the applied stress ratio, depending on the pit geometry and applied stress level; cyclic plasticity will decrease the local stress ratio resulting in increased cyclic strain range and reduction in fatigue life.
- For all levels of applied stress studied in this work, pit geometry has a significant effect on the pit local stress. However, as the pit aspect ratio increases the increase rate in the local maximum stress decreases (owing to low strain hardening).

- Since the difference between the applied stress ratio and pit local stress ratio is found to be associated with the amount of cyclic plastic deformation around the pit base, this study implies the temporal evolution of cathodic or anodic regions in the corrosion pits based on the local stress ratio, which further suggests that mechano-electrochemical effects can be important at corrosion pits.
- The Glinka and Neuber's approaches delivered similar local stress and strain values as the FEA at the pits. Therefore, they can be good alternatives to the computationally expensive FEA.

### 6.3.2 Fatigue tests

- The X65 steel S-N curve was estimated based on the cyclic mechanical properties of this material and was validated by experiments. The results of experiments were close to the estimated S-N curve in both tested stress ratios (for a given life, the relative error in stress amplitude is less than 11%), therefore the estimated S-N curve can be a representative of tested X65 steel.
- Good control over the size of corrosion pits on X65 steel specimens grown by electrochemical methods has been achieved. Corrosion pits with aspect ratio (depth-to-mouth width) of 0.1 to 0.53 can be created with good repeatability. The results showed that potentiostatic method (specimen potential held constant) can give a better control over the pit size than the galvanostatic method (corrosion current held constant) in this material.

- Crack initiation sites that were near the pit mouth, walls and bottom were observed via Scanning Electron Microscopy of fractured specimens tested in ambient air.
- Comparison of the sour environment and ambient air S-N data shows fatigue strength reduction at all stress levels investigated in this work, with greater reduction at lower stress amplitudes. This finding supports the work of other studies in this area where the corrosive environment reduces the fatigue life more at lower stress amplitudes in comparison with higher stress amplitude.
- A relationship between pit geometry i.e. pit aspect ratio, applied stress and the number of cycles to failure were achieved from corrosion fatigue tests on pre-pitted specimens. It is seen that higher aspect ratio and higher applied stress led to more rapid onset of cracking and hence shorter crack initiation time.
- Fractography of fractured surfaces showed multiple crack initiation sites from pit that could be from the mouth, wall and base.

### 6.3.3. Prediction methods and validation by tests

- Two prediction approaches were proposed and tested in the ambient air condition first, *i.e.* the combination of elastic-plastic FE stress/strain analysis with material's S -N data or the strain-life data expressed by the Smith-Watson-Topper (SWT) equation.
- For the lower pit aspect ratio of 0.54 the two methods give similar predicted life; increasing the aspect ratio (meaning higher local stress and strain) widens the difference between the two predictive approaches.
- The predicted lives by both prediction methods were in good agreement with the tests in ambient air. (a) for lower pit aspect ratio (e.g. 0.54) fatigue life is

higher than $1.5\times10^5$ cycles where the two prediction approach coincident, the local stress amplitudes of experimental results are closer to prediction 2 (*i.e.* combination of FEA and S-N data). (b) for higher pit aspect ratio (meaning higher local stress and strains, and hence shorter life, tests are closer to prediction 1 (*i.e.* combination of FEA and SWT). This is because that at shorter lives the cyclic plasticity is much greater and the SWT approach accounts for the effect of cyclic plasticity.

- In the sour environment, fatigue life to crack initiation from corrosion pits was predicted by using the pit local stress in conjunction with the material's S-N relationship. The local stress amplitude at corrosion pits were calculated by simultaneously solving the material's cyclic stress-strain relationship with the Glinka's rule. Finally the obtained local stress amplitude was used to predict life using the sour environment S-N data.
- The predicted fatigue lives to crack initiation from the corrosion pits were in a good agreement with the experimental results in sour environment.

## 6.4 Outlook for future work

Further investigations could be carried out to assess the effect of double pit on pit-to-crack transition in corrosive environment. This can be done by making double pit on the specimen with different pit sizes and distances.

The developed environmental vessel can be used for corrosion fatigue tests in various kinds of materials used in several industries. The real in-service environment can be simulated in the vessel using the assigned inputs and outputs. Also a thermocouple can be added to the vessel to simulate high in-service temperatures. Visualisation in 3D of

fatigue damage development at the microscale (3.75 μm) is expected to advance subject knowledge in various industries.

In-situ corrosion fatigue tests inside the X-ray tomography machine can be useful to facilitate more X-ray scans without the need to remove the vessel. This can be carried out by designing a stationary loading system at the top and bottom of the vessel in a way that vessel can rotate 360 inside the load bearing system.

The outlined test protocol in this study has the potential to provide a more thorough understanding of the pit-to-fatigue crack transition mechanism than has previously been the case. For example the detailed evolution of fatigue crack can be monitored by interrupting the test more frequently (e.g. every 1000 cycles) upon detection of the initial crack.

Due to the high resolution of synchrotron X-ray tomography, a synchrotron X-ray micro-tomography can provide more insight into the effect of microstructure on pit-to-crack transition. This effect can also be studied by FEA of the 3D microstructure of the material around the pit obtained from synchrotron X-ray.

Corrosion fatigue tests on the specimens including weld in the centre can provide results about the effect of sour corrosive environment on fatigue behaviour of welds.

Image based FEA could be undertaken to assess the effect of real pit shape. In order to do this, X-ray images can be used to produce a finite element mesh. Then, the image based mesh is imported to finite element solver. In this way, the real 3D shape of defects is investigated under external loadings.

From the FEA results in static load applied, it can be hypothesized that the value of plastic zone volume over pit volume may determine the critical pit condition from which crack may initiate. This finding is potentially significant in terms of cracking via hydrogen embrittlement phenomena, for which there are many different routes to ingress of atomic hydrogen in metals and alloys (e.g. sour corrosion as in the present study, or corrosion in presence of other hydrogen recombination poisons such as cyanide, or cathodic overprotection, galvanic coupling of dissimilar metals, etc) which lead to similar levels of hydrogen charging and thus for a given material/microstructure, it may be possible to develop a general risk ranking for pit size-geometry leading to cracking in many different applications across industry. While this concept may only be useful in the case of reducing environments (e.g. deaerated) other simple relationships may exist for pits in oxidising conditions, which should be investigated in future work. The relationship between normalized plastic zone volume and critical pit condition can be verified by empirical studies. Experimental observation may thus support the hypothesis that the critical pit size from which cracks initiate may happen at a specific critical value of plastic zone volume over pit volume. In this project the focus of experimental study has been cyclic loading therefore, no experiments have been carried out under static load to verify the mentioned hypothesis.

## References


Ahmmad, M.M. and Sumi, Y. (2010) “Strength and Deformability of Corroded Steel Plates under Quasi-Static Tensile Load”. *Journal of marine science and technology* 15 (1), 1–15

Ahn, S.-H., Lawrence, F.V., and Metzger, M.M. (1992) “Corrosion Fatigue of an HSLA Steel”. *Fatigue & Fracture of Engineering Materials & Structures* 15 (7), 625–642

Akid, R. (1996) “The Influence of Environment upon the Accumulation of Damage under Corrosion Fatigue Conditions”. *Fatigue \& Fracture of Engineering Materials \& Structures* 19 (2-3), 277–285

Akid, R. (2010) *Corrosion Fatigue*.

Akid, R. and Dmytrakh, I. (1998) “Influence of Surface Deformation and Electrochemical Variables on Corrosion and Corrosion Fatigue Crack Development”. *Fatigue \& fracture of engineering materials \& structures* 21 (7), 903–911

Akid, R., Dmytrakh, I., and Gonzalez-Sanchez, J. (2006) “Fatigue Damage Accumulation: The Role of Corrosion on the Early Stages of Crack Development”. *Corrosion Engineering, Science and Technology* 41 (4), 328–335

Amaro, R.L., Rustagi, N., Findley, K.O., Drexler, E.S., and Slifka, A.J. (2014) “Modeling the Fatigue Crack Growth of X100 Pipeline Steel in Gaseous Hydrogen”. *International Journal of Fatigue* 59, 262–271

Arriscorreta, C.A. (2012) *Statistical Modeling for the Corrosion Fatigue of Aluminum Alloys 7075-T6 and 2024-T3*.

Bai, Y. and Bai, Q. (2005) *Subsea Pipelines and Risers*. Elsevier

Baragetti, S. (2014) “Notch Corrosion Fatigue Behavior of Ti-6Al-4V”. *Materials* 7 (6), 4349–4366

Bhandari, J., Khan, F., Abbassi, R., Garaniya, V., and Ojeda, R. (2015) “Modelling of Pitting Corrosion in Marine and Offshore Steel Structures-A Technical Review”. *Journal of Loss Prevention in the Process Industries* 37, 39–62

Boukerrou, A. and Cottis, R. (1993) “Crack Initiation in the Corrosion Fatigue of Structural Steels in Salt Solutions”. *Corrosion science* 35 (1-4), 577–585

Buffiere, J.-Y. (2017) “Fatigue Crack Initiation And Propagation From Defects In Metals: Is 3D Characterization Important?” *Procedia Structural Integrity* 7, 27–32

Burns, J., Larsen, J., and Gangloff, R. (2011) “Driving Forces for Localized Corrosion-to-Fatigue Crack Transition in Al-Zn-Mg-Cu”. *Fatigue \& Fracture of Engineering Materials \& Structures* 34 (10), 745–773

Buxton, D., Cottis, R., Scarf, P., and McIntyre, P. (1992) “Life Prediction in Corrosion Fatigue”. in *Proc. Int. Conf. Corrosion-Deformation Interaction, Fontainebleau, France*. held 1992. 901

Caines, S., Khan, F., and Shirokoff, J. (2013) “Analysis of Pitting Corrosion on Steel under Insulation in Marine Environments”. *Journal of Loss Prevention in the process Industries* 26 (6), 1466–1483

Cerit, M. (2013) “Numerical Investigation on Torsional Stress Concentration Factor at the Semi Elliptical Corrosion Pit”. *Corrosion Science* 67, 225–232

Cerit, M., Genel, K., and Eksi, S. (2009) “Numerical Investigation on Stress Concentration of Corrosion Pit”. *Engineering Failure Analysis* 16 (7), 2467–2472

Chapman, T., Kareh, K., Knop, M., Connolley, T., Lee, P., Azeem, M., Rugg, D., Lindley, T., and Dye, D. (2015) “Characterisation of Short Fatigue Cracks in Titanium Alloy IMI 834 Using X-Ray Microtomography”. *Acta Materialia* 99, 49–62

Chen, G., Wan, K.-C., Gao, M., Wei, R., and Flournoy, T. (1996) “Transition from Pitting to Fatigue Crack Growth—modeling of Corrosion Fatigue Crack Nucleation in a 2024-T3 Aluminum Alloy”. *Materials Science and Engineering: A* 219 (1), 126–132

Chlistovsky, R., Heffernan, P., and DuQuesnay, D. (2007) “Corrosion-Fatigue Behaviour of 7075-T651 Aluminum Alloy Subjected to Periodic Overloads”. *International Journal of Fatigue* 29 (9-11), 1941–1949

Cordes, N.L., Henderson, K., Stannard, T., Williams, J.J., Xiao, X., Robinson, M.W., Schaedler, T.A., Chawla, N., and Patterson, B.M. (2015) “Synchrotron-Based X-Ray Computed Tomography during Compression Loading of Cellular Materials”. *Microscopy Today* 23 (3), 12–19

Cornet, I. and GOLAN, S. (1959) “Influence of Temperature on Corrosion Fatigue”. *Corrosion* 15 (5), 58–64

Dolley, E., Lee, B., and Wei, R. (2000) “The Effect of Pitting Corrosion on Fatigue Life”. *Fatigue \& Fracture of Engineering Materials \& Structures* 23 (7), 555–560

Eadie, R., Szklarz, K., and Sutherby, R. (2005) “Corrosion Fatigue and near-Neutral pH Stress Corrosion Cracking of Pipeline Steel and the Effect of Hydrogen Sulfide”. *Corrosion* 61 (2), 167–173

Ebara, R. (2007) “Corrosion Fatigue Crack Initiation in 12\% Chromium Stainless Steel”. *Materials Science and Engineering: A* 468, 109–113

Fatoba, O. and Akid, R. (2014) “Low Cycle Fatigue Behaviour of API 5L X65 Pipeline Steel at Room Temperature”. *Procedia Engineering* 74, 279–286

Figueiredo, A.M.G., de Oliveira Ribeiro, G., Dias, J.F., Modenesi, P.J., Queiroz, F.L.P., de Oliveira Vasconcelos, J., and da Silveira Monteiro, H.A. (2015) “An Investigation of Bending Fatigue Crack Propagation in Structural Steel by the Measurement of Indirect Parameters”. *Journal of the Brazilian Society of Mechanical Sciences and Engineering* 37 (1), 305–312

Fink, C.G., Turner, W.D., and Paul, G.T. (1943) “Zinc Yellow in the Inhibition of Corrosion Fatigue of Steel in Sodium Chloride Solution”. *Transactions of The Electrochemical Society* 83 (1), 377–401

Gamboa, E., Linton, V., and Law, M. (2008) “Fatigue of Stress Corrosion Cracks in X65 Pipeline Steels”. *International Journal of Fatigue* 30 (5), 850–860

Glinka, G. (1985) “Calculation of Inelastic Notch-Tip Strain-Stress Histories under Cyclic Loading”. *Engineering Fracture Mechanics* 22 (5), 839–854

Goswami, T. and Hoeppner, D. (1997) “Review of Pit Nucleation, Growth and Pitting Corrosion Fatigue Mechanisms”. *Journal of the Mechanical Behavior of Materials* 8 (2), 169–196

Goswami, T. and Hoeppner, D.W. (1999) “Transition Criteria-From a Pit to a Crack”. *Journal of the Mechanical Behavior of Materials* 10 (5-6), 261–278

Goto, M. and Nisitani, H. (1992) “CRACK INITIATION AND PROPAGATION BEHAVIOUR OF A HEAT-TREATED CARBON STEEL IN CORROSION FATIGUE”. *Fatigue \& Fracture of Engineering Materials \& Structures* 15 (4), 353–363

Guan, L., Zhang, B., Yong, X., Wang, J., Han, E.-H., and Ke, W. (2015) “Effects of Cyclic Stress on the Metastable Pitting Characteristic for 304 Stainless Steel under Potentiostatic Polarization”. *Corrosion Science* 93, 80–89

Gutman, E., Solovioff, G., and Eliezer, D. (1996) “The Mechanochemical Behavior of Type 316L Stainless Steel”. *Corrosion science* 38 (7), 1141–1145

Gutman, E.M. (1994) *Mechanochemistry of Solid Surfaces*. World Scientific Publishing Co Inc

Hashemi, S. (2011) “Strength-Hardness Statistical Correlation in API X65 Steel”. *Materials Science and Engineering: A* 528 (3), 1648–1655

Hertzberg, R.W., Vinci, R., and Jason, L.H. (2012) *Deformation and Fracture Mechanics of Engineering Materials.*

Horner, D., Connolly, B., Zhou, S., Crocker, L., and Turnbull, A. (2011) "Novel Images of the Evolution of Stress Corrosion Cracks from Corrosion Pits". *Corrosion Science* 53 (11), 3466–3485

Htoo, A.T., Miyashita, Y., Otsuka, Y., Mutoh, Y., and Sakurai, S. (2016) "Variation of Local Stress Ratio and Its Effect on Notch Fatigue Behavior of 2024-T4 Aluminum Alloy". *International Journal of Fatigue* 88, 19–28

Hu, J., Tian, Y., Teng, H., Yu, L., and Zheng, M. (2014) "The Probabilistic Life Time Prediction Model of Oil Pipeline due to Local Corrosion Crack". *Theoretical and applied fracture mechanics* 70, 10–18

Ignatiev, K., Davis, G., Elliott, J., and Stock, S. (2006) "MicroCT (microtomography) Quantification of Microstructure Related to Macroscopic Behaviour: Part 1-Fatigue Crack Closure Measured in Situ in AA 2090 Compact Tension Samples". *Materials science and technology* 22 (9), 1025–1037

Ishihara, S., Saka, S., Nan, Z., Goshima, T., and Sunada, S. (2006) "Prediction of Corrosion Fatigue Lives of Aluminium Alloy on the Basis of Corrosion Pit Growth Law". *Fatigue \& Fracture of Engineering Materials \& Structures* 29 (6), 472–480

Jakubowski, M. (2015) "Influence of Pitting Corrosion on Fatigue and Corrosion Fatigue of Ship and Offshore Structures, Part II: Load-Pit-Crack Interaction". *Polish Maritime Research* 22 (3), 57–66

Ji, J., Zhang, C., Kodikara, J., and Yang, S.-Q. (2015) "Prediction of Stress Concentration Factor of Corrosion Pits on Buried Pipes by Least Squares Support Vector Machine". *Engineering Failure Analysis* 55, 131–138

Jones, K. and Hoeppner, D.W. (2006) "Prior Corrosion and Fatigue of 2024-T3 Aluminum Alloy". *Corrosion Science* 48 (10), 3109–3122

Jones, K. and Hoeppner, D.W. (2009) "The Interaction between Pitting Corrosion, Grain Boundaries, and Constituent Particles during Corrosion Fatigue of 7075-T6 Aluminum Alloy". *International journal of fatigue* 31 (4), 686–692

Karami, M. (2012) "Review of Corrosion Role in Gas Pipeline and Some Methods for Preventing It". *Journal of Pressure Vessel Technology* 134 (5), 054501

Kawai, S. and Kasai, K. (1985) "Considerations of Allowable Stress of Corrosion Fatigue (focused on the Influence of Pitting)". *Fatigue \& Fracture of Engineering Materials \& Structures* 8 (2), 115–127

Kermani, M., Harrop, D., and others (1996) “The Impact of Corrosion on Oil and Gas Industry”. *SPE Production \& Facilities* 11 (03), 186–190

Khan, Z. and Younas, M. (1996) “Corrosion-Fatigue Life Prediction for Notched Components Based on the Local Strain and Linear Elastic Fracture Mechanics Concepts”. *International journal of fatigue* 18 (7), 491–498

Khor, K., Buffiére, J.-Y., Ludwig, W., Toda, H., Ubhi, H., Gregson, P., and Sinclair, I. (2004) “In Situ High Resolution Synchrotron X-Ray Tomography of Fatigue Crack Closure Micromechanisms”. *Journal of Physics: Condensed Matter* 16 (33), S3511

Kolios, A., Srikanth, S., and Salonitis, K. (2014) “Numerical Simulation of Material Strength Deterioration due to Pitting Corrosion”. *Procedia CIRP* 13, 230–236

Kondo, Y. (1989) “Prediction of Fatigue Crack Initiation Life Based on Pit Growth”. *Corrosion* 45 (1), 7–11

Kumakura, Y., Takanashi, M., Fuji, A., Kitagawa, M., Kobayashi, Y., and others (1999) “Fatigue Strength of Coated Steel Plate in Seawater”. in *The Ninth International Offshore and Polar Engineering Conference*. held 1999

Larrosa, N.O., Chapetti, M.D., and Ainsworth, R.A. (2015) “Assessing Fatigue Endurance Limit of Pitted Specimens by Means of an Integrated Fracture Mechanics Approach”. in *ASME 2015 Pressure Vessels and Piping Conference*. held 2015. V007T07A005–V007T07A005

Li, S.-X. and Akid, R. (2013) “Corrosion Fatigue Life Prediction of a Steel Shaft Material in Seawater”. *Engineering Failure Analysis* 34, 324–334

Li, X., Zhang, J., Akiyama, E., Wang, Y., and Li, Q. (2018) “Microstructural and Crystallographic Study of Hydrogen-Assisted Cracking in High Strength PSB1080 Steel”. *International Journal of Hydrogen Energy*

Linder, J. and Blom, R. (2001) “Development of a Method for Corrosion Fatigue Life Prediction of Structurally Loaded Bearing Steels”. *Corrosion* 57 (5), 404–412

Lindley, T., McIntyre, P., and Trant, P. (1982) “Fatigue-Crack Initiation at Corrosion Pits”. *Metals technology* 9 (1), 135–142

Lu, B. and Luo, J. (2006) “Crack Initiation and Early Propagation of X70 Steel in Simulated near-Neutral pH Groundwater”. *Corrosion* 62 (8), 723–731

Lu, B., Luo, J., Norton, P., and Ma, H. (2009) “Effects of Dissolved Hydrogen and Elastic and Plastic Deformation on Active Dissolution of Pipeline Steel in Anaerobic Groundwater of near-Neutral pH”. *Acta Materialia* 57 (1), 41–49

Lu, B., Yu, H., and Luo, J. (2013) “Effects of Plastic Deformation and Carbon Dioxide on Corrosion of Pipeline Steel in near-Neutral pH Groundwater”. *Journal*

*of materials engineering and performance* 22 (5), 1430–1435

Lu, X., Rawson, S.D., and Withers, P.J. (2018) "Effect of Hydration and Crack Orientation on Crack-Tip Strain, Crack Opening Displacement and Crack-Tip Shielding in Elephant Dentin". *Dental Materials*

Ludwig, W., Buffière, J.-Y., Savelli, S., and Cloetens, P. (2003) "Study of the Interaction of a Short Fatigue Crack with Grain Boundaries in a Cast Al Alloy Using X-Ray Microtomography". *Acta Materialia* 51 (3), 585–598

Lynch, S. (2016) "Understanding Mechanisms and Kinetics of Environmentally Assisted Cracking". *BHM Berg-und Hüttenmännische Monatshefte* 161 (1), 3–18

Maire, E., Le Bourlot, C., Adrien, J., Mortensen, A., and Mokso, R. (2016) "20 Hz X-Ray Tomography during an in Situ Tensile Test". *International journal of fracture* 200 (1-2), 3–12

Maire, E., Carmona, V., Courbon, J., and Ludwig, W. (2007) "Fast X-Ray Tomography and Acoustic Emission Study of Damage in Metals during Continuous Tensile Tests". *Acta Materialia* 55 (20), 6806–6815

Marrow, T., Buffiere, J.-Y., Withers, P., Johnson, G., and Engelberg, D. (2004) "High Resolution X-Ray Tomography of Short Fatigue Crack Nucleation in Austempered Ductile Cast Iron". *International journal of fatigue* 26 (7), 717–725

McEvily Jr, A. (1990) *Atlas of Stress-Corrosion and Corrosion Fatigue Curves*.

Medved, J., Breton, M., and Irving, P. (2004) "Corrosion Pit Size Distributions and Fatigue Lives—a Study of the EIFS Technique for Fatigue Design in the Presence of Corrosion". *International journal of fatigue* 26 (1), 71–80

Miller, K. and Akid, R. (1996) "The Application of Microstructural Fracture Mechanics to Various Metal Surface States". *Proc. R. Soc. Lond. A* 452 (1949), 1411–1432

Mohammed, S., Hua, Y., Barker, R., and Neville, A. (2017) "Investigating Pitting in X65 Carbon Steel Using Potentiostatic Polarisation". *Applied Surface Science* 423, 25–32

Mu, Z.T., Chen, D.H., Zhu, Z.T., and Ye, B. (2011) "The Stress Concentration Factor of Different Corrosion Pits Shape". in *Advanced Materials Research*. held 2011. 1115–1119

Murtaza, G. and Akid, R. (1996) "Corrosion Fatigue Short Crack Growth Behaviour in a High Strength Steel". *International journal of fatigue* 18 (8), 557–566

Murtaza, G. and Akid, R. (2000) "Empirical Corrosion Fatigue Life Prediction Models of a High Strength Steel". *Engineering Fracture Mechanics* 67 (5), 461–

Mustansar, Z., McDonald, S.A., Sellers, W.I., Manning, P.L., Lowe, T., Withers, P.J., and Margetts, L. (2017) "A Study of the Progression of Damage in an Axially Loaded Branta Leucopsis Femur Using X-Ray Computed Tomography and Digital Image Correlation". *PeerJ* 5, e3416

Nadimi, S., Kong, D., and Fonseca, J. (2017) *From Imaging to Prediction of Carbonate Sand Behaviour*.

Neuber, H. (1961) "Theory of Stress Concentration for Shear-Strained Prismatical Bodies with Arbitrary Nonlinear Stress-Strain Law". *Journal of Applied Mechanics* 28 (4), 544–550

Ohaeri, E., Szpunar, J., Fazeli, F., and Arafin, M. (2018) "Hydrogen Induced Cracking Susceptibility of API 5L X70 Pipeline Steel in Relation to Microstructure and Crystallographic Texture Developed after Different Thermomechanical Treatments". *Materials Characterization*

Ok, D., Pu, Y., and Incecik, A. (2007) "Computation of Ultimate Strength of Locally Corroded Unstiffened Plates under Uniaxial Compression". *Marine Structures* 20 (1), 100–114

Ossai, C.I., Boswell, B., and Davies, I.J. (2015) "Pipeline Failures in Corrosive Environments-A Conceptual Analysis of Trends and Effects". *Engineering Failure Analysis* 53, 36–58

Paik, J.K., Lee, J.M., and Ko, M.J. (2004) "Ultimate Shear Strength of Plate Elements with Pit Corrosion Wastage". *Thin-Walled Structures* 42 (8), 1161–1176

Pan, T. (2012) "Corrosion Behavior of a Duplex Stainless Steel under Cyclic Loading: A Scanning Kelvin Probe Force Microscopy (SKPFM) Based Microscopic Study". *Journal of Applied Electrochemistry* 42 (12), 1049–1056

Papavinasam, S. (2013) *Corrosion Control in the Oil and Gas Industry*. Elsevier

Parkins, R. (1964) "Stress-Corrosion Cracking". *Metallurgical Reviews* 9 (1), 201–260

Patterson, B.M., Cordes, N.L., Henderson, K., Williams, J.J., Stannard, T., Singh, S.S., Ovejero, A.R., Xiao, X., Robinson, M., and Chawla, N. (2016) "In Situ X-Ray Synchrotron Tomographic Imaging during the Compression of Hyper-Elastic Polymeric Materials". *Journal of materials science* 51 (1), 171–187

Pidaparti, R.M. and Patel, R.K. (2010) "Investigation of a Single Pit/defect Evolution during the Corrosion Process". *Corrosion Science* 52 (9), 3150–3153

Pidaparti, R.M. and Patel, R.R. (2008) “Correlation between Corrosion Pits and Stresses in Al Alloys”. *Materials Letters* 62 (30), 4497–4499

Pidaparti, R.M. and Rao, A.S. (2008) “Analysis of Pits Induced Stresses due to Metal Corrosion”. *Corrosion Science* 50 (7), 1932–1938

Poberezhnyi, L., Maruschak, P., Prentkovskis, O., Danyliuk, I., Pyrig, T., and Brezinová, J. (2016) “Fatigue and Failure of Steel of Offshore Gas Pipeline after the Laying Operation”. *Archives of Civil and Mechanical Engineering* 16 (3), 524–536

Proudhon, H., Moffat, A., Sinclair, I., and Buffiere, J.-Y. (2012) “Three-Dimensional Characterisation and Modelling of Small Fatigue Corner Cracks in High Strength Al-Alloys”. *Comptes Rendus Physique* 13 (3), 316–327

Qian, L., Toda, H., Uesugi, K., Ohgaki, T., Kobayashi, M., and Kobayashi, T. (2008) “Three-Dimensional Visualization of Ductile Fracture in an Al-Si Alloy by High-Resolution Synchrotron X-Ray Microtomography”. *Materials Science and Engineering: A* 483, 293–296

Qu, P., Toda, H., Zhang, H., Sakaguchi, Y., Qian, L., Kobayashi, M., and Uesugi, K. (2009) “Local Crack Driving Force Analysis of a Fatigue Crack by a Microstructural Tracking Method”. *Scripta Materialia* 61 (5), 489–492

Rajabipour, A. and Melchers, R.E. (2013) “A Numerical Study of Damage Caused by Combined Pitting Corrosion and Axial Stress in Steel Pipes”. *Corrosion Science* 76, 292–301

Ranganathan, N., Aldroe, H., Lacroix, F., Chalon, F., Leroy, R., and Tougui, A. (2011) “Fatigue Crack Initiation at a Notch”. *International Journal of Fatigue* 33 (3), 492–499

Rokhlin, S., Kim, J.-Y., Nagy, H., and Zoofan, B. (1999) “Effect of Pitting Corrosion on Fatigue Crack Initiation and Fatigue Life”. *Engineering Fracture Mechanics* 62 (4), 425–444

Sachs, N.W. (2005) “Understanding the Surface Features of Fatigue Fractures: How They Describe the Failure Cause and the Failure History”. *Journal of Failure Analysis and Prevention* 5 (2), 11–15

Sankaran, K., Perez, R., and Jata, K. (2001) “Effects of Pitting Corrosion on the Fatigue Behavior of Aluminum Alloy 7075-T6: Modeling and Experimental Studies”. *Materials Science and Engineering: A* 297 (1), 223–229

Sato, N. (1971) “A Theory for Breakdown of Anodic Oxide Films on Metals”. *Electrochimica Acta* 16 (10), 1683–1692

Schoenbauer, B.M., Perlega, A., Karr, U.P., Gandy, D., and Stanzl-Tschegg, S.E. (2015) “Pit-to-Crack Transition under Cyclic Loading in 12\% Cr Steam Turbine Blade Steel”. *International Journal of Fatigue* 76, 19–32

Scully, J. and Moran, P. (1988) “Influence of Strain on the Environmental Hydrogen-Assisted Cracking of a High-Strength Steel in Sodium Chloride Solution”. *Corrosion* 44 (3), 176–185

Singh, S.S., Williams, J.J., Hruby, P., Xiao, X., De Carlo, F., and Chawla, N. (2014) “In Situ Experimental Techniques to Study the Mechanical Behavior of Materials Using X-Ray Synchrotron Tomography”. *Integrating Materials and Manufacturing Innovation* 3 (1), 9

Singh, S.S., Williams, J.J., Stannard, T.J., Xiao, X., De Carlo, F., and Chawla, N. (2016) “Measurement of Localized Corrosion Rates at Inclusion Particles in AA7075 by in Situ Three Dimensional (3D) X-Ray Synchrotron Tomography”. *Corrosion Science* 104, 330–335

Smith, K.N., Topper, T.H., and Watson, P. (1970) “A Stress-Strain Function for the Fatigue of Metals”. *J mater* 5, 767–778

Sriraman, M. and Pidaparti, R. (2010) “Crack Initiation Life of Materials under Combined Pitting Corrosion and Cyclic Loading”. *Journal of materials engineering and performance* 19 (1), 7–12

Srivatsan, S. and Sudarshan, T. (1988) “Mechanisms of Fatigue Crack Initiation in Metals: Role of Aqueous Environments”. *Journal of materials science* 23 (5), 1521–1533

Stephens, R.I., Fatemi, A., Stephens, R.R., and Fuchs, H.O. (2000) *Metal Fatigue in Engineering*. John Wiley \& Sons

Sun, J., Sun, C., Zhang, G., Li, X., Zhao, W., Jiang, T., Liu, H., Cheng, X., and Wang, Y. (2016) “Effect of O2 and H2S Impurities on the Corrosion Behavior of X65 Steel in Water-Saturated Supercritical CO2 System”. *Corrosion Science* 107, 31–40

Suresh, S. (1998) *Fatigue of Materials*. Cambridge university press

Toda, H., Maire, E., Yamauchi, S., Tsuruta, H., Hiramatsu, T., and Kobayashi, M. (2011) “In Situ Observation of Ductile Fracture Using X-Ray Tomography Technique”. *Acta Materialia* 59 (5), 1995–2008

Turnbull, A. (1993) “Modelling of Environment Assisted Cracking”. *Corrosion science* 34 (6), 921–960

Turnbull, A. (2014) “Corrosion Pitting and Environmentally Assisted Small Crack Growth”. in *Proc. R. Soc. A.* held 2014. 20140254

Turnbull, A. and Crocker, L. (2006) *Finite Element Analysis of the Stress and Strain Associated with a Corrosion Pit in a Cylindrical Specimen under Applied Tensile Loading*. National Physical Laboratory

Turnbull, A., Horner, D., and Connolly, B. (2009) "Challenges in Modelling the Evolution of Stress Corrosion Cracks from Pits". *Engineering Fracture Mechanics* 76 (5), 633–640

Turnbull, A., McCartney, L., and Zhou, S. (2006) "Modelling of the Evolution of Stress Corrosion Cracks from Corrosion Pits". *Scripta materialia* 54 (4), 575–578

Turnbull, A., Wright, L., and Crocker, L. (2010) "New Insight into the Pit-to-Crack Transition from Finite Element Analysis of the Stress and Strain Distribution around a Corrosion Pit". *Corrosion Science* 52 (4), 1492–1498

Turnbull, A. and Zhou, S. (2004) "Pit to Crack Transition in Stress Corrosion Cracking of a Steam Turbine Disc Steel". *Corrosion science* 46 (5), 1239–1264

Vosikovsky, O. (1976) "Fatigue Crack Growth in an X65 Line-Pipe Steel in Sour Crude Oil". *Corrosion* 32 (12), 472–475

Van der Walde, K. and Hillberry, B. (2007) "Initiation and Shape Development of Corrosion-Nucleated Fatigue Cracking". *International Journal of Fatigue* 29 (7), 1269–1281

Van der Walde, K. and Hillberry, B. (2008) "Characterization of Pitting Damage and Prediction of Remaining Fatigue Life". *International Journal of Fatigue* 30 (1), 106–118

Wang, Y. and Akid, R. (1996) "Role of Nonmetallic Inclusions in Fatigue, Pitting, and Corrosion Fatigue". *Corrosion* 52 (2), 92–102

Wei, R. and Gao, M. (1983) "Reconsideration of the Superposition Model for Environmentally Assisted Fatigue Crack Growth". *Scripta metallurgica* 17 (7), 959–962

Williams, J.J., Yazzie, K.E., Phillips, N.C., Chawla, N., Xiao, X., De Carlo, F., Iyyer, N., and Kittur, M. (2011) "On the Correlation between Fatigue Striation Spacing and Crack Growth Rate: A Three-Dimensional (3-D) X-Ray Synchrotron Tomography Study". *Metallurgical and Materials Transactions A* 42 (13), 3845–3848

Wirsching, P.H. (1984) "Fatigue Reliability for Offshore Structures". *Journal of Structural Engineering* 110 (10), 2340–2356

Withers, P.J. and Preuss, M. (2012) "Fatigue and Damage in Structural Materials Studied by X-Ray Tomography". *annual review of materials research* 42, 81–103

Wu, S., Xiao, T., and Withers, P. (2017) “The Imaging of Failure in Structural Materials by Synchrotron Radiation X-Ray Microtomography”. *Engineering Fracture Mechanics* 182, 127–156

Wu, S., Yu, C., Yu, P., Buffière, J., Helfen, L., and Fu, Y. (2016) “Corner Fatigue Cracking Behavior of Hybrid Laser AA7020 Welds by Synchrotron X-Ray Computed Microtomography”. *Materials Science and Engineering: A* 651, 604–614

Xu, S. and Wang, Y. (2015) “Estimating the Effects of Corrosion Pits on the Fatigue Life of Steel Plate Based on the 3D Profile”. *International Journal of Fatigue* 72, 27–41

Yang, Y. and Akid, R. (2015) “Electrochemical Investigation of the Corrosion of Different Microstructural Phases of X65 Pipeline Steel under Saturated Carbon Dioxide Conditions”. *Materials* 8 (5), 2635–2649

Yu, M., Xing, X., Zhang, H., Zhao, J., Eadie, R., Chen, W., Been, J., Van Boven, G., and Kania, R. (2015) “Corrosion Fatigue Crack Growth Behavior of Pipeline Steel under Underload-Type Variable Amplitude Loading Schemes”. *Acta Materialia* 96, 159–169

Zeng, Z. and Fatemi, A. (2001) “Elasto-Plastic Stress and Strain Behaviour at Notch Roots under Monotonic and Cyclic Loadings”. *The Journal of Strain Analysis for Engineering Design* 36 (3), 287–300

Zhang, G. and Cheng, Y. (2011) “Localized Corrosion of Carbon Steel in a CO2-Saturated Oilfield Formation Water”. *Electrochimica Acta* 56 (3), 1676–1685

Zhang, H., Toda, H., Qu, P., Sakaguchi, Y., Kobayashi, M., Uesugi, K., and Suzuki, Y. (2009) “Three-Dimensional Fatigue Crack Growth Behavior in an Aluminum Alloy Investigated with in Situ High-Resolution Synchrotron X-Ray Microtomography”. *Acta Materialia* 57 (11), 3287–3300

Zhang, R. and Mahadevan, S. (2001) “Reliability-Based Reassessment of Corrosion Fatigue Life”. *Structural safety* 23 (1), 77–91

Zhang, X.-Y., Li, S.-X., and Liang, R. (2013) “Effect of Corrosion Pits on Fatigue Life and Crack Initiation”. in *ICF13*. held 2013

Zhang, Y., Du, M., Zhang, J., and Du, J. (2015) “Corrosion Behavior of X65 Carbon Steel in Simulated Oilfield Produced Water”. *Materials and Corrosion* 66 (4), 366–374

Zhang, Y., Fan, M., Xiao, Z., and Zhang, W. (2016) “Fatigue Analysis on Offshore Pipelines with Embedded Cracks”. *Ocean Engineering* 117, 45–56

Appendix A

| Fatigue test series | Test condition | Pre-pitted | Tested at stress amplitude level | Specimen schismatic |
|---|---|---|---|---|
| 1 | Ambient air | ☒ | 150 to 280MPa | 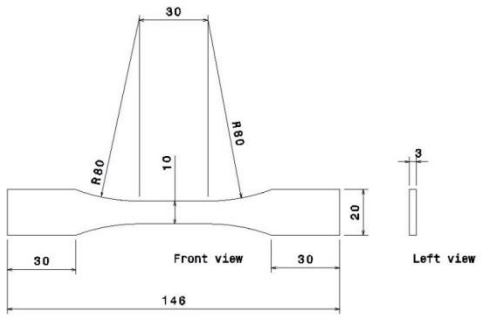  |
| 2 | Ambient air | ☑- pit sizes in table 3.3 | 225 to 230MPa | 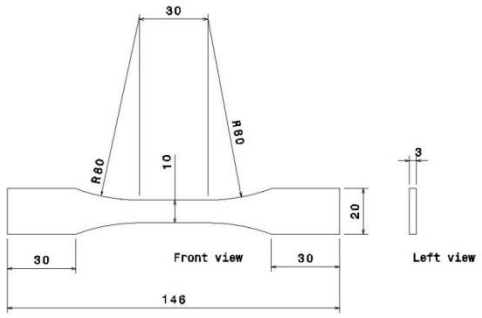  |
| 3 | Sour environment | ☒ | 135 to 209 MPa | 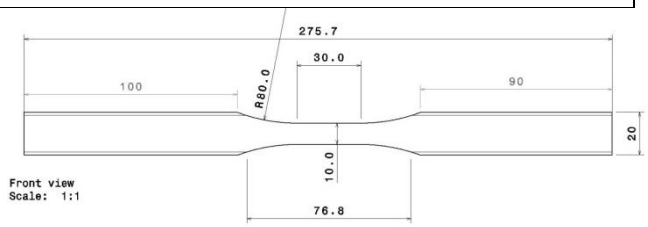  |
| 4 | Sour environment | ☑- pit sizes are shown in table 3.4 | 165 and 185 MPa | 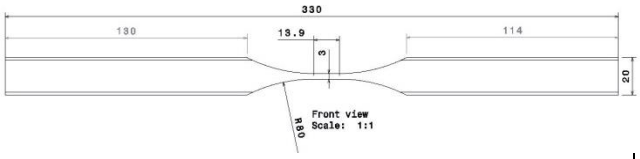  |
| 5 | Sour environment | ☑- pit sizes are shown in table 3.5 | 165 and 185 MPa | 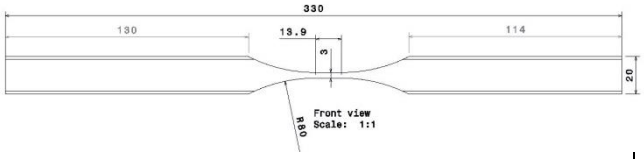  |